INVESTIGATION OF FLUID FLOW THROUGH TWO-DEPTH AND TWO WIDTH MICRO CHANNELS

THESIS SUBMITTED IN PARTIAL FULFILMENT OF THE
REQUIREMENTS FOR THE DEGREE
OF

MASTER OF ENGINEERING
IN
MECHANICAL ENGINEERING

BY
RISHI JAIN

UNDER THE GUIDANCE OF
PROF. M. A. MANNAN

DEPARTMENT OF MECHANICAL AND PRODUCTION ENGINEERING

NATIONAL UNIVERSITY OF SINGAPORE
SINGAPORE

Session 2001/2003

Abstract

The family of chips called micro total analysis systems (μ-TAS) and lab-on-chip (LOC) refers to microfluidics devices and their functional integration. The microfluidic aspect of μ-TAS and LOC deals with single phase or multi-phase fluid flow inside the micro channels of different geometries, shapes and architecture. A two-depth and two-width micro channel is introduced in which a micro-reservoir is placed between two micro channels namely the first channel, the depth of which is equal to the depth of micro reservoir and the shallow channel, the depth of which is approximately $1/120^{th}$ to $1/20^{th}$ of the depth of the micro reservoir. These kinds of micro channels are suitable for μ-TAS and LOC applications for they can be used for cell-cell separation, cell deformability tests, micro-filters, micro-reactors etc. Different architectures of these micro channels can be optimized for different applications. In this study, Computational Fluid Dynamics (CFD) two-phase flow simulations have been carried out to understand the performance of these micro channels in terms of pressure profiles and centerline velocity magnitude along the length of the channel, particle accumulation and path lines in the micro reservoir of the channel and the flow resistance of these micro channels. The effects of the position of the micro reservoir from the inlet, the depth of first channel, micro reservoir and shallow channel and the cross-section of the micro reservoir for different widths of first channel have been analyzed. Experimental studies have been carried out to examine the flow resistance of a two-depth two-width micro channel and a straight micro channel.

Acknowledgements

I express my sincere thanks to Prof. M.A. Mannan for his invaluable supervision and guidance. He was always available with new ideas and suggestions during difficult phases of the project. All his help is gratefully acknowledged.

I remain indebted to Prof. Simon Ang Saw-Teong, project co-supervisor for his invaluable helps in all phases of work.

I would like to express some gratitude to Mr. Lee, lab officer of work-shop 2, Ms Grace Foo, staff in the Supercomputing and Visualization Unit (SVU) of NUS Computer Center, Mr. Phang, supplier of equipment for experimental work and Mr. Kong, lab officer at Institute of Materials Research and Engineering (IMRE).

Table of Contents

List of Figures

List of Tables

List of Symbols

μm	micron
Re	Reynolds number
ΔP	pressure drop
Q	flow rate
ΔP^*	normalized pressure drop
Q^*	normalized flow rate
ρ	density (in kg/m^3)
x	horizontal coordinate (in mm)
y	vertical coordinate (in mm)
z	axial coordinate (in mm)
D	diameter
Δm	change in mass
Δt	change in time
FS	full scale
L	length

Chapter 1: Introduction

1.1 Motivation

The modern lab-on-chip found in a typical diagnosis laboratory consists of one or more micro channels stacked in different ways on a silicon substrate. The substrate is covered with a thin glass which serves as a medium to gather information from the channel. A small sensor head focuses on a section of the micro channel in order to investigate the happenings inside the micro channel. E.g. Kiichi Sato's immunosorbant assay system, which he used for the analysis of secretory human immunoglobulin A on polystyrene beads, works on the same principle [1]. The sensor gets the information from the micro reservoir in terms of signals which are emitted from the particles, which are mixed with the fluid flowing through the micro channel.

1.2 Outline

In this thesis, the CFD simulation of the two-phase flow through the two-depth and two-width micro channels and experimental validation of the flow resistance through one of them are presented. These micro channels can be used for μ-TAS and LOC applications such as micro-filters, micro-mixers or micro-reaction-chambers. A simple design for a two-depth and two-width micro channel (Figure 1.1) in a flow through device consists of three parts, namely, the first channel, the micro reservoir and the shallow channel. The geometrical placement of the micro reservoir and other dimensions of the micro channel are constrained by three demands. Firstly, the flow resistance of the filter must remain within certain limits. Secondly, the filter should not be sensitive to clogging. Finally, the

collected particles should be held within a relatively small confined area to facilitate detection.

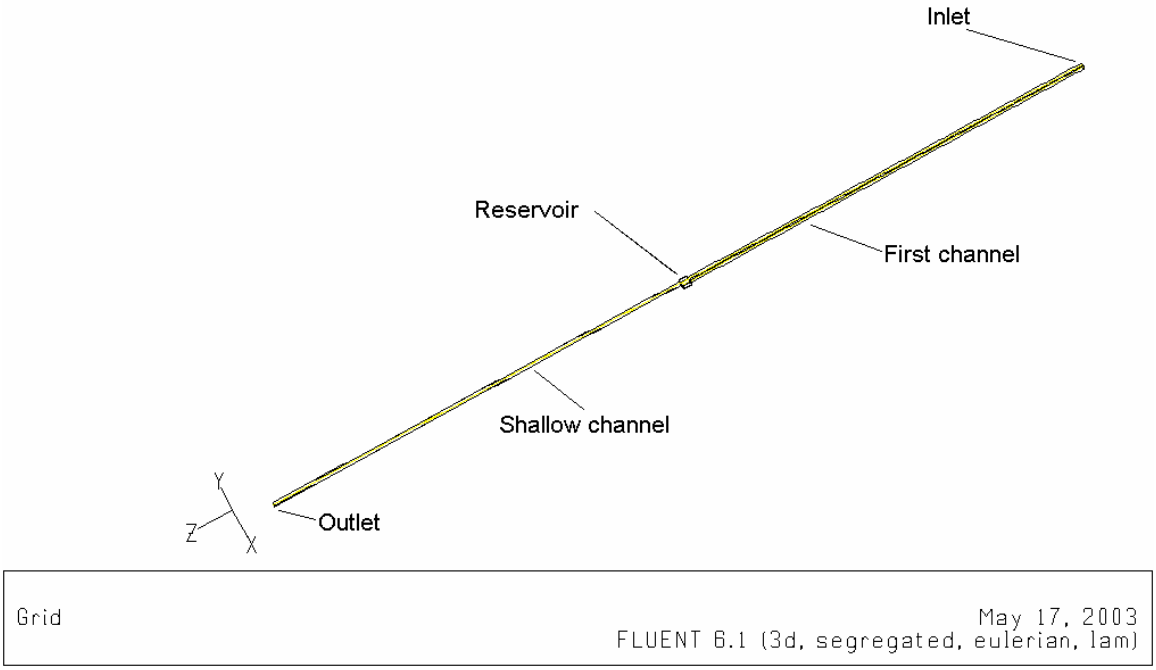

Figure 1.1: A two-depth and two-width micro channel

The visual analysis of various cases of these micro channel geometries is accomplished using FLUENT CFD Package which is based on the finite volume method to analyze flow in a specified domain. Modeling of these micro channel geometries is done using GAMBIT modeling software. Different cases were considered by:

1. Changing the position of the micro reservoir from the inlet
2. Changing the first channel depth and micro reservoir depth keeping the shallow channel depth = 5 micron and other parameters constant.
3. Changing the first channel depth and micro reservoir depth keeping the shallow channel depth = 3 micron and other parameters constant.

4. Changing the square cross-section of the micro reservoir for first channel width and shallow channel width = 100 micron and other parameters constant.
5. Changing the square cross-section of the micro reservoir for first channel width and shallow channel width = 150 micron and other parameters constant.
6. Changing the square cross-section of the micro reservoir for first channel width and shallow channel width = 70 micron and other parameters constant.

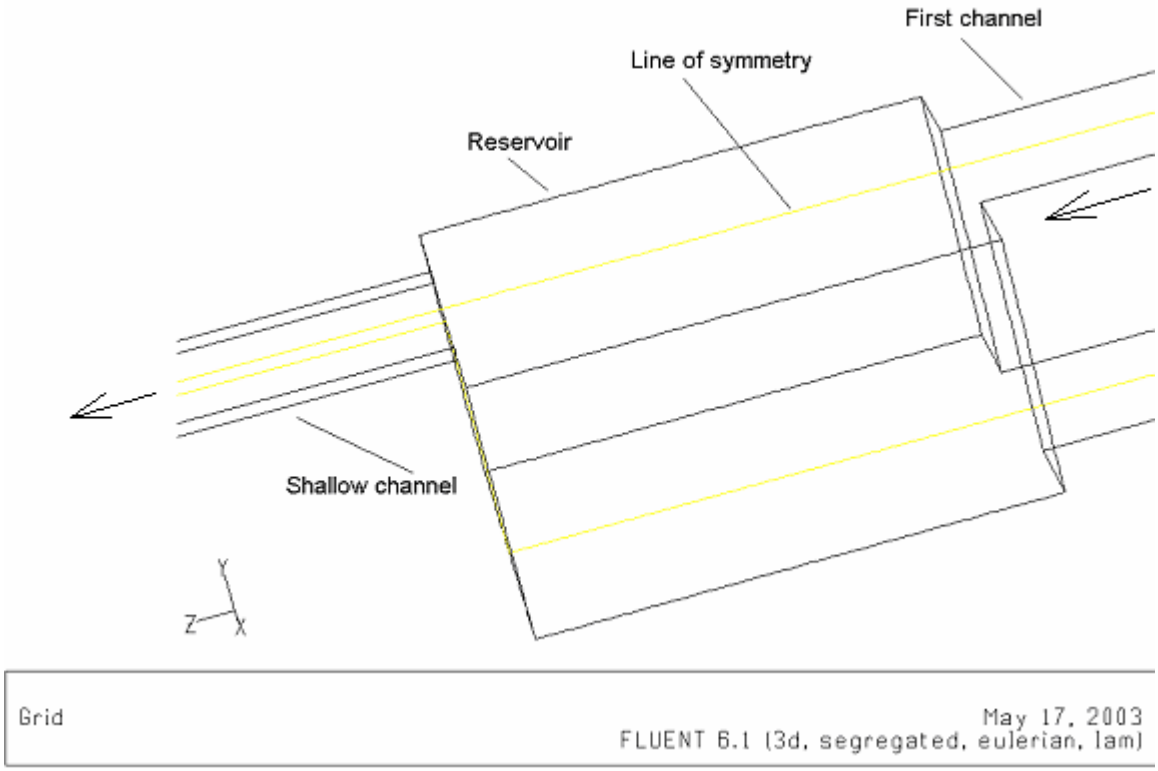

Figure 1.2: Perspective view of the micro channel micro reservoir

The CFD simulation results are categorized as follows:

a) Pressure profiles along the length of the micro channels

b) Velocity magnitude along the length of the micro channels

c) Volume fraction of phase-2 (micro particles) in the micro reservoir and

d) Path lines followed by particles injected from the inlet surface in the micro reservoir.

e) Mass fluxes delivered by the micro channels

The length of the micro channel (overall) is 20 mm. Flow through the micro channel is provided by the pressure difference of 200 kPa between the inlet and outlet face. The computations were done on the Computer Server name Cheetah4 (Model: Compaq GS320, Os: Tru645.1). The pre- and post processing front-end used is Pollux (Model: Sun Blade 1000, Os: Solaris 8).

The second part of the thesis deals with the fabrication and characterization of one of two-depth and two-width micro channels and one straight micro channel without micro reservoir and shallow channel. These micro channels were fabricated at the Institute of Microelectronics, Singapore. The anodic bonding on these micro channels was done at the Institute of Material Research and Engineering. The micro channel holder was designed and fabricated in Workshop-II. Other components for the experimental setup were supplied by Power and Motion Control Limited, Singapore.

1.3 Scope

The work presented in this thesis is summarized in seven chapters, in which a brief description of the motivation and objectives is given in the introductory Chapter 1. Chapter 2 deals with the literature review of some past research achievements on numerical and experimental studies on micro channels for μ-TAS and LOC applications. Experimental studies of flow through micro channels of different dimensions for different Reynolds numbers are also reviewed. In Chapter 3, the CFD Analysis considerations are described for two-phase flow simulation in two-depth and two-width micro channels.

Various modeling constraints and assumptions are covered in this chapter. The results and discussion of the CFD analysis are described in Chapter 4 in which the results are analyzed sequentially according to the objective of the thesis. Chapter 5 describes the experimental design and measurement work for two different types of micro channels, two-depth and two-width micro channel and straight micro channel. Results and Discussion on the experiments are described in Chapter 6. The thesis is concluded in Chapter 7.

Chapter 2: Literature Review

Several researchers have investigated flow in the micro channels with different micro channel shapes. The micro channels can be distinguished in many ways: the surface on which the micro channel is etched, the cross-sectional geometry of the micro channel, the geometry of the micro channel along its length, and of course, the depth, width and length of the micro channels. These different aspects are taken into consideration to get the output of certain experimental or simulation investigation which leads to a selected application in the micro fluidics sector. In addition, the work of the following mentioned people deals with different types of micro channel geometries which they found most suitable for fulfilling their own research objective. Normally, the micro channels used in μ-TAS and LOC applications are non-linear and non-circular micro channels.

2.1 Micro channel studies for μ-TAS and LOC applications

Anne Y. Fu et al. (1999) [2] used rectangular micro channels with tapering walls for the purpose of cell sorting. The tapering of the walls makes the micro channel width contract from 100 micron to 3 micron. The depth of the micro channel was 4 micron.

Kiichi Sato et al. (2000) [1] studied a micro channel with 100 micron depth and 200 micron width. The micro channel has a dam shape of length 2 mm in the middle which makes the depth above it 10 micron. They used this technique to stop the polystyrene beads flowing with the fluid in the micro channel for the analysis of secretory human immunoglobulin A.

Wilding et al. (1997) [3] used an array of silicon micro posts separated by tortuous channels spaced apart on silicon substrate. They considered different designs for filtering purposes as mentioned in Table 2.1

Table 2.1: Wilding's filter chip designs

S No.	Designs
1.	Offset array of simple micro posts (13 X 20 micron spaced 7 micron apart) set across a 500 micron wide x 20 micron deep silicon channels.
2.	Array of complex micro posts (73 micron wide) separated by 7 micron wide tortuous channels spaced 30 micron apart and set across a 500 micron wide X 5.7 micron deep silicon channel
3.	Array of 120 micro posts (175 micron X 18 micron wide) separated by 6 micron channels set across a 3 mm wide X 13 micron deep silicon channel.

Wesley Chang et al. (2000) [4] investigated the use of simple power law for blood flow of between 2.5 micro liter to 100 micro liter per minute in channel with 200 X 60 micron cross-sections and the configurations of straight, 90 degree bend and sudden contraction from 200 micron to 100 micron. They did experimental measurements of pressure vs. flow rate for blood flow in these channels to validate the predictions of hydrodynamic resistance generated by CFD simulations

Similar to the work herein, Anderson et al. (2000) [5] used three different widths along the length of the micro channel. The micro channel was divided into inlet channel, outlet channel and a reaction chamber in between. The reaction chamber had pillars to hold the polystyrene beads flowing with the fluid in it. Various designs considered by them are tabulated in table 2.2.

Table 2.2: A summary of the different designs of the flow-through micro machined device where V is the filter chamber volume, W the pillar width, L the pillar length, and H the pillar heights.

Design	Reaction chamber V(nl)	Pillar W, L, H (micron	Pillar spacing (micron)	Number of pillars	Inlet channel W, L, H (micron)	Outlet channel W, L, H (micron)
1.	0.5	3, 10, 50	2	70	50, 2450, 50	100, 2250, 50
2.	2.0	3, 10, 50	2	152	50, 2450, 50	100, 2000, 50
3.	12.5	3, 10, 50	2	392	50, 2250, 50	100, 1785, 50
4.	50.0	3,10,50	2	792	50, 1300, 50	100, 1480, 50
5.	0.5	3, 5, 50	2	70	50, 2450, 50	100, 2250, 50
6.	0.5	3, 20, 50	2	70	50, 2450, 50	100, 1785, 50
7.	12.5	3, 10, 50	3	320	50, 1300, 50	100, 1785, 50
8.	12.5	5, 10, 50	4	220	50, 1300, 50	100, 1785, 50
9.	10	3, 10, 50	2	20	50, 2285, 50	100, 2225, 50

Liu et al. (2000) [6] used a three dimensional serpentine micro channel design with a “C” shaped repeating units to implement chaotic advection to passively enhance fluid mixing. For comparison, they also used square wave and straight channels. All the above mentioned channels have the cross-section of 300 micron wide and 150 micron depth.

In the aerospace industry, micron-scale supersonic nozzles play an important role in the development of small-scale aircraft and spacecraft. The supersonic nozzle has a throat of approximately 35 micron wide. The thickness of the nozzle is 500 micron. These nozzles are designed for JPL/NASA to be used as micro thrusters on micro-satellites (Bayt et al., 1997 [7]).

Molho et al. (2001) [8] investigated turn geometries for microchip electrophoresis. They performed both numerical analysis and experimentation to propose a dispersion reduction scheme which minimizes dispersion at micro channel turns.

Koning (1997) [9] simulated dilute gas flow through micro channels in which the micro channel upper and lower walls have sinusoidal shapes. In their work, they compared

the pressure profiles obtained through the Reynolds equation and Direct Simulation Monte Carlo method.

Shrewsbury et al. (2001) [10] worked on understanding the transport, orientation and deformation of biological macromolecules by flow when the fluid goes from a micro reservoir into the micro channel (300 micron width, 60 micron depth and length 8 mm) and comes out of the micro channel into the micro reservoir. This results in contraction flow at the inlet of the micro channel and expansion flow at the exit of the micro channel.

Knight et al. (1998) [11] did experiments on hydrodynamic focusing in a micro channel. They used the intersection of four rectangular micro channels of depth 10 micron and width 10 micron. The width of the inlet micro channels tapered to 2 micron abutting the intersection resulting in the formation of nozzle.

Zahn et al. (2000) [12] worked with micro needles in which the width of the micro channel got tapered. The micro needle width = 160 micron and height 110 micron. The other micro needle used is 192 micron wide, 110 micron height and 7 mm length.

Branebjerg et al. (1996) [13] demonstrated that adding complexity to the flow field has the potential to increase the amount of mixing between streams.

2.2 Experimental Studies of flow through Micro channels

Despite the fundamental simplicity of laminar flow in micro channels, experimental studies of micro scale flow have often failed to reveal the expected relationship between friction factor and Reynolds number. Further, flow discrepancies are neither consistently higher nor lower than macro scale predictions. A summary of the experiments that have been conducted to investigate the behavior of fluid flow in micro channels, over a large

range of Reynolds numbers, geometries, and experimental conditions, is presented in table 2.3.

Table 2.3: Experimental conditions for flow resistance experiments. Note when a range of values for channel dimension is given, it indicates that several channels were used with different individual dimensions.

Study	Working fluid	Channel description	Re
Choi (1991) [14]	Nitrogen gas	Circular: diameter 3-81 micron	~ 30 – 20000
Flockhart and Dhariwal (1998) [15]	Water	Trapezoidal: depth 27-63 micron, width 100 -1000 micron, length 12-36 mm	< 600
Jiang et al. (1995) [16]	Water	Circular: diameter 8 – 42 micron. Rectangular, trapezoidal and triangular: depth 13.4 – 46 micron, width 35 – 110 micron, length 2.5 – 10 mm.	Circular: <~ 1.2. Unclear for other geometries.
Mala and Li (1999) [17]	Water	Circular: diameter 50 – 254 micron	Up to 2500
Papautsky et al. (1999a) [18]	Water	Array of rectangular channels, each: depth 30 micron, width 600 micron, length 3mm	1 – 18
Papautsky et al. (1999b) [19]	Water	Array of rectangular channels: height 22.71 – 26.35 micron, width 150 – 600 micron, length 7.75 mm	0.001 – 10
Peng et al. (1994) [20]	Water	Rectangular: height 100 – 300 micron, width 200 – 400 micron, length 50 mm	50 – 40,000
Pfahler et al. (1991) [21]	N – propanol, silicone oil, nitrogen gas, helium gas	Rectangular and trapezoidal, depending upon channel: depth 0.48 – 38.7 micron, width 55 – 115 micron, length 10.2 -10.9 micron	Liquids: << 1-~80
Qu et al. (2000) [22]	Water	Trapezoidal: depth 28 – 114 micron, width 148 – 523 micron, length 28 mm	~ 10 – 1450
Sharp et al. (2000) [23]	Water	Circular: diameter 75 – 245 micron	50 – 2500
Tuckerman and Pease (1981) [24]	Water	Array of etched rectangular/trapezoidal, each: depth 50 – 56 micron,	~ 200 – 600

		width 287 – 320 micron, length 1 cm	
Wilding et al. (1994) [25]	Water, biological fluids	Trapezoidal: depth 20 – 40 micron, width 40 – 150 micron, length 11.7 mm	Water: 17 – 126
Wu and Little (1983) [26]	Nitrogen, helium, argon	Trapezoidal or U-shaped: depth 28 – 65 micron, width 133 – 200 micron, length 7.6 – 40.3 mm	~ 200 – 15,000
Yu et al. (1995) [27]	Nitrogen gas, water	Circular: diameter 19-102 micron	250 – 20,000

Significant differences in studies for deviation in the behavior of fluid from continuum macro scale theory have been reported. Sharp et al. (2001) [28] have shown that in the range of accepted laminar flow behavior, the friction factor agrees with classical continuum hydrodynamic theory with negligible differences. Transition to turbulence occurs at Re = 2000. However large differences in pressure drop in micro channels have been reported by many investigators. These differences may be due to imperfections in the flow system for the experiment. Different kinds of imperfections are :- (1) Variation in the desired dimensions of the micro channel (2) Impurity which can settle inside the micro channel during covering procedure like anodic bonding and (3) Leakage which can occur due to faulty sealing while applying covering procedure like anodic bonding. Since imperfections may well occur in real engineering systems, it is essential to understand the sources of the observed discrepancies in order to avoid them, control them, or convert them into designs.

2.3 Two-depth and two-width micro channels

Although a wide range of different micro total analysis systems (μ-TAS) has been demonstrated [29], efficient standard interconnections between these devices and the

macroscopic world are not yet available [30]. Therefore a new as well as simple micro channel design for conveniently fixing external tubes to the chip is developed in this thesis.

The great assortment of available micro particles and beads and the characteristics of the two-depth and two-width micro channels presented in this thesis open up the possibility to miniaturize many experiments that are today performed in test-tubes and micro-titter plates. In addition, the flow through micro fluidic micro reservoir may have a potential role in applications not involving bead or micro particles, i.e. cell-cell separations, cell deformability tests and particle filtration [31, 32].

Chapter 3: CFD Simulation of two-depth and two-width micro channels

3.1 Overview of Numerical Scheme

The numerical scheme used for simulation is segregated solver method. Using this method, FLUENT will solve the governing integral equations for the conservation of mass and momentum. A control-volume-based technique is used that consists of:

- Division of the domain into discrete control volumes using a computational grid.
- Integration of the governing equations on the individual control volumes to construct algebraic equations for the discrete dependent variables (``unknowns'') such as velocities, pressure, and conserved scalars.
- Linearization of the discretized equations and solution of the resultant linear equation system to yield updated values of the dependent variables.

3.1.1 Segregated Solution Method

Using this approach, the governing equations are solved sequentially (i.e., segregated from one another). Because the governing equations are non-linear, several iterations of the solution loop must be performed before a converged solution is obtained. Each iteration consists of the steps illustrated in Figure 3.1:

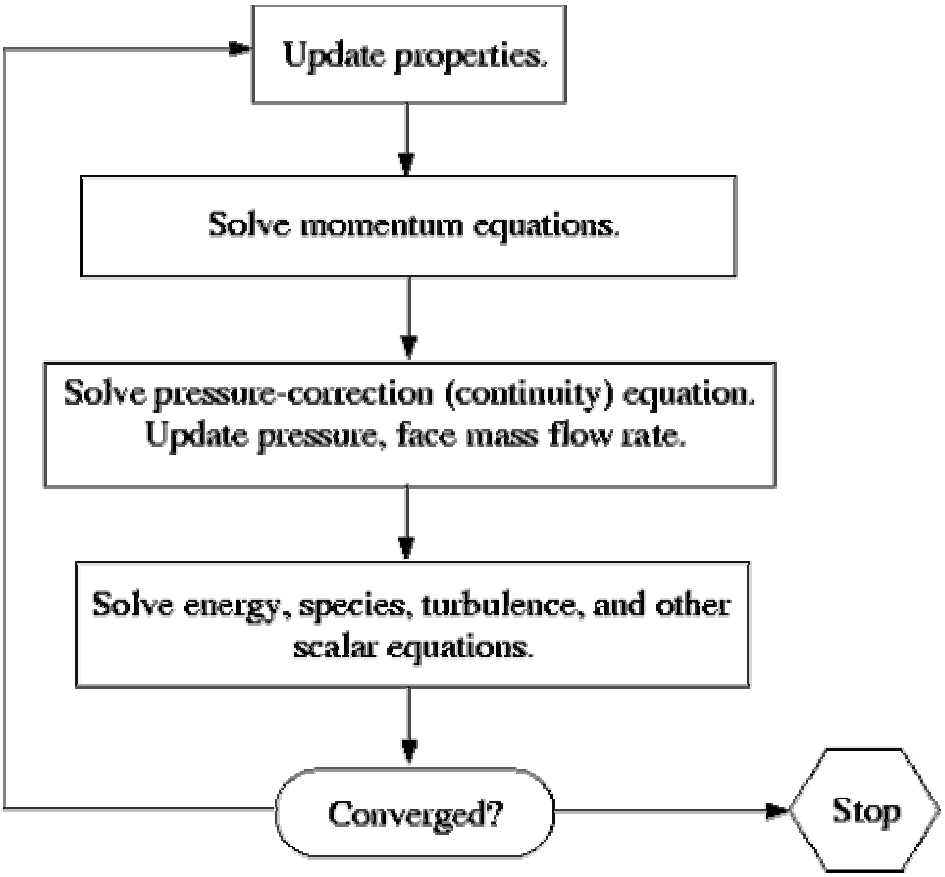

Figure 3.1: Overview of the Segregated Solution Method

3.1.2 Linearization

The manner in which the governing equations are linearized may take an ``implicit'' or ``explicit'' form with respect to the dependent variable (or set of variables) of interest.

- Implicit linearization: For a given variable, the unknown value in each cell is computed using a relation that includes both existing and unknown values from neighboring cells. Therefore each unknown will appear in more than one equation in the system, and these equations must be solved simultaneously to give the unknown quantities.

- Explicit linearization: For a given variable, the unknown value in each cell is computed using a relation that includes only existing values. Therefore each unknown will appear in only one equation in the system and the equations for the unknown value in each cell can be solved one at a time to give the unknown quantities.

In the segregated solution method each discrete governing equation is linearized implicitly with respect to that equation's dependent variable. This will result in a system of linear equations with one equation for each cell in the domain. Because there is only one equation per cell, this is sometimes called a ``scalar'' system of equations.

3.1.3 Discretization

FLUENT uses a control-volume-based technique to convert the governing equations to algebraic equations that can be solved numerically. This control volume technique consists of integrating the governing equations about each control volume, yielding discrete equations that conserve each quantity on a control-volume basis.

Discretization of the governing equations can be illustrated most easily by considering the steady-state conservation equation for transport of a scalar quantity ϕ . This is demonstrated by the following equation written in integral form for an arbitrary control volume V as follows:

$$\oint \rho \phi \vec{v} \cdot d\vec{A} = \oint \Gamma_{\phi} \nabla \phi \cdot d\vec{A} + \int_{V} S_{\phi} dV \tag{3.1}$$

where ρ is density, $\vec{v}$ is velocity vector, $\vec{A}$ is surface area vector, Γ_ϕ is the diffusion coefficient for ϕ, $\nabla\phi$ is the gradient of ϕ, and S_ϕ is the source of ϕ per unit volume. Equation (3.1) is applied to each control volume, or cell, in the computational domain. The two-dimensional, triangular cell shown in Figure 3.2 is an example of such a control volume. Discretization of Equation (3.1) on a given cell yields

$$\sum_f^N \rho_f \vec{v}_f \phi_f \cdot \vec{A}_f = \sum_f^N \Gamma_\varphi (\nabla\phi)_n \cdot \vec{A}_f + S_\phi V \tag{3.2}$$

where N is the number of faces enclosing cell, ϕ_f is the value of ϕ convected through face f, $\rho_f \vec{v}_f \cdot \vec{A}_f$ is the mass flux through the face, $\vec{A}_f$ is the area of face f, $(\nabla\phi)_n$ is the magnitude of $\nabla\phi$ normal to face f, and V is the cell volume.

The equations solved by FLUENT take the same general form as the one given above and apply readily to multi-dimensional, structured as well as unstructured meshes composed of arbitrary polyhedra.

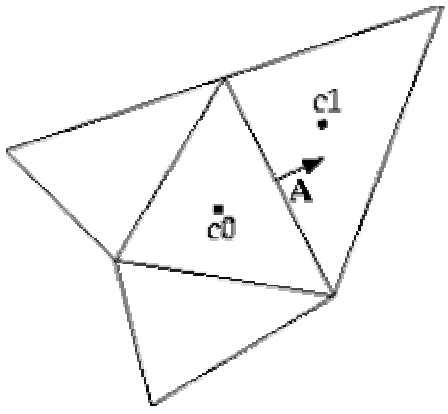

Figure 3.2: Control Volume Used to Illustrate Discretization of a Scalar Transport

FLUENT stores discrete values of the scalar ϕ at the cell centers ($c0$ and $c1$ in Figure 3.2). However, face values ϕ_f are required for the convection terms in Equation (3.2) and must be interpolated from the cell center values. This is accomplished using an upwind scheme. Upwinding means that the face value ϕ_f is derived from quantities in the cell upstream, or ``upwind," relative to the direction of the normal velocity v_n in Equation (3.2).

3.1.3.1 First-Order Upwind Scheme

When first-order accuracy is desired, quantities at cell faces are determined by assuming that the cell-center values of any field variable represent a cell-average value and hold throughout the entire cell; the face quantities are identical to the cell quantities. Thus when first-order upwinding is selected, the face value ϕ_f is set equal to the cell-center value of ϕ in the upstream cell.

3.1.3.2 Under-Relaxation

Because of the nonlinearity of the equation set being solved by FLUENT, it is necessary to control the change of ϕ. This is typically achieved by under-relaxation, which reduces the change of ϕ produced during each iteration. In a simple form, the new value of the variable ϕ within a cell depends upon the old value, ϕ_{old}, the computed change in ϕ, $\Delta\phi$, and the under-relaxation factor, α, as follows:

$$\phi = \phi_{old} + \alpha\Delta\phi \tag{3.3}$$

3.1.3.3 Temporal Discretization

The spatial discretization for the time-dependent equations is identical to the steady-state case. Temporal discretization involves the integration of every term in the differential equations over a time step Δt. The integration of the transient terms is straightforward, as shown below.

A generic expression for the time evolution of a variable ϕ is given by

$$\frac{\partial \phi}{\partial t} = F(\phi) \tag{3.4}$$

where the function F incorporates any spatial discretization. If the time derivative is discretized using backward differences, the first-order accurate temporal discretization is given by

$$\frac{\phi^{n+1} - \phi^{n}}{\Delta t} = F(\phi) \tag{3.5}$$

and the second-order discretization is given by

$$\frac{3\phi^{n+1} - 4\phi^{n} + \phi^{n-1}}{2\Delta t} = F(\phi) \tag{3.6}$$

where

n+1 is the value at the next time interval t+Δt, n is the value at the current time level t and n-1 is the value at the previous time level t-Δt.

$F(\phi)$at the future time level is given by,

$$\frac{\phi^{n+1}-\phi^{n}}{\Delta t}=F\left(\phi^{n+1}\right) \text{ or,} \tag{3.7}$$

$$\phi^{n+1}=\phi^{n}+\Delta tF\left(\phi^{n+1}\right) \tag{3.8}$$

The equation can be solved iteratively by initializing ϕ^{i} to ϕ^{n} and iterating the equation

$$\phi^{i}=\phi^{n}+\Delta tF\left(\phi^{i}\right) \tag{3.9}$$

for the first-order implicit formulation, or

$$\phi^{i}=4/3\phi^{n}-1/3\phi^{n-1}+2/3\Delta tF\left(\phi^{i}\right) \tag{3.10}$$

for the second-order implicit formulation, until ϕ^{i} stops changing (i.e., converges). At that point, ϕ^{n+1} is set to ϕ^{i}.

The advantage of this scheme is that it is unconditionally stable with respect to time step size.

3.1.4 The Segregated Solver

In this section, special practices related to the discretization of the momentum and continuity equations and their solution by means of the segregated solver are addressed. These practices are most easily described by considering the steady-state continuity and momentum equations in integral form:

$$\oint \rho\vec{v}\cdot d\vec{A}=0 \tag{3.11}$$

$$\oint \rho\vec{v}\vec{v}\cdot d\vec{A}=-\oint pI\cdot d\vec{A}+\oint\overline{\overline{\tau}}\cdot d\vec{A}+\int_{V}\vec{F}dV \tag{3.12}$$

where I is the identity matrix, $\overline{\overline{\tau}}$ is the stress tensor, and $\vec{F}$ is the force vector.

3.1.4.1 Discretization of the Momentum Equation

The discretization scheme described in Section 3.1.3 for a scalar transport equation is also used to discretize the momentum equations. For example, the *x*-momentum equation can be obtained by setting $\phi = u$:

$$a_P u = \sum_{nb} a_{nb} u_{nb} + \sum p_f A \cdot \hat{i} + S \tag{3.13}$$

If the pressure field and face mass fluxes were known, Equation (3.13) could be solved in the manner outlined in Section 3.1.3, and a velocity field obtained. However, the pressure field and face mass fluxes are not known a priori and must be obtained as a part of the solution. FLUENT uses a co-located scheme, whereby pressure and velocity are both stored at cell centers. However, Equation (3.13) requires the value of the pressure at the face between cells *c*0 and *c*1, shown in Figure 3.2. The Pressure Interpolation Scheme in FLUENT interpolates the pressure values at the faces using momentum equation coefficients [39].

3.1.4.2 Discretization of the Continuity Equation

Equation (3.11) may be integrated over the control volume in Figure 3.2 to yield the following discrete equation

$$\sum_{f}^{N} J_f A_f = 0 \tag{3.14}$$

where J_f is the mass flux through face f, ρv_n .

As described in Section 3.1.1, the momentum and continuity equations are solved sequentially. In this sequential procedure, the continuity equation is used as an equation for pressure. However, pressure does not appear explicitly in Equation (3.14) for incompressible flows, since density is not directly related to pressure. The SIMPLE (Semi-Implicit Method for Pressure-Linked Equations) family of algorithms [40] is used for introducing pressure into the continuity equation.

In order to proceed further, it is necessary to relate the face values of velocity, $\vec{v}_n$, to the stored values of velocity at the cell centers. The face value of velocity is not averaged linearly; instead, momentum-weighted averaging, using weighting factors based on the a_P coefficient from equation (3.13), is performed. Using this procedure, the face flux, J_f, may be written as

$$J_f = \hat{J}_f + d_f\left(p_{c0} - p_{c1}\right) \tag{3.15}$$

where p_{c0} and p_{c1} are the pressures within the two cells on either side of the face, and $\hat{J}_f$ contains the influence of velocities in these cells (see Figure 3.2). The term d_f is a function of $\overline{a}_P$, the average of the momentum equation a_P coefficients for the cells on either side of face *f*.

3.1.4.3 Pressure-Velocity Coupling

Pressure-velocity coupling is achieved by using Equation (3.15) to derive an equation for pressure from the discrete continuity equation (Equation (3.14)). The SIMPLE algorithm

uses a relationship between velocity and pressure corrections to enforce mass conservation and to obtain the pressure field.

If the momentum equation is solved with a guessed pressure field p^*, the resulting face flux, J^*_f, computed from Equation (3.15)

$$J_f^* = \hat{J}_f^* + d_f\left(p_{c0}^* - p_{c1}^*\right) \tag{3.16}$$

does not satisfy the continuity equation. Consequently, a correction J'_f is added to the face flux J^*_f so that the corrected face flux, J_f

$$J_f = J_f^* + J_f' \tag{3.17}$$

satisfies the continuity equation. The SIMPLE algorithm postulates that J'_f be written as

$$J_f' = d_f\left(p_{c0}' - p_{c1}'\right) \tag{3.18}$$

where p' is the cell pressure correction.

The SIMPLE algorithm substitutes the flux correction equations (Equations (3.17) and (3.18)) into the discrete continuity equation (Equation (3.14)) to obtain a discrete equation for the pressure correction p' in the cell:

$$a_P p' = \sum_{nb} a_{nb} p'_{nb} + b \tag{3.19}$$

where the source term b is the net flow rate into the cell:

$$b = \sum_{f}^{N} J_f^* A_f \tag{3.20}$$

The cell pressure and the face flux are corrected using

$$p = p^{*} + \alpha_{p} p' \tag{3.21}$$

$$J_{f} = J_{f}^{*} + d_{f}\left(p'_{c0} - p'_{c1}\right) \tag{3.22}$$

Here α_p is the under-relaxation factor for pressure. The corrected face flux, J_f, satisfies the discrete continuity equation identically during each iteration.

3.2 Eulerian Model

The Eulerian model is the most complex of the multiphase models in FLUENT. It solves a set of momentum and continuity equations for each phase. Coupling is achieved through the pressure and interphase exchange coefficients. The manner in which this coupling is handled depends upon the type of phases involved; granular (fluid-solid) flows are handled differently than non-granular (fluid-fluid) flows. For granular flows , the properties are obtained from application of kinetic theory. Momentum exchange between the phases is also dependent upon the type of mixture being modeled.

To change a single-phase model, where a single set of conservation equations for momentum and continuity is solved, to two phase model, additional sets of conservation equations must be introduced. The modifications involve, among other things, the introduction of the volume fractions α_1 and α_2 for primary (fluid) and secondary (particle) phases, as well as a mechanism for the exchange of momentum between these phases.

3.2.1 Volume Fractions

The description of two phase flow as interpenetrating continua incorporates the concept of phasic volume fractions , denoted here by α_1 and α_2. Volume fractions represent the space occupied by each phase, and the laws of conservation of mass and momentum are satisfied by each phase individually. The volume of phase q, V_q, is defined by

$$V_q = \int_V \alpha_q dV \tag{3.23}$$

where

$$\sum_{q=1}^{2} \alpha_q = 1 \tag{3.24}$$

The effective density of phase q is

$$\hat{\rho}_q = \alpha_q \rho_q \tag{3.25}$$

where ρ_q is the physical density of phase q.

3.2.2 Equations Solved by FLUENT

The equations for granular two phase flows, as solved by FLUENT, are presented here.

3.2.2.1 Continuity Equation

The volume fraction of phase1 is calculated from a continuity equation:

$$\frac{\partial}{\partial t}(\alpha_1) + \nabla \cdot (\alpha_1 \vec{v}_1) = \frac{1}{\rho_1}\left(\dot{m}_{21} - \alpha_1 \frac{d_1 \rho_1}{dt} \right) \tag{3.26}$$

The solution of this equation for each secondary phase, along with the condition that the volume fractions sum to one (given by Equation (3.24)), allows for the calculation of the primary-phase volume fraction.

3.2.2.2 Fluid-Solid Momentum Equations

FLUENT uses a multi-fluid granular model to describe the flow behavior of a fluid-solid mixture. The solid-phase stresses are derived by making an analogy between the random particle motions arising from particle-particle collisions taking into account the inelasticity of the granular phase. The kinetic energy associated with the particle velocity fluctuations is represented by a ``pseudothermal" or granular temperature which is proportional to the mean square of the random motion of particles.

The conservation of momentum for a fluid phase1 is

$$\begin{aligned}&\frac{\partial}{\partial t}\left(\alpha_1\rho_1\vec{v}_1\right)+\nabla\cdot\left(\alpha_1\rho_1\vec{v}_1\vec{v}_1\right)\\&=-\alpha_1\nabla p+\nabla\cdot\overline{\overline{\tau}}_1+\alpha_1\rho_1\vec{g}+\alpha_1\rho_1\left(\vec{F}_1+\vec{F}_{lift,1}+\vec{F}_{vm,1}\right)+K_{21}\left(\vec{v}_2-\vec{v}_1\right)+\dot{m}_{21}\vec{v}_{21}\end{aligned} \tag{3.27}$$

Here p is the pressure shared by both phases, $\vec{g}$ is the acceleration due to gravity, $\vec{F}_1$ is the external body force, $\vec{F}_{lift,1}$ is a lift force, and $\vec{F}_{vm,1}$ is the virtual mass force. $\overline{\overline{\tau}}_1$ is the phase1 stress-strain tensor and is given by

$$\overline{\overline{\tau}}_1=\alpha_1\mu_1\left(\nabla\vec{v}_1+\nabla\vec{v}_1^{\,T}\right)+\alpha_1\left(\lambda_1-\frac{2}{3}\mu_1\right)\nabla\cdot\vec{v}_1\overline{\overline{I}} \tag{3.28}$$

where μ_1 and λ_1 are shear and bulk viscosity of phase1,

$$F_{lift} = -0.5\rho_1\alpha_2\left|\vec{v}_1 - \vec{v}_2\right| \times \left(\nabla \times \vec{v}_1\right) \tag{3.29}$$

$$F_{lift,1} = -F_{lift,2} \tag{3.30}$$

and that for the phase 2 is

$$\begin{aligned} &\frac{\partial}{\partial t}\left(\alpha_2\rho_2\vec{v}_2\right) + \nabla\cdot\left(\alpha_2\rho_2\vec{v}_2\vec{v}_2\right) \\ &= -\alpha_2\nabla p - \nabla p_2 + \nabla\cdot\overline{\overline{\tau}}_2 + \alpha_2\rho_2\vec{g} + \alpha_2\rho_2\left(\vec{F}_2 + \vec{F}_{lift,2} + \vec{F}_{vm,2}\right) + K_{12}\left(\vec{v}_1 - \vec{v}_2\right) + \dot{m}_{12}\vec{v}_{12} \end{aligned} \tag{3.31}$$

where p_2 is the solid pressure, K_{12} is the momentum exchange coefficient between fluid phase1 and solid phase2, and $\vec{F}_2$ is the external body force, $\vec{F}_{lift,2}$ is a lift force, and $\vec{F}_{vm,2}$ is the virtual mass force. $\overline{\overline{\tau}}_2$ is the phase2 stress-strain tensor.

$$F_{vm} = 0.5\alpha_1\rho_1\left(\frac{d_1 v_1}{dt} - \frac{d_2 v_2}{dt}\right) \tag{3.32}$$

where $\frac{d_1}{dt}$ denotes the phase material time derivative of the form

$$\frac{d_1}{dt}(\phi) = \frac{\partial}{\partial t}(\phi) + (\vec{v}_1\cdot\nabla)\phi \tag{3.33}$$

The fluid-solid exchange coefficient K_{21} can be written in the following general form:

$$K_{21} = \frac{\alpha_2\rho_2 f}{\tau_2} \tag{3.34}$$

where f is defined differently for the different exchange-coefficient models (as described below), and τ_2, the ``particulate relaxation time'', is defined as

$$\tau_2 = \frac{\rho_2 d_2^2}{18\mu_1} \tag{3.35}$$

where d_2 is the diameter of particles of phase2.

All definitions of f include a drag function (C_D) that is based on the relative Reynolds number (Re_2). It is this drag function that differs among the exchange-coefficient models.

- The Gidaspow model

When $\alpha_1 > 0.8$, the fluid-solid exchange coefficient K_{21} is of the following form:

$$K_{21} = \frac{3}{4} C_D \frac{\alpha_2 \alpha_1 \rho_1 \left|\vec{v}_2 - \vec{v}_1\right|}{d_2} \alpha_1^{-2.65} \tag{3.36}$$

where

$$C_D = \frac{24}{\alpha_1 \mathrm{Re}_2}\left[1 + 0.15(\alpha_1 \mathrm{Re}_2)^{0.687}\right] \tag{3.37}$$

When $\alpha_1 \leq 0.8$

$$K_{21} = 150\frac{\alpha_2(1-\alpha_1)\mu_1}{\alpha_1 d_2^2} + 1.75\frac{\rho_1 \alpha_2 \left|\vec{v}_2 - \vec{v}_1\right|}{d_2} \tag{3.38}$$

3.2.3 Solution Method in FLUENT

For Eulerian multiphase calculations, FLUENT uses the Phase Coupled SIMPLE (PC-SIMPLE) algorithm [41] for the pressure-velocity coupling. PC-SIMPLE is an extension of the SIMPLE algorithm [40] to multiphase flows. The velocities are solved coupled by

phases, but in a segregated fashion. Then, a pressure correction equation is built based on total volume continuity rather than mass continuity. Pressure and velocities are then corrected so as to satisfy the continuity constraint.

3.2.3.1 The Pressure-Correction Equation

For incompressible two phase flow, the pressure-correction equation takes the form

$$\sum_{k=1}^{2}\left\{\frac{\partial}{\partial t}\alpha_k + \nabla\cdot\alpha_k\vec{v}_k' + \nabla\cdot\alpha_k v_k^* - \frac{1}{\rho_k}\sum_{l=1}^{2}\dot{m}_{lk}\right\} = 0 \tag{3.39}$$

where $\vec{v}_k'$ is the velocity correction for the phase k and $\vec{v}_k^*$ is the value of $\vec{v}_k$ at the current iteration. The velocity corrections are themselves expressed as functions of the pressure corrections.

3.3 Two-phase flow in two-depth and two-width micro channels

For investigation, nineteen different designs of two-depth and two-width micro channels are considered. Variations in micro reservoir positions from the inlet are considered, variations in the depth of first channel, micro reservoir and shallow channel are considered and variation in the cross-section of the micro reservoir for different widths of first channel are considered. The designs for various cases considered are listed in Table 3.1-3.6. Different models of the two-depth and two-width micro channels (Figure 3.3), used in this study, are tabulated from table 3.1 to 3.6 below. The models were named from A1 to A19.

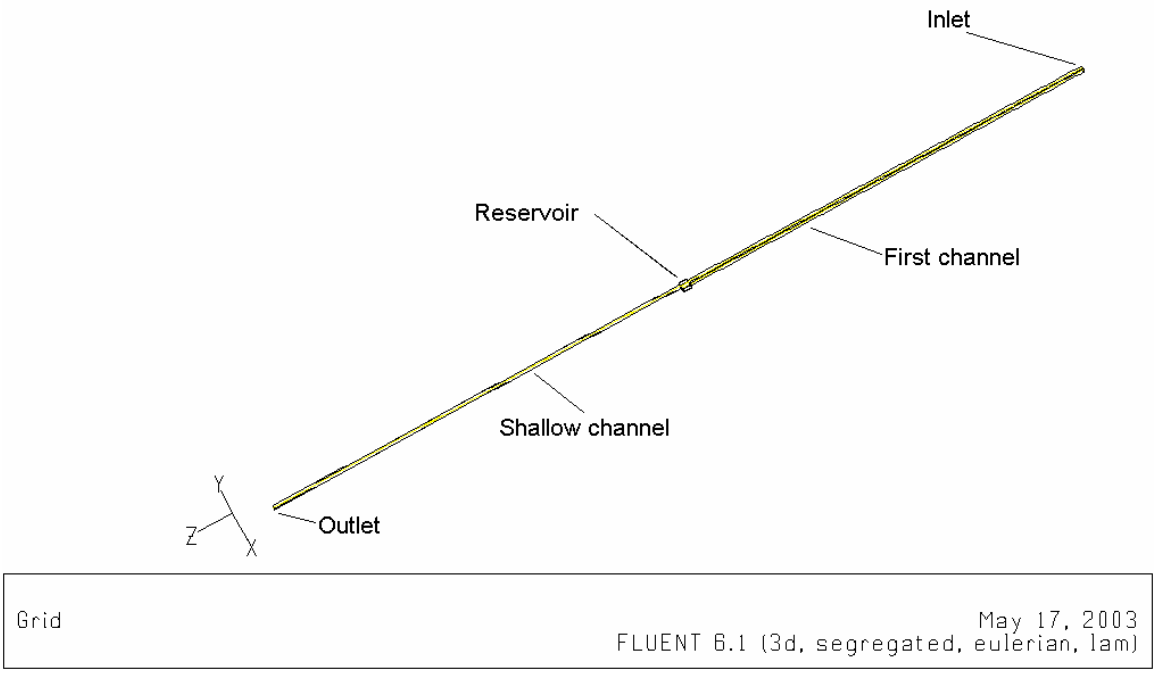

Figure 3.3 One of the two depth and two width micro channel designs used in the simulation work.

Table 3.1: Varying the position of the micro reservoir from the center of the micro channel with the difference of 2000 micron.

Case No.	Name of the models	First Channel			Micro reservoir			Shallow Channel		
		Depth (μm)	Width (μm)	Length (μm)	Depth (μm)	Width (μm)	Length (μm)	Depth (μm)	Width (μm)	Length (μm)
1.	A1	100	100	9900	100	200	200	5	100	9900
2.	A2	100	100	11900	100	200	200	5	100	7900
3.	A3	100	100	13900	100	200	200	5	100	5900
4.	A4	100	100	15900	100	200	200	5	100	3900

Table 3.2: Varying the first channel depth and micro reservoir depth (250 micron and 400 micron) keeping the shallow channel depth = 5 micron

Case No.	Name of the models	First Channel			Micro reservoir			Shallow Channel		
		Depth (μm)	Width (μm)	Length (μm)	Depth (μm)	Width (μm)	Length (μm)	Depth (μm)	Width (μm)	Length (μm)
1.	A5	250	100	9900	250	200	200	5	100	9900
2.	A6	400	100	9900	400	200	200	5	100	9900

Table 3.3: Varying the first channel depth and micro reservoir depth (200 micron, 250 micron and 400 micron) keeping the shallow channel depth = 3 micron

Case No.	Name of the models	First Channel			Micro reservoir			Shallow Channel		
		Depth (μm)	Width (μm)	Length (μm)	Depth (μm)	Width (μm)	Length (μm)	Depth (μm)	Width (μm)	Length (μm)
1.	A7	100	100	9900	100	200	200	3	100	9900
2.	A8	250	100	9900	250	200	200	3	100	9900
3.	A9	400	100	9900	400	200	200	3	100	9900

Table 3.4: Varying cross-section of the micro reservoir (100 micron, 150 micron, 250 micron) with first channel width = shallow channel width = 100 micron

Case No.	Name of the models	First Channel			Micro reservoir			Shallow Channel		
		Depth (μm)	Width (μm)	Length (μm)	Depth (μm)	Width (μm)	Length (μm)	Depth (μm)	Width (μm)	Length (μm)
1.	A10	100	100	9900	100	250	250	5	100	9850
2.	A11	100	100	9900	100	150	150	5	100	9950
3.	A12	100	100	9900	100	100	100	5	100	10000

Table 3.5: Varying the cross-section of the micro reservoir (150 micron, 200 micron, 250 micron) with first channel width = shallow channel width = 150 micron

Case No.	Name of the models	First Channel			Micro reservoir			Shallow Channel		
		Depth (μm)	Width (μm)	Length (μm)	Depth (μm)	Width (μm)	Length (μm)	Depth (μm)	Width (μm)	Length (μm)
1.	A13	100	150	9900	100	150	150	5	150	9950
2.	A14	100	150	9900	100	200	200	5	150	9900
3.	A15	100	150	9900	100	250	250	5	150	9850

Table 3.6: Varying the cross-section of the micro reservoir (70 micron, 100 micron, 150 micron, 250 micron) with first channel width = shallow channel width = 70 micron

Case No.	Name of the models	First Channel			Micro reservoir			Shallow Channel		
		Depth (μm)	Width (μm)	Length (μm)	Depth (μm)	Width (μm)	Length (μm)	Depth (μm)	Width (μm)	Length (μm)
1.	A16	100	70	9900	100	70	70	5	70	10030
2.	A17	100	70	9900	100	100	100	5	70	10000
3.	A18	100	70	9900	100	150	150	5	70	9950
4.	A19	100	70	9900	100	250	250	5	70	9850

The particles considered for the flow have the density of 1500 kg/m^3 and diameter of 1 micron. The fluid considered is water with the density of 998 kg/m^3. The flow field is initialized with micro-particles volume fraction of 0.02, which is also called volume fraction patching. All the contours of volume fraction variation of micro particles in the micro reservoir were determined under steady state condition. The pressure at the inlet

was maintained constant at 200 kPa which is sufficient to give a proper initialization for flow field in all the models.

3.4 CFD Analysis Considerations

CFD Analysis of Two-depth and Two-width micro channels has been given the following considerations:-

1. Modeling Goals
2. Computational Geometry
3. Physical Model
4. Solution Procedure

3.4.1 Modeling Goals

As mentioned, the objective of this CFD analysis is to simulate the two phase flow through different geometries of two-depth and two-width micro channels using a commercial CFD package. A study of the effects of varying dimensional parameters of micro channel on pressure distribution along its length, centerline velocity magnitudes along its length, contours of volume fraction of phase2 in the micro reservoir, path lines followed by the particles in the micro reservoir injected from the inlet face and the mass flux delivered.

The CFD package used to accomplish these goals is FLUENT 6.0, which is based on the finite volume method to analyze flow in specified domain. It is an opportunity to study one of the wide range of applications of this software in the engineering field.

The models were developed with a level of sophistication chosen to predict the actual performance of the system with sufficient accuracy, while keeping the degree of

complexity to a manageable level. This is usually accomplished by making reasonable, simplifying assumptions. All the considerations in developing the models are presented here along with a brief justification.

3.4.2 Computational Geometry

1. Isolation of a piece of the complete physical model: The complete physical model of two-depth and two-width micro channels is isolated by the walls of the micro channel, the inlet face and the outlet face.
2. Defining the computational domain: The computational domain is the entire volume of the micro channel from inlet to outlet.
3. Boundary conditions used at the boundary of the model: The flow in the micro channel is bounded by the following boundary conditions:-

a) A constant pressure of 200 kPa distributed uniformly over the entire surface of inlet face.

b) A constant pressure of 0 Pa distributed uniformly over the entire surface of outlet face.

c) The channel is divided into two halves by the plane of symmetry which runs parallel to the side walls of the channel.

d) The flow is confined by the walls of the micro channel and the line of symmetry.

4. Defining the coordinate system of the model: The coordinate system of the model must be the three dimensional Cartesian coordinate system. This helps to understand the contours of volume fraction of phase2 in the micro reservoir and path lines followed by particles in the micro reservoir injected from the inlet face. The length is along the positive direction of z-axis, the depth along the negative direction of y-axis and the width along the x-axis.

5. Selecting the best grid topology: Since the volume consists of three different rectangular volumes in series, the most suitable grid topology or meshing scheme type is “map” which consists of hexahedral elements (Figure 3.4) with nodes at each corner of the cell. To get a better picture in the micro reservoir section, higher density of these elements is required in the micro reservoir region than in the first channel and the shallow channel.

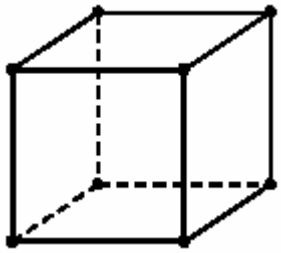

Figure 3.4: The hexahedral meshing element with eight nodes at the corners.

3.4.3 Physical Model

1. Flow through the micro channels: Flow through the micro channels at 200 kPa of the above mentioned dimensions remains laminar when the expected Reynolds number lies between 0.1 and 10. The simulation results also confirm that the Re number for such micro channels can never allow turbulence in any part of the channel.
2. Steady state flow condition: The solution in this analysis is taken for the steady state flow condition.
3. The effect of gravity and other body forces is unimportant: Since natural convection is negligible, orientation is unimportant. Also, gravity is not a hydrodynamic concern since the flow passage is confined and does not have a free surface.

4. The fluid motion obeys the Navier-Stokes equations and the fluid is modeled as a continuum: This states that the fluid behaves as a Newtonian fluid and follows a continuum approach. Water is known to act as Newtonian fluid.
5. The incompressible medium: The fluid used is water and is incompressible.
6. The particles mostly available in the market are spherical in shape and have the material density ranging from 1200 kg/m^3 to 2000 kg/m^3: The particles are taken with diameter of 1 micron and density of 1500 kg/m^3.
7. No-slip condition is satisfied : The velocity of the fluid at the walls are zero.

3.4.4 Solution Procedure

1. The problem can be solved by simply, using the default solver formulation and solution parameters.

a) The governing equations for the segregated solver do not contain any time-dependent terms if we are performing steady state calculations,

b) For a simple flow that is aligned with the grid (e.g. laminar flow in a rectangular duct modeled with a quadrilateral or hexahedral grid) the numerical diffusion will be naturally low, so we can generally use the first-order scheme instead of second order scheme without any significant loss of accuracy.

c) The segregated solver uses under-relaxation to control the update of computed variables at each iteration. This means that all equations solved using the segregated solver will have under-relaxation factors associated with them. In FLUENT, the default under-relaxation parameters for all variables are set to values that are near optimal for the largest possible number of cases.

d) Pressure-velocity coupling is relevant for the segregated solver. FLUENT provides SIMPLE algorithm for pressure-velocity coupling. Steady state solutions generally use SIMPLE algorithm. For the Eulerian model, the Phase coupled SIMPLE algorithm is used.

e) In order to keep the solution under extreme conditions, FLUENT provides limits that keep the solution within an acceptable range. Typically, it is not necessary to change the default solution limits.

2. The convergence cannot be accelerated with a more judicious solution procedure: When the segregated solver is used, all equations are, by default, solved using the first-order upwind discretization for convection. The first order discretization generally yields better convergence than the second-order scheme.
3. The problem fits within the memory constraints of the computer: The memory given in each directory in the workstations is 1 GB which is quite sufficient for managing the CFD models and their solutions.
4. The problem takes no more than 24 hours to converge on the computer. In addition, the problem can be submitted into the batch queue which allows the jobs to run on the computer servers in the background.

3.5 Modeling and Simulation of the two-depth and two-width micro channel

3.5.1 Modeling of the micro channel

The modeling of flow in micro-channel involves 3 major steps and they are as follows:

1. Definition of computational domain
2. Generation of grid/mesh

3. Definition of boundary conditions.

3.5.1.1 Definition of Computation Domain for the model of micro channel

The geometry was created with the scale of 1 micron = 1 unit. The volume was assigned the Cartesian coordinate system of (+X, +Y, +Z). This makes the entire model volume towards the positive space of the coordinate system. The volumes of the model were created taking into account the later use of symmetry boundary condition as mentioned in section 3.3.1.3. This makes the whole volume to be cut, using the plane of symmetry parallel to the side walls of the micro channel, into two halves and one half of it was used as the model for simulation. Figure 3.5 shows the faces of the grid around the micro reservoir region.

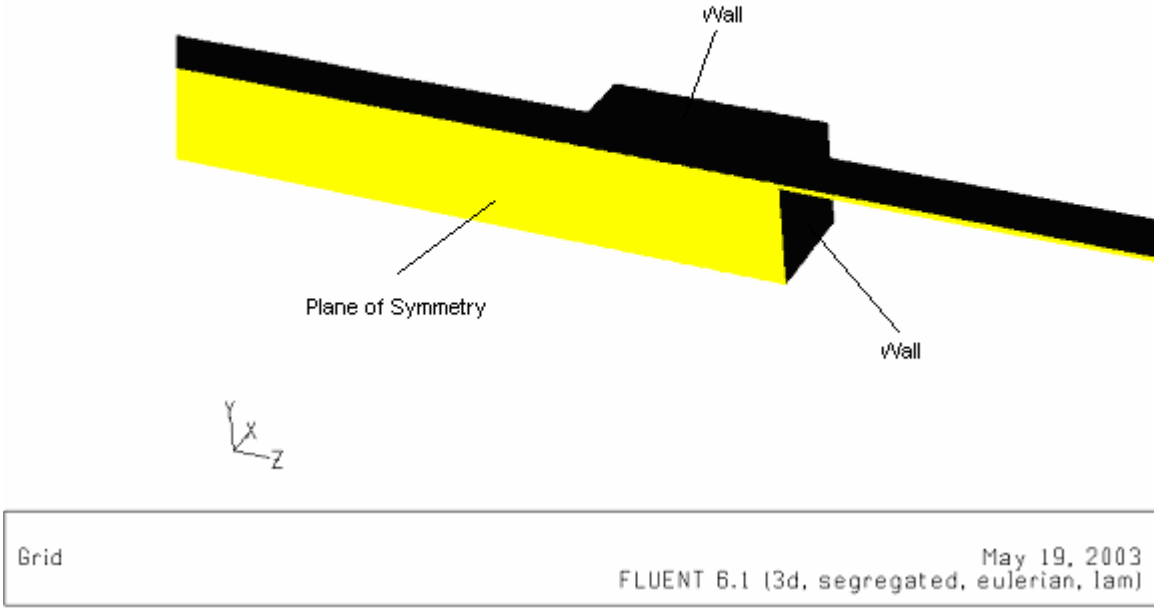

Figure 3.5: Symmetrical half of the grid showing the faces around the micro reservoir region of two-depth two-width micro channel.

3.5.1.2 Generation of Grid with GAMBIT for the model of micro channel

The modeling of the computation domain is done with GAMBIT. The grid topology used is Map i.e. the structured grid with hexahedral meshing elements, Figure 3.6 below shows the meshing scheme used in the simulation of fluid-flow in a micro-channel. The volume of the model is made by uniting the three cuboids of the first channel, micro reservoir and the shallow channel, respectively. While uniting the volumes, the volume of the micro reservoir was retained. This volume was then used to split the united volume into three separate volumes again. This strategy was used to have the common faces between each of the volumes so that the "Map" scheme meshing could be applied to the entire model. Finally the extraneous micro reservoir volume was removed. The meshing of edge is done on the edges of the first channel and shallow channel with the node interval of 100 units. The micro reservoir is meshed using the "Map" scheme with hexahedral elements of 2 nodes (the nodes are only at the corners of the cell) with the node spacing of 4 units (Figure 3.6). Finally, the entire volume was meshed using the same scheme with node spacing of 1 unit. It will be seen that refinement of the grid is possible with this meshing scheme as well.

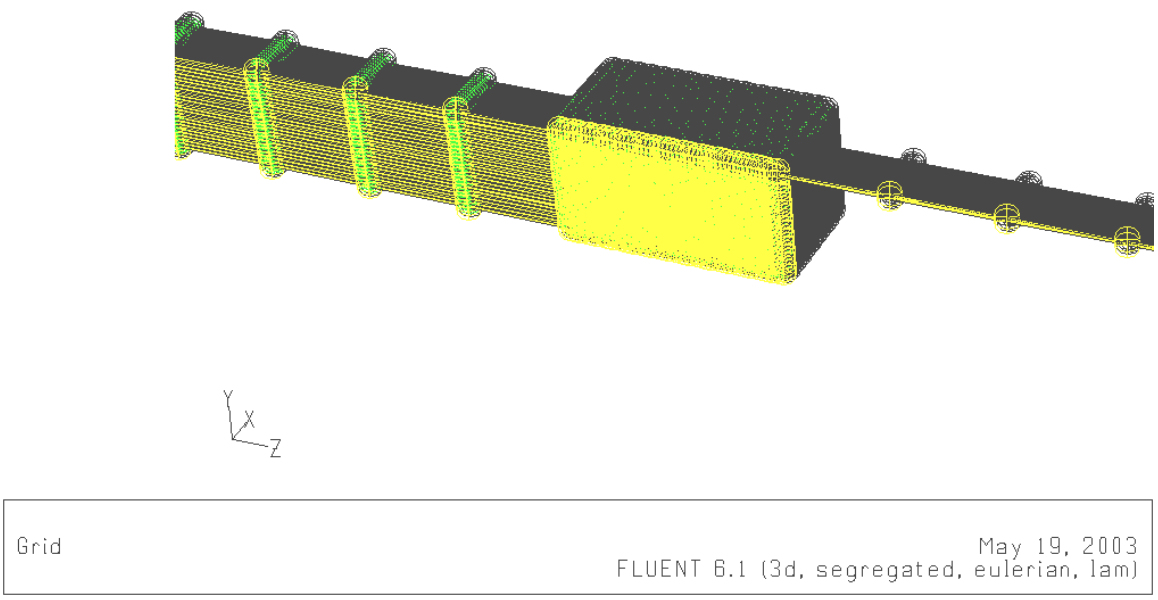

Figure 3.6: Grid/Mesh Used in Simulation

3.5.1.3 Definition of Zone types for the model of micro channel

Zone types define the physical and operational characteristics of the model at its boundaries and within specific regions of its domain. There are two classes of zone type specifications:

(i) Boundary type: - This type defines the characteristic of the model at its external or internal boundaries. Following are the boundary specifications applied in the simulations:

a. Pressure Inlet, named as “inlet”
b. Pressure Outlet, named as “outlet”
c. Plane of Symmetry, named as “symmetry”
d. Confining Walls, named as “walls”

Figure 3.5 also indicates boundary specifications (c) and (d) that were applied in the fluid flow in micro channel simulations. Boundary specification (a) and (b) are not shown. They are at the opposite ends of the model along its length. Changes can also be made to the boundary type when the grid has been read into the solver, FLUENT.

(ii) Continuum type: - This type defines the characteristic of the model within specified regions of its domain. The entire model was given the continuum type as "fluid" and given the name "fluid+particles"

3.5.2 Solution Procedure in FLUENT for Fluid Flow in the micro channel

After reading the mesh file that is obtained from GAMBIT, the steps for successful results are reduced to:

1. Checking Grid
2. Scaling Grid
3. Selecting Appropriate Solver.
4. Defining the Physical Model.
5. Creating Required Materials
6. Specifying Phases
7. Specifying Operating Conditions
8. Specifying Boundary Conditions.
9. Adjusting Solution Control Parameters.

3.5.2.1 Checking Grid: The grid checking capability in FLUENT provides domain extents, volume statistics, grid topology and periodic boundary information, verification of simplex counters, and (for axisymmetric cases) node position verification with respect to

the x-axis. It is generally a good idea to check the grid right after reading into the solver, in order to detect any grid trouble before the problem solution is started.

3.5.2.2 Scaling Grid: The scale grid panel allows to convert the grid from various units of measurements to SI or to apply custom scale factors to the individual coordinates of the grid. The grid is converted into mm units and the scale factor applied to the individual coordinates of the grid is 0.001.

3.5.2.3 Selecting the Appropriate Solver for Fluid Flow in a Micro-Channel

In FLUENT, there is the possibility of choosing either the segregated or coupled solver. The segregated solver will work through the governing equations sequentially whereas the Coupled solver solves them simultaneously. For the application of fluid flow driven by pressure under steady state conditions, the segregated solver is more appropriate as it does not employ any time-dependent equation. The solver used is the 3-Dimensional segregated solver with implicit linearization.

3.5.2.4 Defining the Physical Model for Fluid Flow in a Micro-Channel

The Laminar Model is selected as the Viscous Flow Model for the simulation, while the Eulerian model (two-phase) is selected under the Multi-phase Model taking into account the particle aspects. The Eulerian model is the most complex of multiphase models in FLUENT. It solves a set of momentum and continuity equations for each phase. Coupling is achieved through pressure and interphase exchange coefficients. The manner in which coupling is handled depends upon the type of phases involved. For granular flows (solid-liquid), the properties are obtained from the application of kinetic theory.

3.5.2.5 Creating Required Materials for Fluid Flow in a Micro-Channel

In every simulation, there is the need to create the materials needed. By default air is the material associated with the fluid. This is here changed to water-liquid. Micro particles of density 1500 Kg/m^3 are created in the database under the name "micro particles" and added to the list.

3.5.2.6 Specifying Phases: Phase 1 is assigned "water _liquid" and phase 2 is assigned "micro particles". The micro particles are considered as granules with the diameter of 1 micron. The interphase interaction is modified for drag coefficient. For solid-liquid two phase flows, the "gidaspow" scheme is used to compute drag coefficient.

3.5.2.7 Specifying Operating Conditions: For all flows, FLUENT uses gauge pressure internally. Any time an absolute pressure is needed, it is generated by adding the operating pressure to the relative pressure. Operating Pressure is set as 101,325 Pa.

3.5.2.8 Specifying Boundary Conditions for Fluid Flow in a Micro-Channel

There are six different boundary conditions of six different types for each phase and the mixture. These are "default interior" of type "interior", "fluid+particles" of type "fluid", "inlet" of type "pressure inlet", "outlet" of type "pressure outlet", "symmetry" of type "symmetry" and "walls" of type "wall". Below we describe some particular Boundary Conditions that have been applied in the study of fluid flow in a micro-channel.

1) Pressure Inlet Boundary Conditions: Pressure inlet boundary conditions are used to define the fluid pressure at flow inlets, along with all other scalar properties of the flow. They are suitable for incompressible flow calculations. A constant pressure

of 200 kPa is applied at the inlet of the micro-channel. The flow in the micro-channel will remain well below the sonic speed of 1500 m/s and, therefore compressibility effects are neglected. The direction of the flow is specified as Normal to Boundary.

2) Pressure Outlet Boundary Conditions: Pressure outlet boundary conditions require the specification of a static (gauge) pressure at the outlet boundary. Since compressibility effects are neglected, this boundary condition is very suitable. The outlet gage pressure is set to 0 Pa.
3) Wall Boundary Conditions: Wall boundary conditions are used to bound phases 1 and 2. In viscous flows, the no-slip boundary condition is enforced at walls, by default. In this study on parameters affecting flow-field and particle location, walls are considered to be stationary.

3.5.2.9. Checking the Solution Accuracy for Fluid Flow in a Micro-Channel

First Order Upwind discretization scheme is considered for momentum and volume fraction. The pressure-velocity coupling is by default the Phase-coupled SIMPLE algorithm for eulerian model. Default under-relaxation factors for all the equations of flow and volume fraction are accepted.

The solution is then initialized using inlet boundary condition. The volume fraction of phase 2 is patched with 0.02. The residual plotting is enabled. The iteration limit is set to 5000. All the solutions for all the models converged in this iteration limit.

3.5.2.10. Post-processing of Results

Since the shallow channel is of very small depth, the grid was adapted and refined using hanging node adaption scheme in the shallow channel in order to create more nodes inside the channel. The hanging node adaption scheme is shown in Figure 3.7.

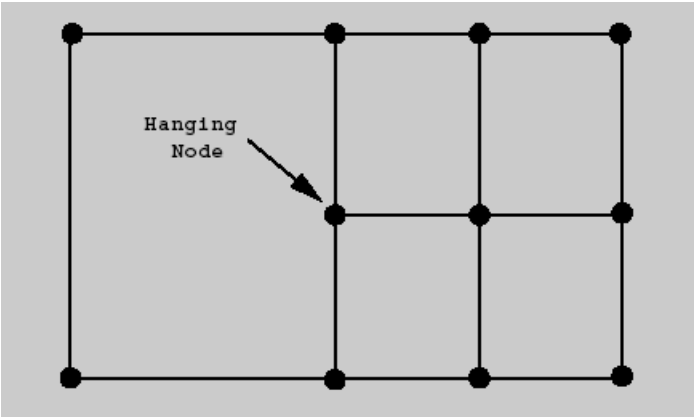

Figure 3.7: Example of hanging node refinement.

The x-y plot of static pressure vs. z-coordinate of the grid is plotted. The x-y plot of velocity magnitude vs. z-coordinate of the grid is plotted. Histograms of volume fraction variation of phase 2 in all the micro channel cases have been analyzed. Finally, the domain of 0.019 to 0.021 is set for taking the contours of volume fraction of phase 2. The grid is displayed as edges of type "feature" to show the geometry of the micro channel only. The contours are plotted on the default interior surface with contour level = 20. The term "default interior" means all the nodes in the model are taken into consideration. For 2-D plots, it is called default interior surface. The reflection of symmetry is enabled for top views. Both the top and left side views are recorded for each model. The path lines are displayed, colored by velocity magnitude of phase1, with single pulse mode. The particles are released from the nodes on the inlet face. Mass-flux is also reported for the understanding and comparison of flow resistance.

Chapter 4: CFD Simulation Results and Discussion

Exactly nineteen geometries have been considered. The simulation results are summarized in the form of pressure profiles and centerline velocity magnitudes along the length of the micro channel, contours of volume fraction variations of phase 2 (micro particles) in the micro reservoir, path lines of particles, in the micro reservoir, injected from the inlet and comparison of mass flux. Path lines directly elucidate the flow pattern inside the micro reservoirs of micro channels. The path lines are colored by phase1 velocity magnitude. Top views and left side view of the micro channel geometries are given to make it clearer.

4.1 Pressure profiles

In the 3-D scenario of fluid flow through micro channels, the velocity vector has x, y and z components. Since x and y velocity components for all the micro channel geometries are negligible, $\left(\frac{\partial p}{\partial x}\right)$ and $\left(\frac{\partial p}{\partial y}\right)$ terms in the Navier-Stokes equations are insignificant. The pressure is only function of z. Thus, variation in the depth of the channels and variation in the cross section area of the reservoir does not affect the pressure profile. The pressure remains more or less constant in the first channel at 200 kPa and gradually decreases from the micro reservoir position to zero (gauge pressure) at the outlet. Pressure profile of case A2 is shown in Figure 4.1. All micro channel geometries follow same pressure profile. Shifting the position of the micro reservoir shift the point from which the pressure starts decreasing in the micro channel geometry.

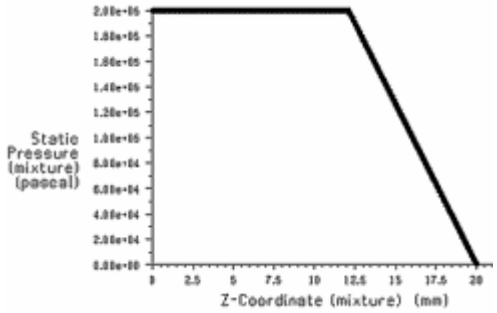

Figure 4.1 Pressure profile plot for case A2. Slope is -25.32 Pa/micron (kPa/mm).

4.2 Centerline Velocity Magnitude plots

The centerline velocity magnitude plots are generated from the velocity magnitudes at the nodes along the length of the micro channel. The surface chosen is default interior (section 3.5.2.10). Top nodes on the plots along the length of the channel signify centerline velocity magnitudes in the channel parts where the flow profile is parabolic. Because of the front wall in the micro reservoir, the fluid particle accelerates (change in velocity magnitude or direction) towards the inlet of the shallow channel. This can be explained on the concept of drag in which an object obstructing the streamlines realizes drag force along the streamlines. Since the front wall is stationary, the fluid particles in the streamlines are accelerated. However if the front wall of the micro reservoir has larger width (which can be made by increasing the cross section area of the micro reservoir) compared to the width of the first channel, the energy gained by the fluid particles due to the wall is used in the recirculation of the fluid in the micro reservoir itself. The cases such as A12, A13 and A16 in which the width of the first channel and the micro reservoir is same, there is no recirculation. High centerline velocity supports high mixing of fluid(s) in the micro reservoir.

4.2.1 Variation in position of the micro reservoir from the inlet.(A1, A2, A3 and A4)

The position of the micro reservoir has a considerable effect on the velocities in both the first channel and the shallow channel. An increase in centerline velocity in the shallow channel can be seen by moving the position of the micro reservoir (Figure 4.2 to Figure 4.5) as most of the pressure drop occurs in the shallow channel, which becomes shorter. The nearer it is to the outlet, the higher is the centerline velocity magnitude in the channel parts. Acceleration due to change in velocity magnitude can be seen in the micro reservoirs of case A1, A2 and A3 due to the front wall in the micro reservoir. The reason is the streamline motion of the fluid is affected by the front wall. However in case A4, the centerline velocity magnitude in the micro reservoir and the shallow channel is same. Fluid acceleration occurs but only to the extent of the velocity magnitude in the shallow channel.

4.2.2 Variation in first channel and micro reservoir depth (100 micron, 250 micron and 400 micron) keeping the shallow channel depth = 5 micron (A1, A5 and A6)

As can be seen from the three plots shown below (Figure 4.2, Figure 4.6 and Figure 4.7), the centerline velocity magnitude decreases steadily in the first channel with the increase in the depth of first channel and micro reservoir. Because of the greater height of the front wall in the 400 micron depth micro channel, acceleration effect can be felt by the fluid particles in the 400 micron depth channel much before the micro reservoir entrance. However, in the 100 micro depth micro channel, the

acceleration effect makes the velocity magnitude to double the velocity magnitude in the micro reservoir. In the 250 micro depth micro channel, the acceleration effect raises the velocity to the extent of velocity magnitude in the shallow channel. This shows that increasing the depth of the first channel displaces the point from which the acceleration effect can be realized in the first channel although it reduces the maximum centerline velocity that can be attained in the micro reservoir. In the shallow channel the velocity is almost the same in all the three cases. The plots also suggest, in the first channel, the velocity magnitude remains more or less constant in the A1 case, little fluctuates in the A5 case but rises gradually from the middle of the first channel to the reservoir in the A6 case.

4.2.3 Variation in first channel and micro reservoir depth (100 micron, 250 micron and 400 micron) keeping the shallow channel depth = 3 micron (A7, A8 and A9)

As shown in Figure 4.8, Figure 4.9 and Figure 4.10, the centerline velocity magnitude remains constant i.e. 0.05 m/s for the shallow channel in the three cases. However, it is comparatively lower than the 5 micron shallow channel depth micro channel cases where the velocity magnitude is 0.14 m/s. Acceleration effect can be seen in the micro reservoir but only to the extent of the velocity magnitude in the shallow channel. Thus, reducing the depth of the shallow channel from 5 micron to 3 micron destroys the acceleration effect in the micro reservoir which is undesirable for mixing. In the first channel, the centerline velocity magnitude is higher in the 250 micron depth channel than in the 100 micron and 400 micron depth channel (least). The plots also suggest that the centerline velocity magnitude remains more or less constant along the first channel and the micro reservoir entrance in all the three cases.

4.2.4 Variation in cross-sectional area of the micro reservoir with first channel width = shallow channel width = 100 micron (A10, A11 and A12)

As can be seen from the plots (Figure 4.11, Figure 4.12 and Figure 4.13), the centerline velocity magnitudes in the shallow channel region are the same for all the three cases. However, in the first channel the centerline velocity magnitude is much lower in A10 and high in A11 and A12. Acceleration effect before the entrance of the micro reservoir can be seen on the streamlines in case A11 and A12. However, there is no appreciable acceleration effect in case A10 because energy gained by the fluid particles is used in the re-circulation in the micro reservoir itself. In case A12, the width of the micro reservoir and the first channel is same. This does not allow any recirculation in the micro reservoir.

4.2.5 Variation in cross-sectional area of the micro reservoir with first channel width = shallow channel width = 150 micron (A13, A14 and A15)

As can be seen from the plots (Figure 4.14, Figure 4.15 and Figure 4.16), the centerline velocity magnitudes in the first channel and shallow channel remain more or less constant for different cross-sectional-area micro reservoirs. However, acceleration effect due to the front wall can be seen in the micro reservoir of case A14 and A15. Acceleration effect can be seen in case A14 before the micro reservoir entrance. In case A15, the centerline velocity magnitude decreases at the micro reservoir entrance.

4.2.6 Variation in cross-sectional area of the micro reservoir with first channel width = shallow channel width = 70 micron (A16, A17, A18 and A19)

As can be seen from the plots (Figure 4.17, Figure 4.18, Figure 4.19 and Figure 4.20), the centerline velocity in the shallow channel remains more or less constant irrespective of the change in the cross-section of the micro reservoir. However, the centerline velocity magnitude in the first channel increases with the increase in cross-sectional area of the micro-reservoir. However, acceleration effect before the entrance of the micro reservoir due to the front wall gradually becomes predominant as we go from case A16 to A18. Case A19 does not show this acceleration as the energy is absorbed in the recirculation in the micro reservoir itself.

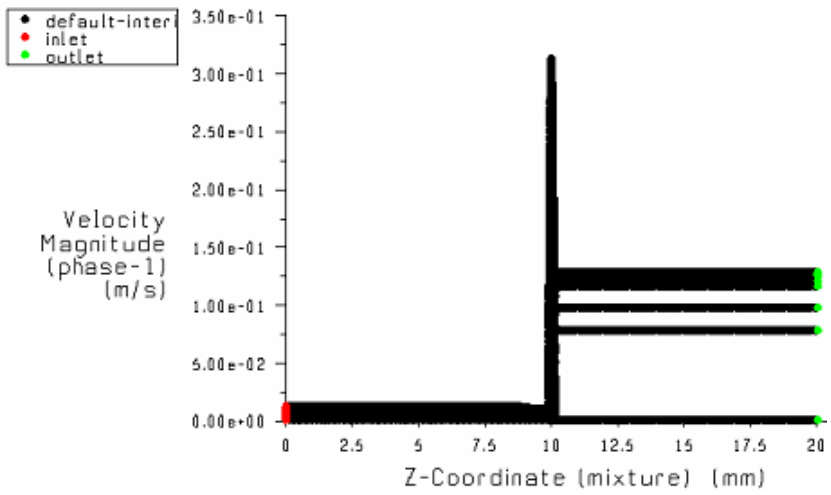

Figure 4.2: Centerline velocity magnitude plot of micro channel A1 along its length

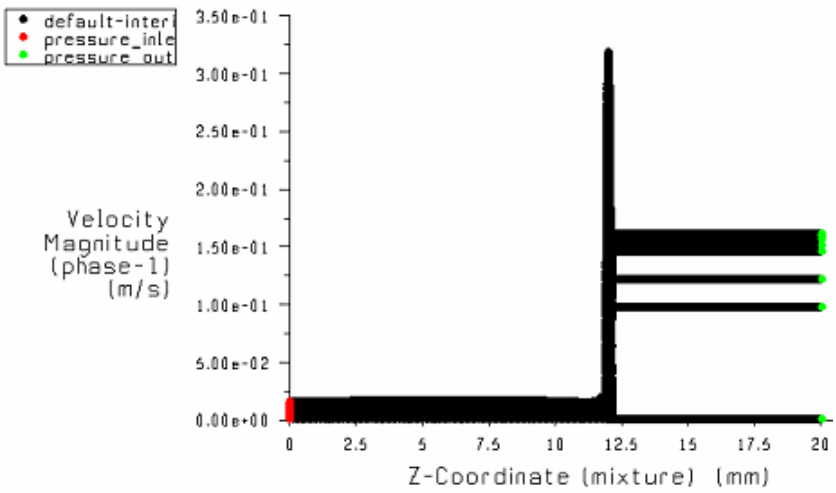

Figure 4.3: Centerline velocity magnitude plot of micro channel A2 along its length

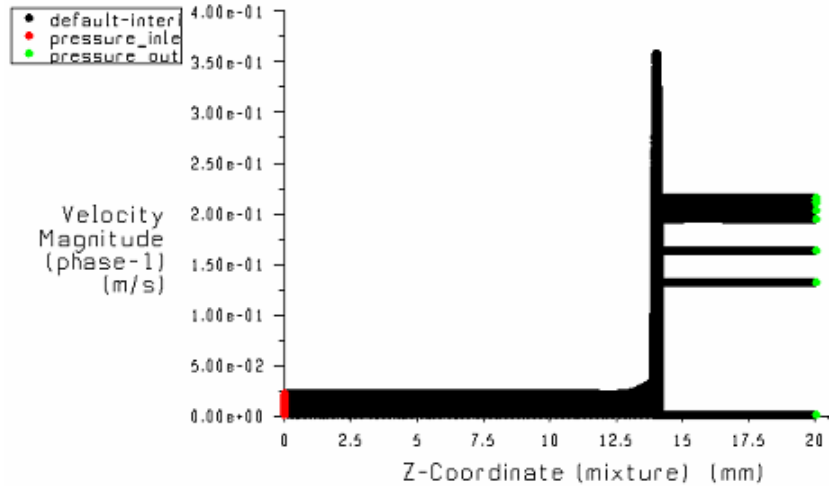

Figure 4.4: Centerline velocity magnitude plot of micro channel A3 along its length

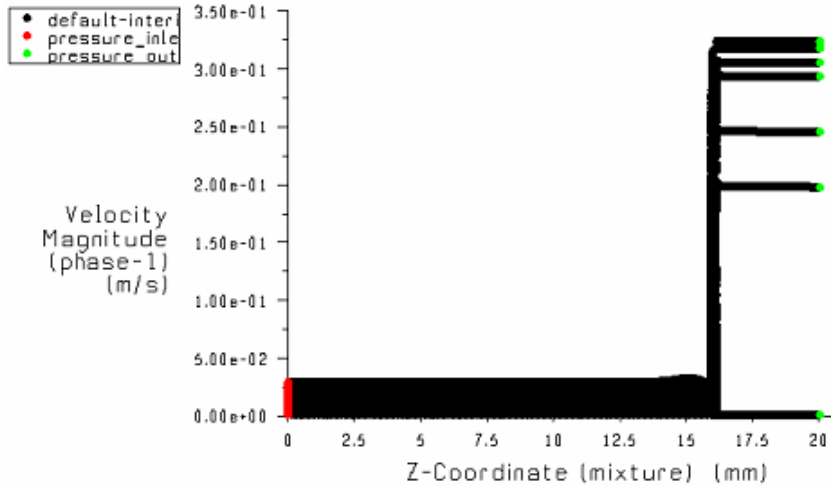

Figure 4.5: Centerline velocity magnitude plot of micro channel A4 along its length

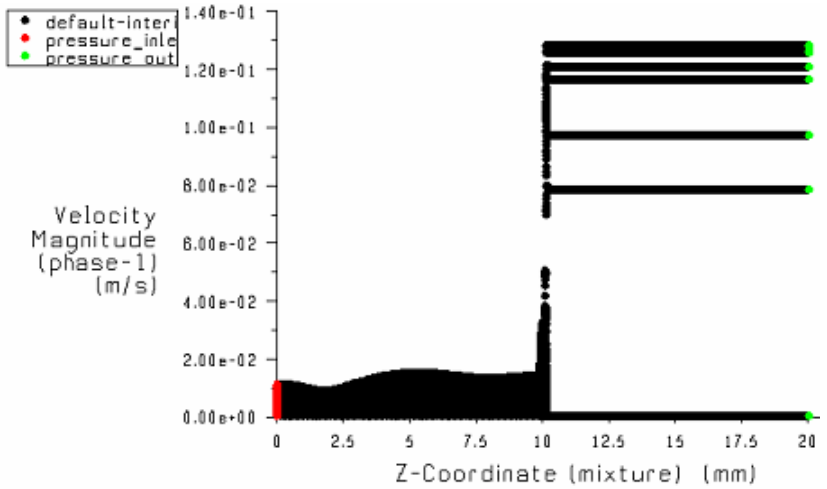

Figure 4.6: Centerline velocity magnitude plot of micro channel A5 along its length

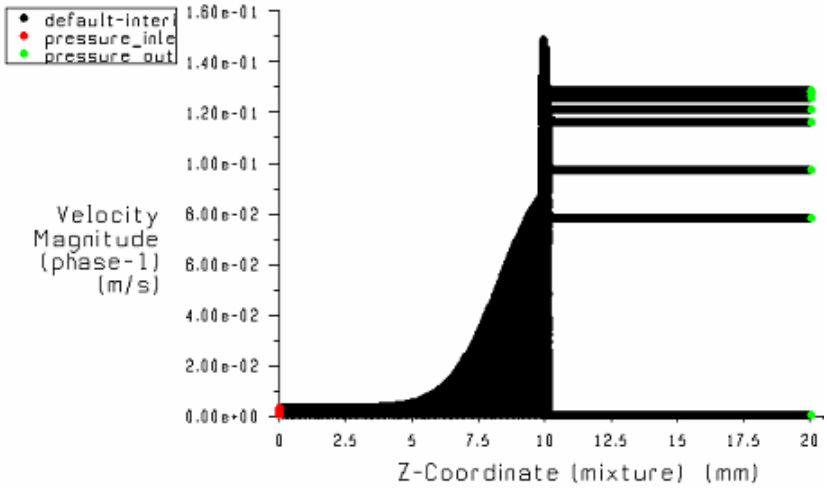

Figure 4.7: Centerline velocity magnitude plot of micro channel A6 along its length

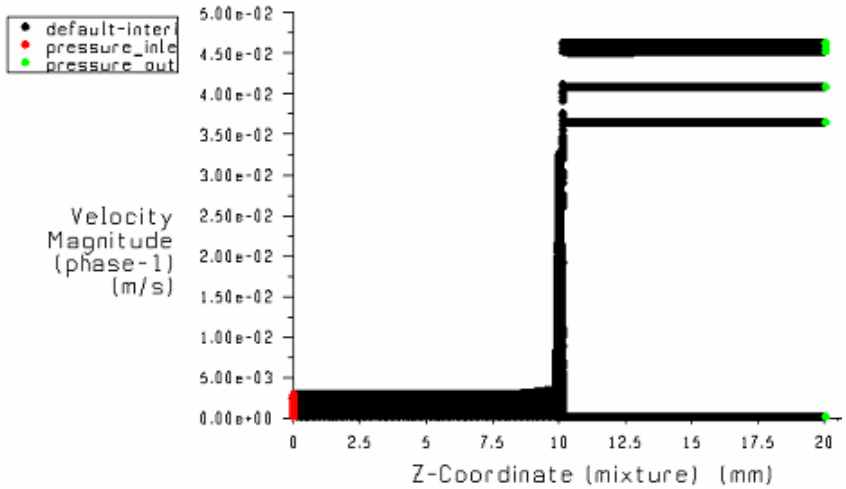

Figure 4.8: Centerline velocity magnitude plot of micro channel A7 along its length

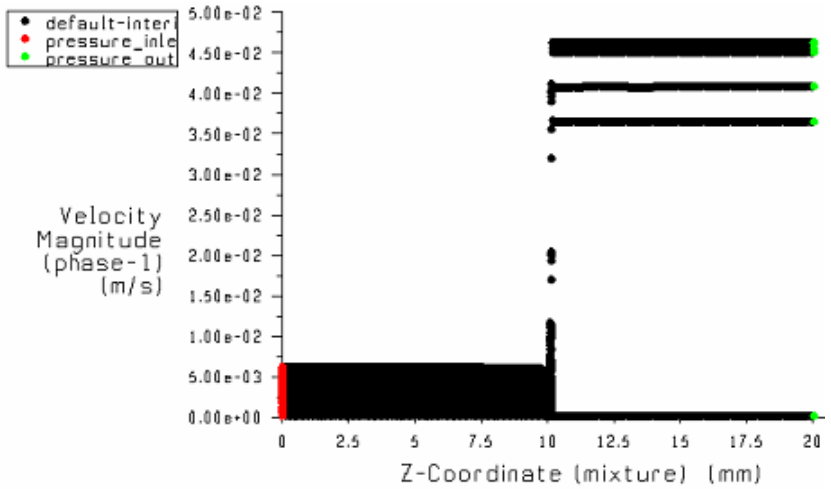

Figure 4.9: Centerline velocity magnitude plot of micro channel A8 along its length

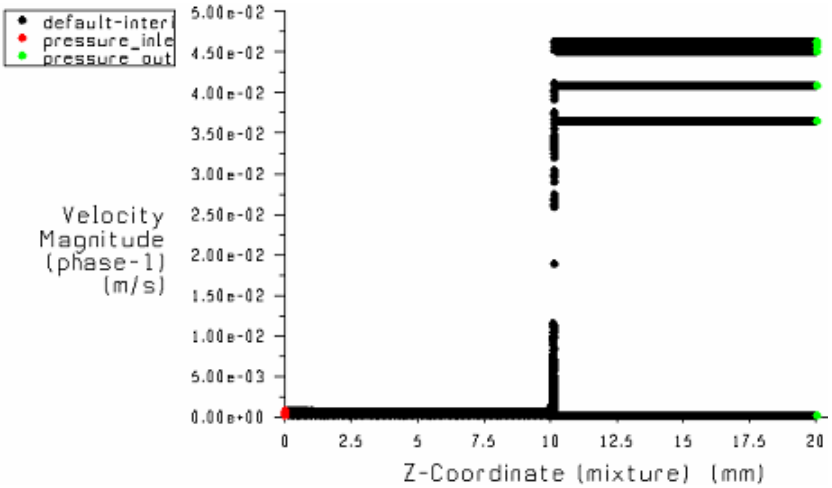

Figure 4.10: Centerline velocity magnitude plot of micro channel A9 along its length

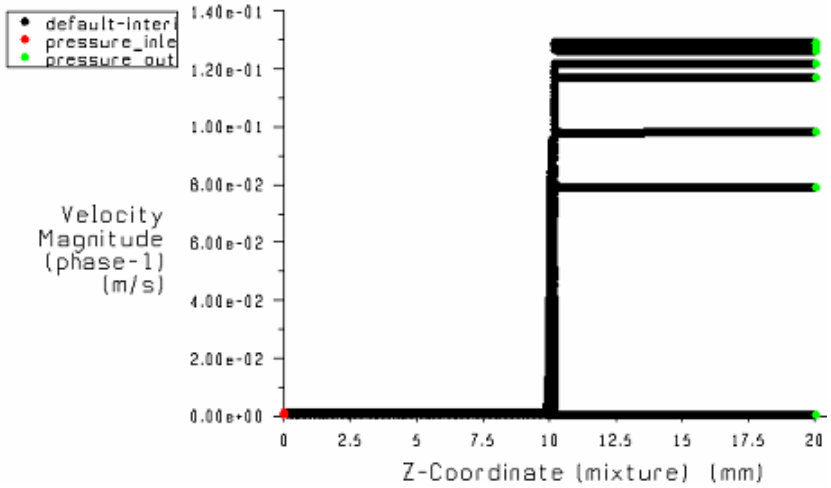

Figure 4.11: Centerline velocity magnitude plot of micro channel A10 along its length

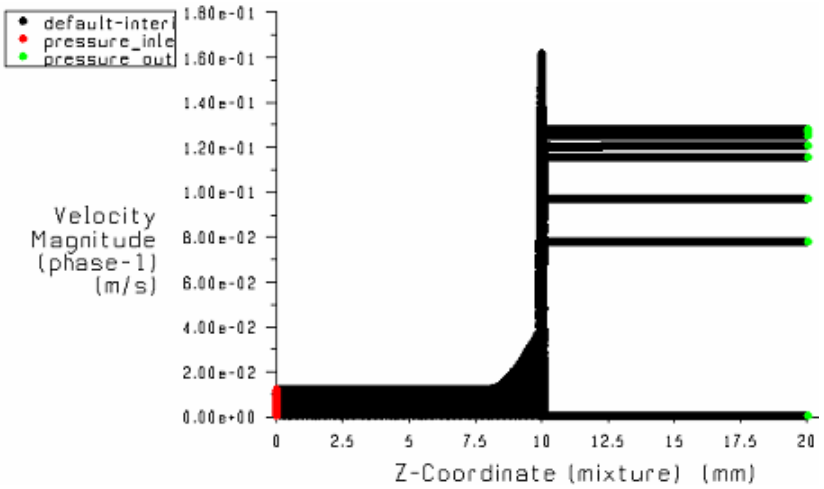

Figure 4.12: Centerline velocity magnitude plot of micro channel A11 along its length

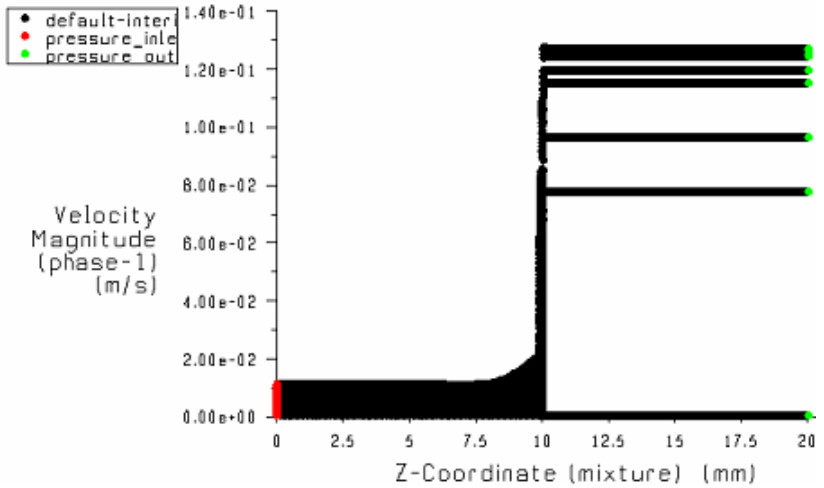

Figure 4.13: Centerline velocity magnitude plot of micro channel A12 along its length

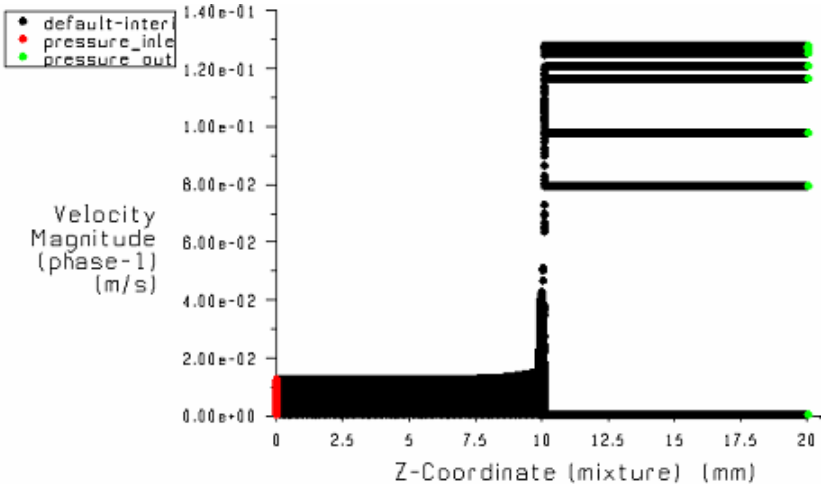

Figure 4.14: Centerline velocity magnitude plot of micro channel A13 along its length

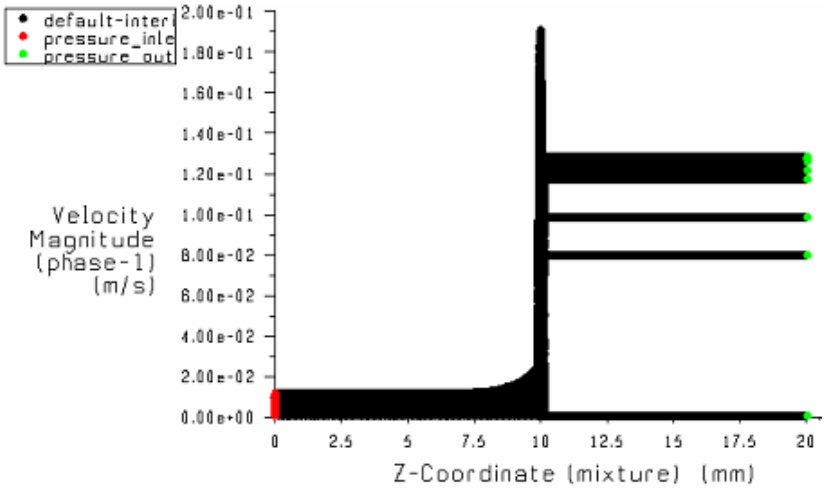

Figure 4.15: Centerline velocity magnitude plot of micro channel A14 along its length

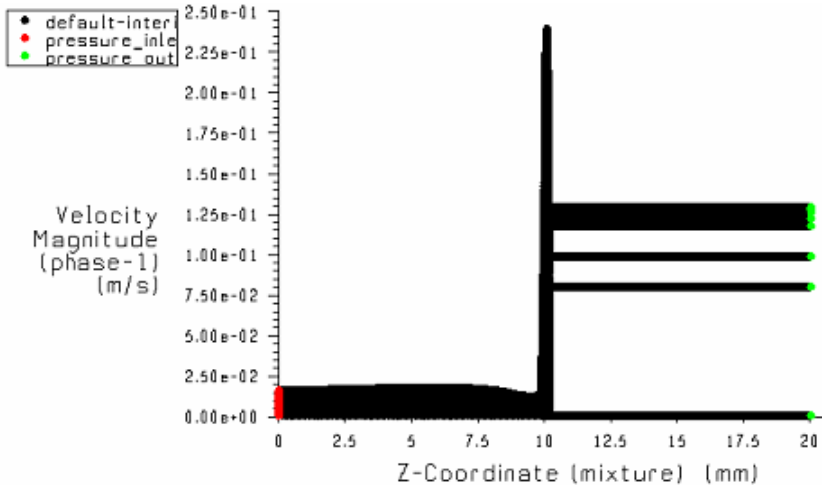

Figure 4.16: Centerline velocity magnitude plot of micro channel A15 along its length

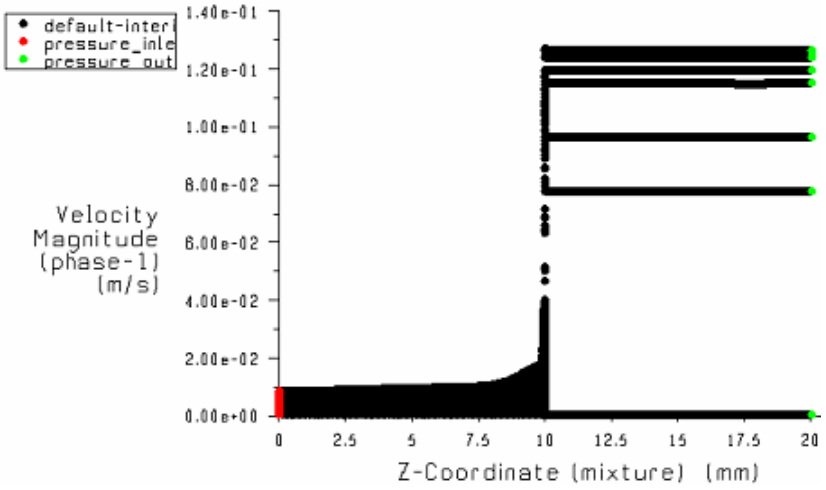

Figure 4.17: Centerline velocity magnitude plot of micro channel A16 along its length

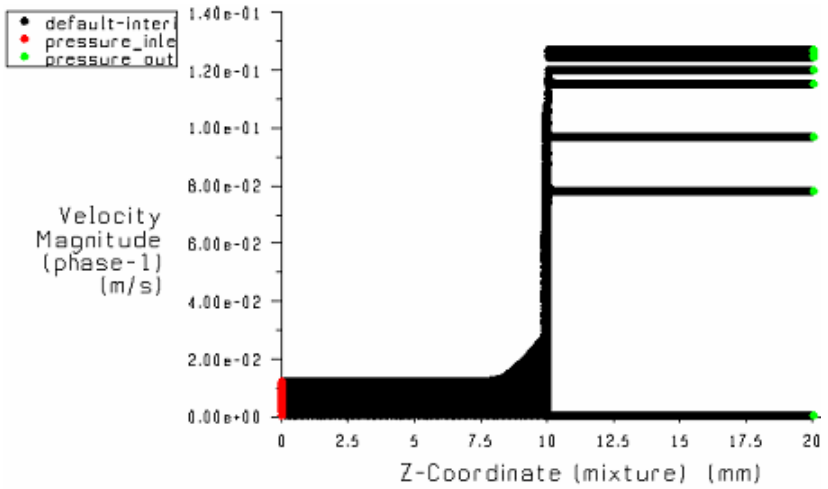

Figure 4.28: Centerline velocity magnitude plot of micro channel A17 along its length

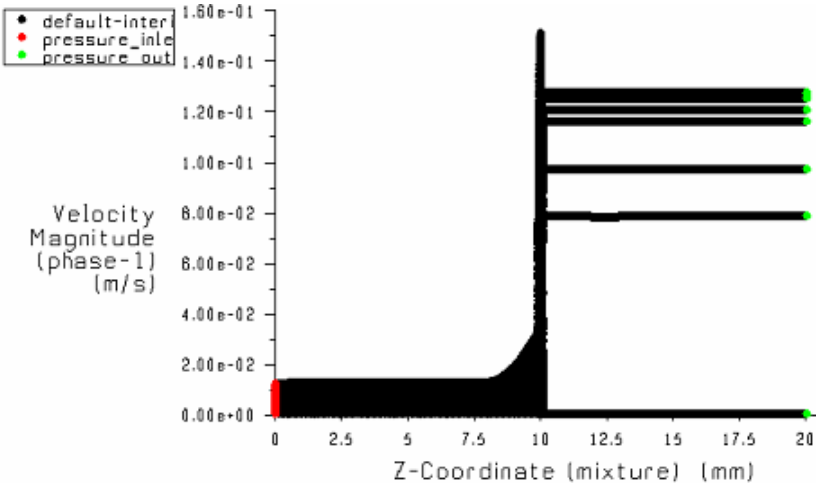

Figure 4.19: Centerline velocity magnitude plot of micro channel A18 along its length

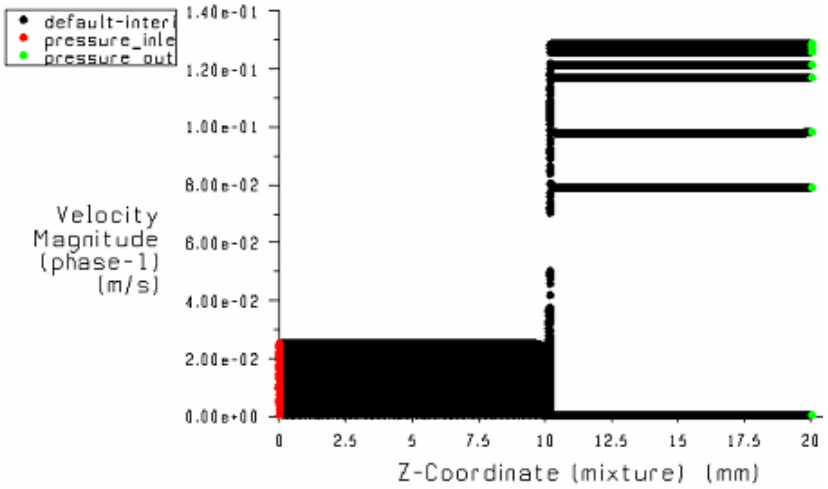

Figure 4.20: Centerline velocity magnitude plot of micro channel A19 along its length

4.3 Contours of Volume fraction of phase 2 (micro particles)

In all the micro channel geometries the flow field is initialized with the volume fraction of micro particles at 0.02 under identical boundary conditions. The volume fraction after the convergence of solution varies at different locations in the micro channel based on its geometry and dimensions. This variation in volume fraction helps to assess the location of particle accumulation in the micro reservoir. The volume fractions are contoured in the domain of 0.019 to 0.021. The histograms of volume fractions of phase 2 corresponding to all the cases shows that most of the cells in the grid lie in this range. The region of 0.021 shows the rise in the volume fraction of phase 2 (micro particles). Top views (with reflection from symmetry) and left side views for each case are presented here. The contour levels are shown with Figure 4.21. The red and blue regions indicate accumulation and depletion, respectively. Green region shows no change in volume fraction. The yellow and bluish green regions show the increase and decrease in volume fraction, respectively. In few cases black region also appears. If it is near red region it shows the volume fraction of more than 0.021 but less than 0.023. If it is near blue region it shows depletion more than 0.019. Normally in μ-TAS and LOC application, the detection of particle is done from the top. Particular micro channel geometry can be best suited for detection if the accumulation region is near the top wall in the micro reservoir. However, accumulation in the first channel, at the junction of shallow channel and the micro reservoir or in the shallow channel itself is highly undesirable as it can result in clogging of the micro channel.

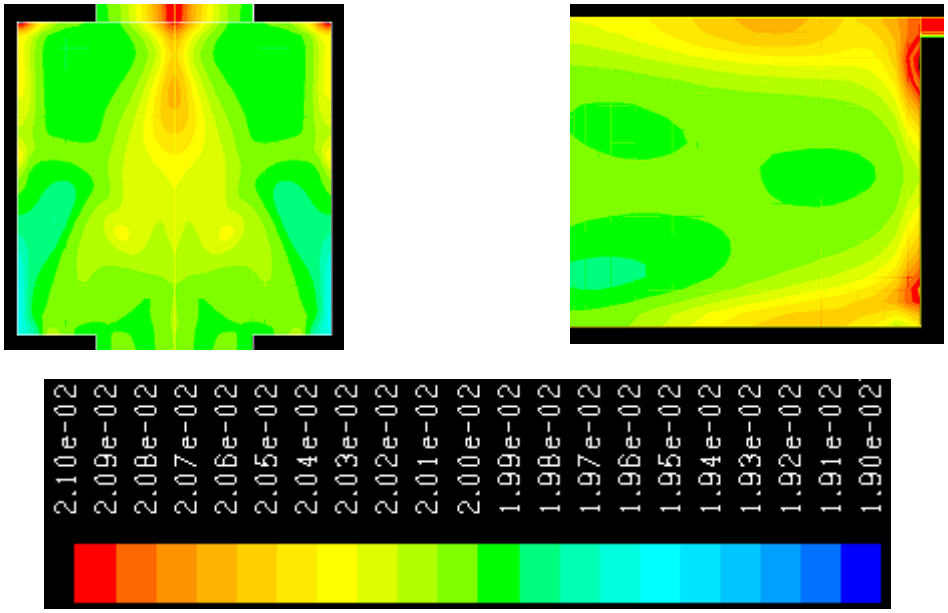

Figure 4.21: Filled contours of volume fraction of phase 2 in case A1

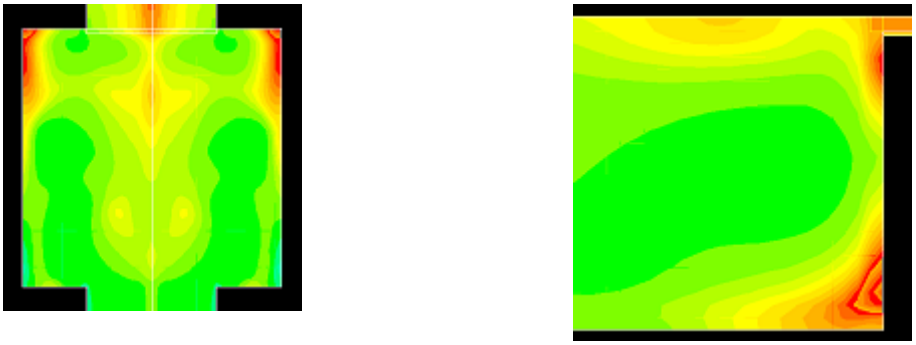

Figure 4.22: Filled contours of volume fraction of phase 2 in case A2

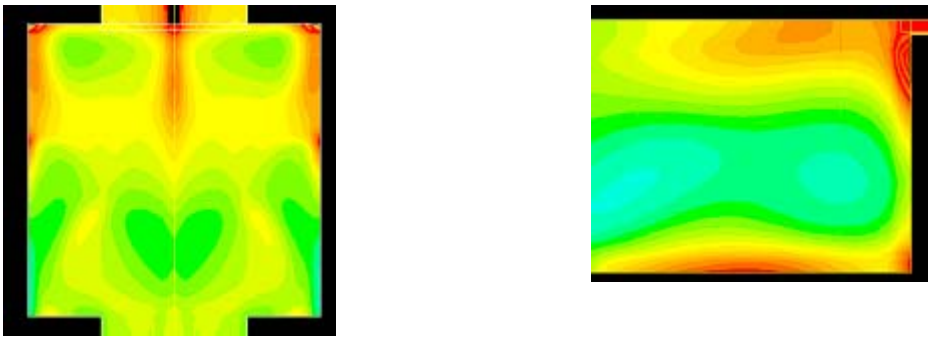

Figure 4.23: Filled contours of volume fraction of phase 2 in case A3

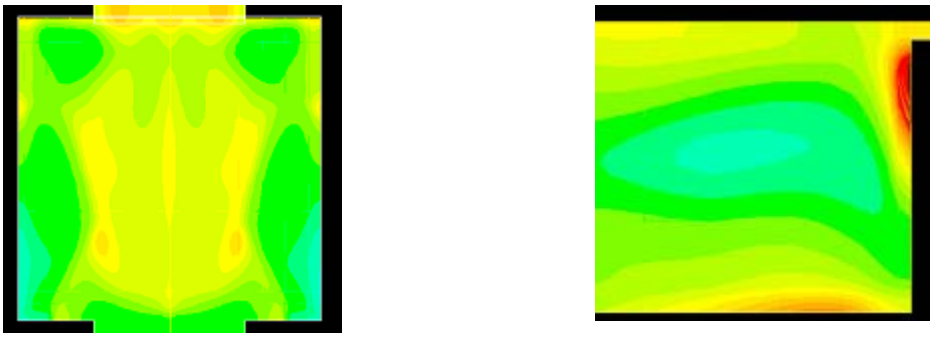

Figure 4.24: Filled contours of volume fraction of phase 2 in case A4

4.3.1 Variation in the position of the micro reservoir from the inlet (A1, A2, A3 and A4)

From the contours (Figure 4.21, Figure 4.22, Figure 4.23 and Figure 4.24) we can see that in all the four cases the region of rise in volume fraction mainly lies in the area of the micro reservoir wall just below the top wall of the micro reservoir. Particle accumulation can be seen in the region just below the entrance of the shallow channel and at the base of the front wall of the micro reservoir. Cases A3 and A4 also show the accumulation at the bottom wall of the micro reservoir. Case A3 also shows the black region in the shallow channel where the volume fraction is greater than 0.21. The central region of the micro reservoirs in all the cases shows a decrease in volume fraction. The shallow channels show the accumulation of micro particles. Between the junction of top wall and sidewalls, accumulation can be seen in the front part of the micro reservoir while depletion at the back. Other regions in the micro reservoir show more or less the unchanged volume fraction. In conclusion, Case A4 is less likely to get clogged in the shallow channel part compared to others. Also, cases A1 and A3 are more suitable for detection purpose from the top.

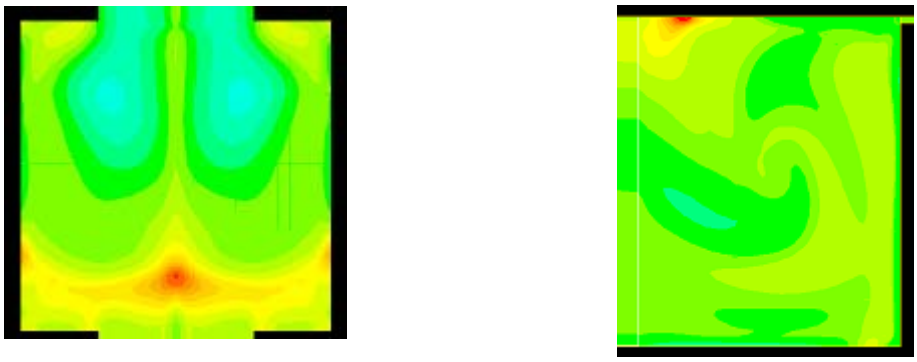

Figure 4.25: Filled line contour of volume fraction of phase 2 in case A5

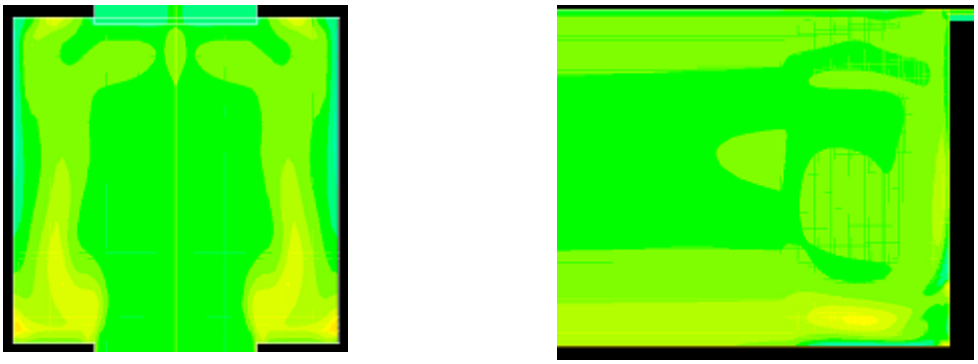

Figure 4.26: Filled line contour of volume fraction of phase 2 in case A6

4.3.2 Variation in first channel and micro reservoir depths keeping the shallow channel depth = 5 micron. (A1, A5 and A6)

As shown in Figure 4.21, Figure 4.25 and Figure 4.26, the volume fraction is high in the front of the micro reservoir in case A1 and at the back of the reservoir in case A5. There is not much rise in volume fraction in A6 except at the back of the top wall of the micro reservoir. Also, accumulation is near the front part of the micro reservoir in case A1 while at the back in case A5. Accumulation is hardly seen in case A6. A5 also shows a decrease in volume fraction near the entrance of the shallow channel. There is some rise in volume fraction at the base of the reservoir in A6 but A1 shows good accumulation at the base. Comparing the three cases, we can say A5 is best in both respects of no clogging in the shallow channel and better detection in the micro

reservoir. A6 is not suitable for detection while A1 is likely to get clogged in the shallow channel part.

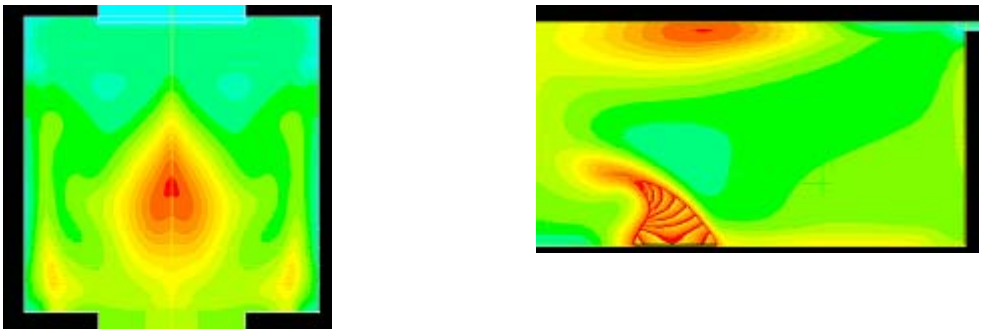

Figure 4.27: Filled line contour of volume fraction of phase 2 in case A7

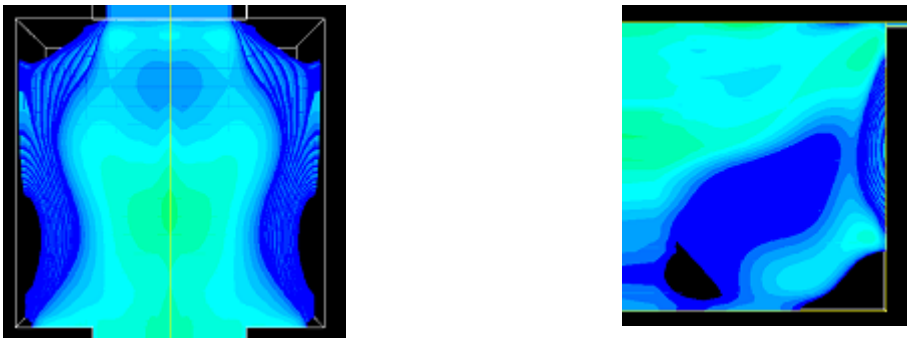

Figure 4.28: Filled line contour of volume fraction of phase 2 in case A8

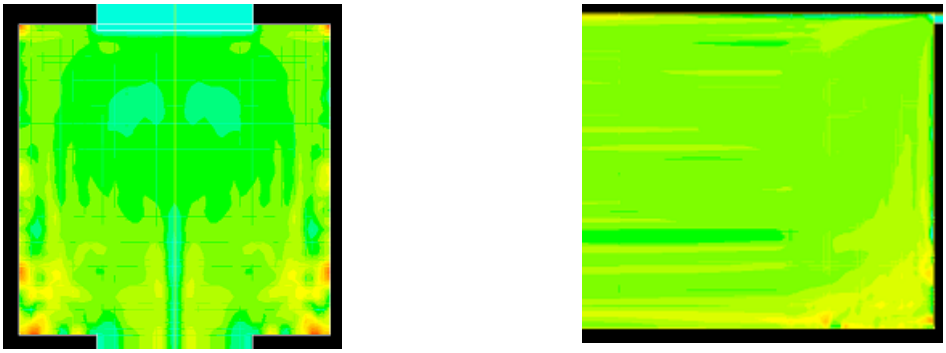

Figure 4.29: Filled line contour of volume fraction of phase 2 in case A9

4.3.3 Variation in first channel and micro reservoir depths keeping the shallow channel depth = 3 micron. (A7, A8 and A9)

As shown in the figures (Figure 4.27, Figure 4.28 and Figure 4.29), the volume fraction in these three geometries are very different from each other. Case A7 shows the accumulation in the micro reservoir while case A8 shows depletion in the micro reservoir. Case A9 neither shows significant accumulation nor depletion. In case A7, accumulation region lies below the top wall and just above the bottom wall of the micro reservoir. There is no rise in volume fraction near the entrance of the shallow channel also. Case A8 shows depletion at the corners of the micro reservoir. The reason is the accumulation in the first channel itself (not shown in figure). Case A9 shows some accumulation dots at the back side of the reservoir from the top. However in the entire micro reservoir region the volume fraction does not vary much. Case A7 is most suitable for better detection from the top and for not supporting clogging at the shallow channel entrance. The accumulation is also confined to a smaller region.

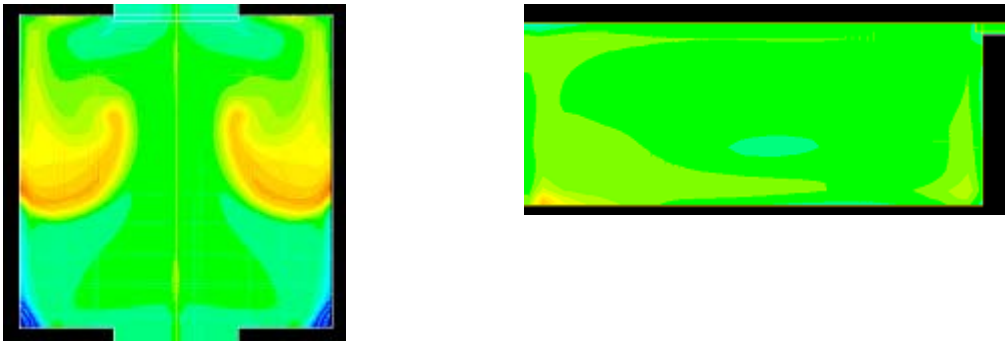

Figure 4.30: Filled line contour of volume fraction of phase 2 in case A10

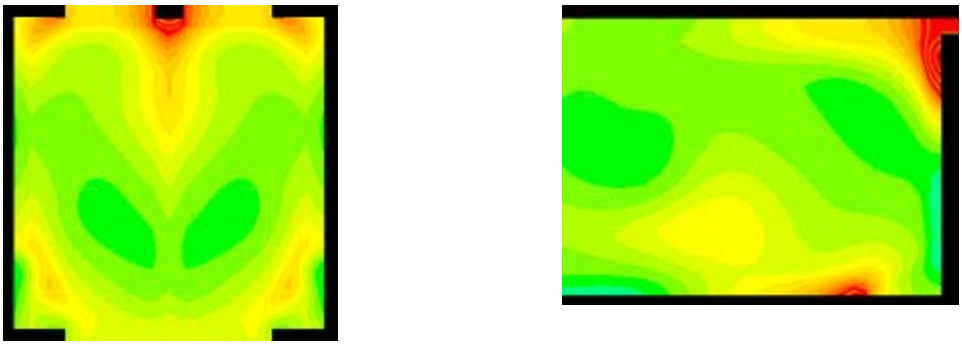

Figure 4.31: Filled line contour of volume fraction of phase 2 in case A11

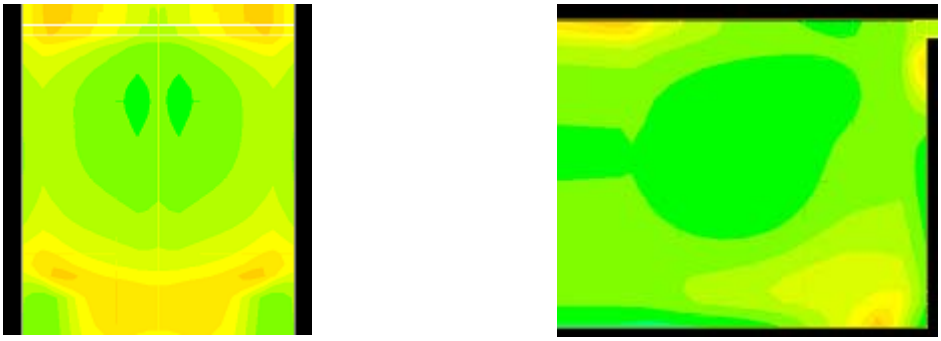

Figure 4.32: Filled line contour of volume fraction of phase 2 in case A12

4.3.4 Variation in the cross-section of the micro reservoir with first channel width = shallow channel width = 100 micron. (A10, A11 and A12)

As shown in the figures (Figure 4.30, Figure 4.31 and Figure 4.32), case A11 shows accumulation in the shallow channel region and the region near its entrance while case A10 is free from it. In all the three cases, the volume fraction increases near the top wall of the micro reservoir. Cases A11 and A12 also show accumulation at the bottom wall of the reservoir. Case A10 shows depletion in the back side of the reservoir. Case 12 also shows high volume fraction in the shallow channel region. Case 10 is best amongst the three for high detection and low susceptibility for clogging.

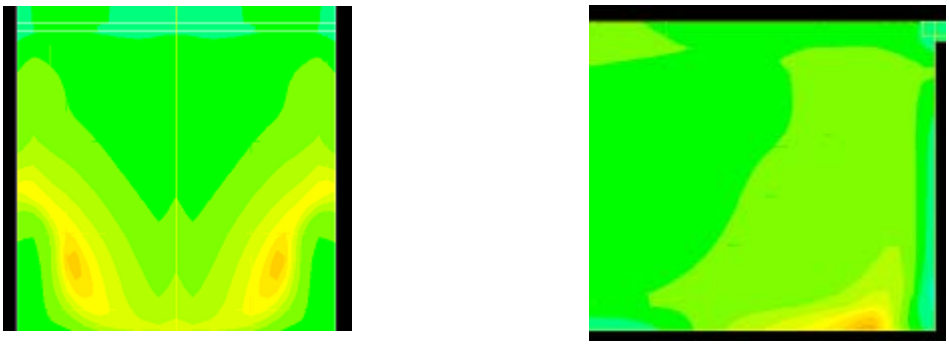

Figure 4.33: Filled line contour of volume fraction of phase 2 in case A13

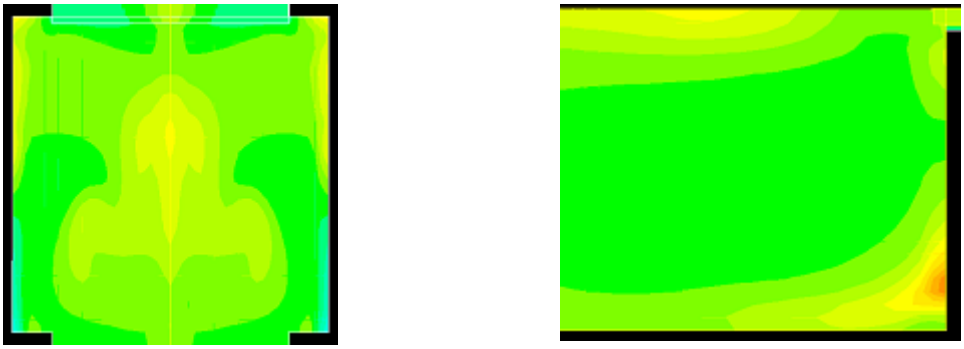

Figure 4.34: Filled line contour of volume fraction of phase 2 in case A14

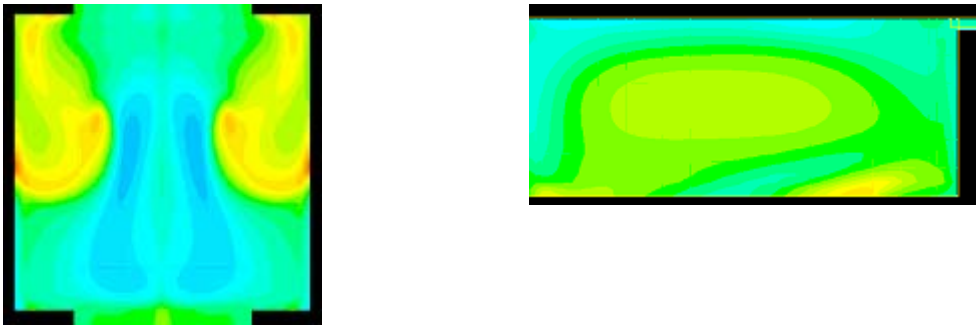

Figure 4.35: Filled line contour of volume fraction of phase 2 in case A15

4.3.5 Variation in the cross-section of the micro reservoir with first channel width = shallow channel width = 150 micron. (A13, A14 and A15)

As shown in Figure 4.33, Figure 4.34 and Figure 4.35, depletion exists near the top wall of the micro reservoir in case A15. Accumulation and rise in volume fraction can be seen at the back of top wall of the micro reservoir in case A13, near the sidewalls in case A15 and at the base of the front wall in case A14. Rise in volume

fraction can also be seen at the central region of the top wall in A14 and at the bottom wall of reservoir in case A15.

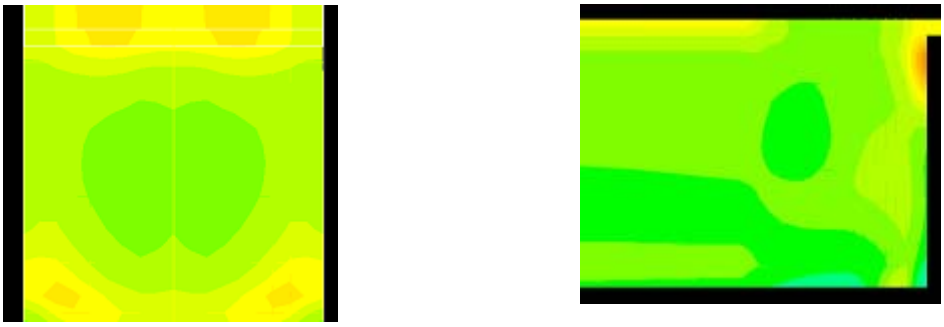

Figure 4.36: Filled line contour of volume fraction of phase 2 in case A16

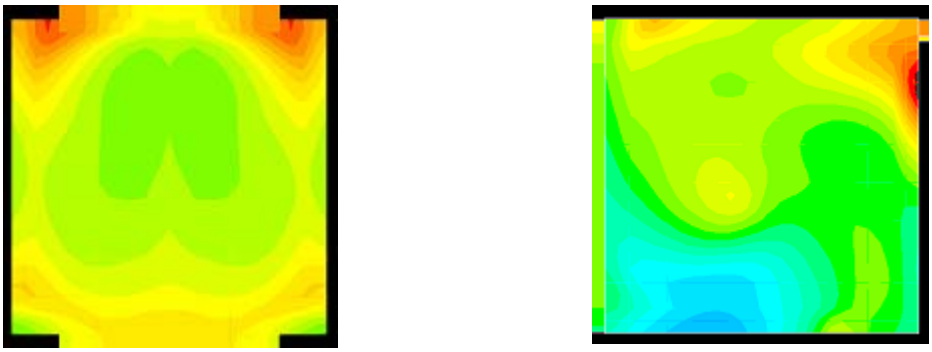

Figure 4.37: Filled line contour of volume fraction of phase 2 in case A17

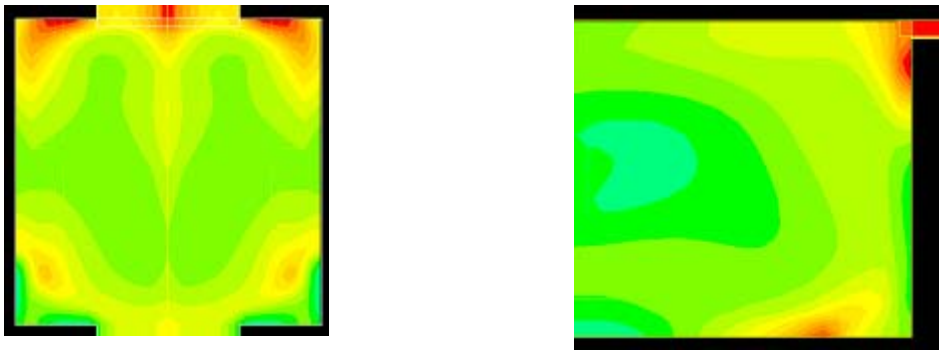

Figure 4.38: Filled line contour of volume fraction of phase 2 in case A18

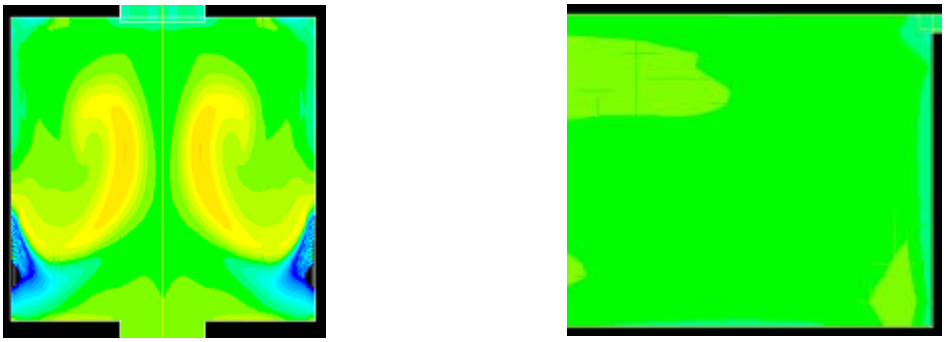

Figure 4.39: Filled line contour of volume fraction of phase 2 in case A19

4.3.6 Variation in the cross-section of the micro reservoir with first channel width = shallow channel width = 70 micron. (A16, A17, A18 and A19)

As shown in Figure 4.36, Figure 4.37, Figure 4.38 and Figure 4.39, Cases A17 and A18 show accumulation in the shallow channel region while cases A16, A17 and A18 show accumulation just below the entrance of the shallow channel. Case A19 shows high volume fraction in the central region of the top wall of the micro reservoir while case A16, A17 and A18 show high volume fraction in the backside of the top wall of the micro reservoir. Case A19 also shows depletion at the backside of the top wall of the micro reservoir.

4.4 Path lines of the particles injected from the inlet surface of the micro channel

Path lines show the general pattern of flow inside the micro reservoir. The path lines are colored by velocity magnitude of phase1 in m/s. Top views with symmetrical reflection and left side views are presented here.

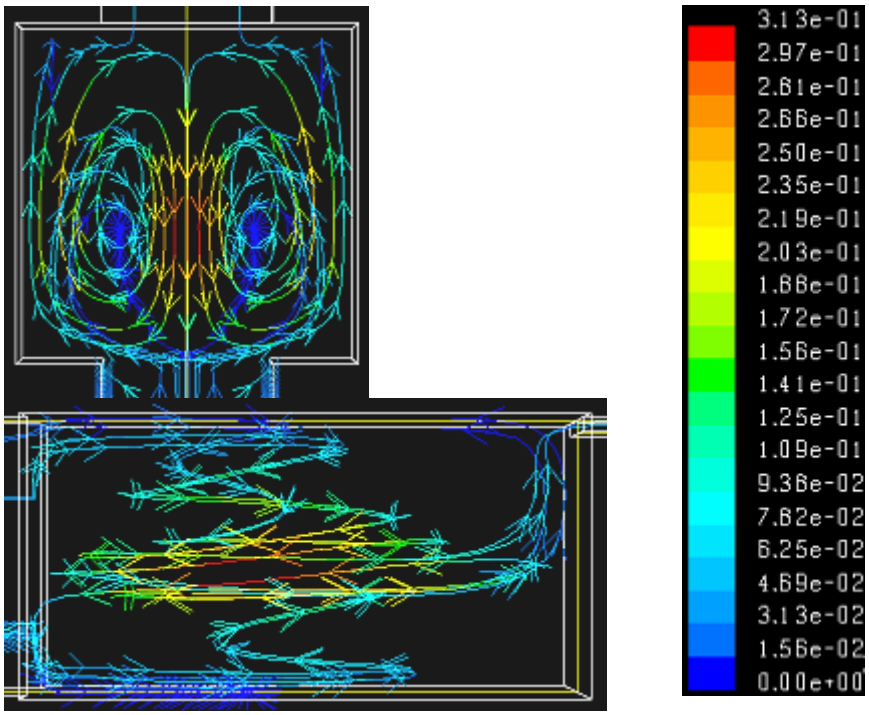

Figure 4.40: Path lines followed by particles in the micro reservoir injected from the inlet surface in case A1.

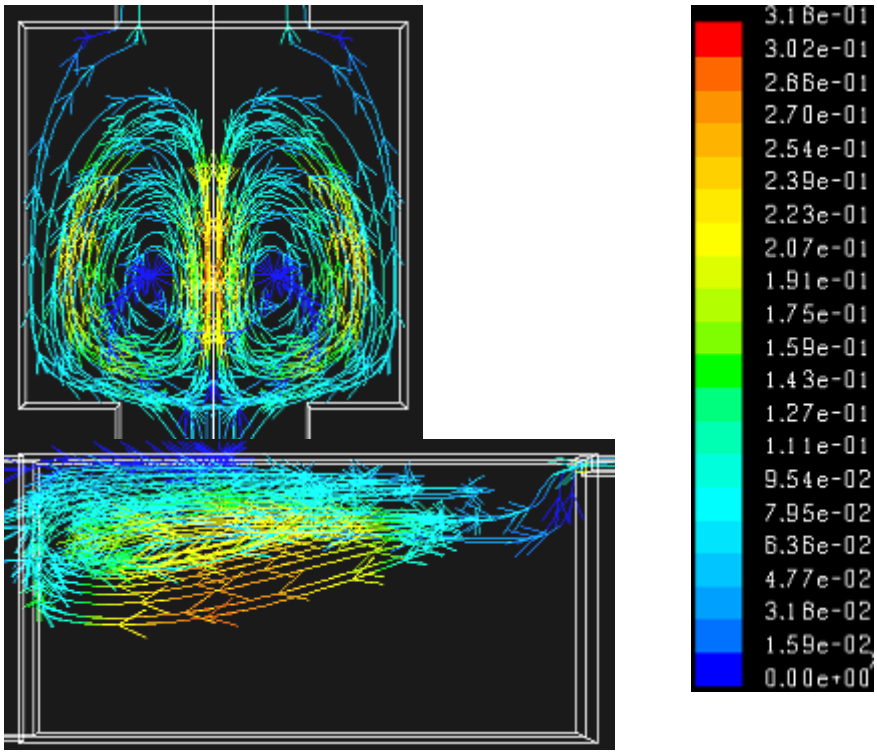

Figure 4.41: Path lines followed by particles in the micro reservoir injected from the inlet surface in case A2.

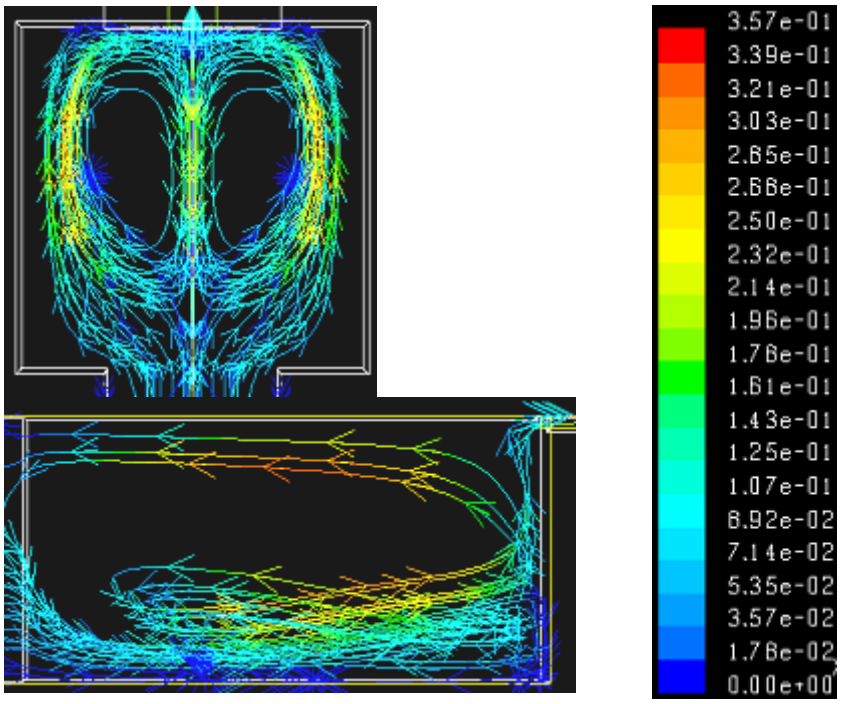

Figure 4.42: Path lines followed by particles in the micro reservoir injected from the inlet surface in case A3.

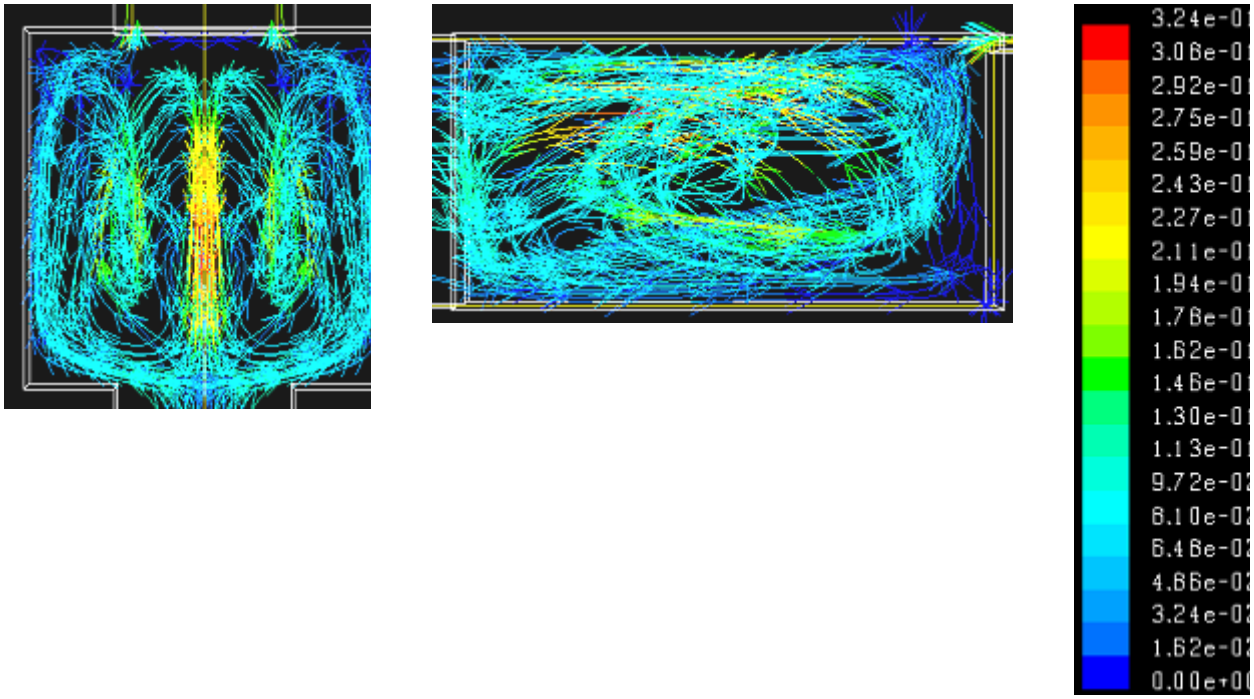

Figure 4.43: Path lines followed by particles in the micro reservoir injected from the inlet surface in case A4.

4.4.1 Variation of the position of the micro reservoir from the inlet. (A1, A2, A3 and A4)

As can be seen from the figures (Figure 4.40, Figure 4.41, Figure 4.42 and Figure 4.43), that varying the position of the micro reservoir markedly changes the path lines of the particles. In most of the cases, reverse velocity vectors on the symmetry can be seen. Case A1 shows two vortices from the top. The particles follow the helical path inside the micro reservoir before entering into the shallow channel. Case A2 also shows two vortices from the top. However, the particles converge towards the top wall before entering into the micro reservoir and follow the helical path in top half of the micro reservoir. Case A3 shows the convergence of particles before entering into the micro reservoir towards its bottom wall and rise up in the helical path towards the top wall of the micro reservoir. The particle motion is confined to the periphery of the two vortices rather at the center. For case A4, the vortices are not so clear. The particle motion is in the whole region of the reservoir with recirculation in not so circular way.

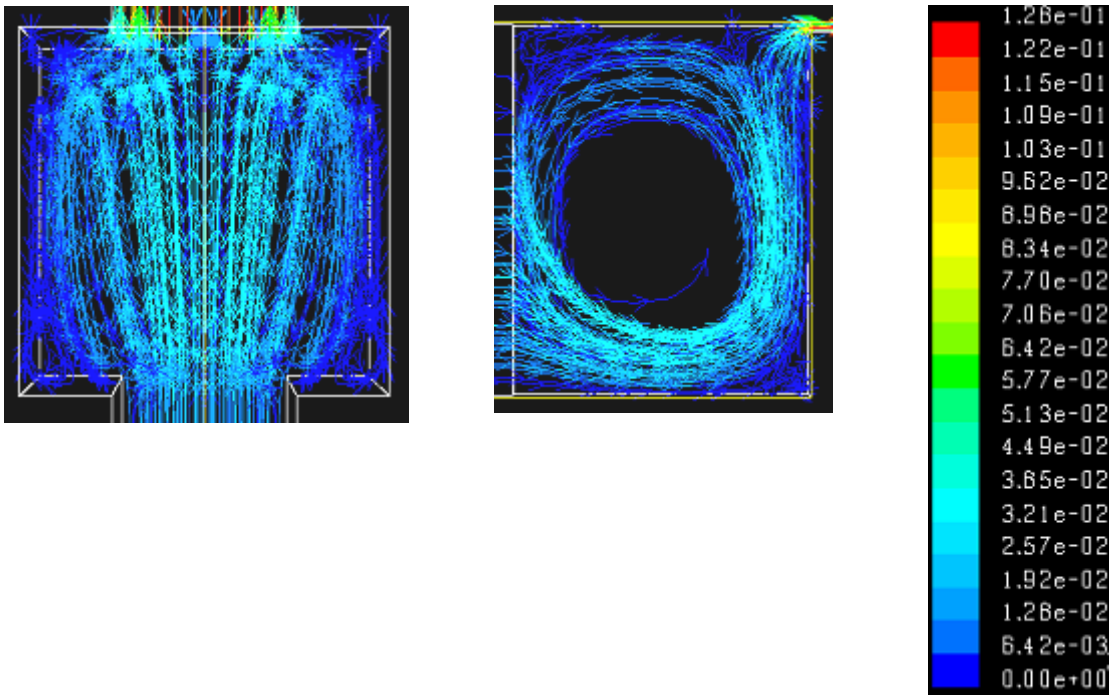

Figure 4.44: Path lines followed by particles in the micro reservoir injected from the inlet surface in case A5.

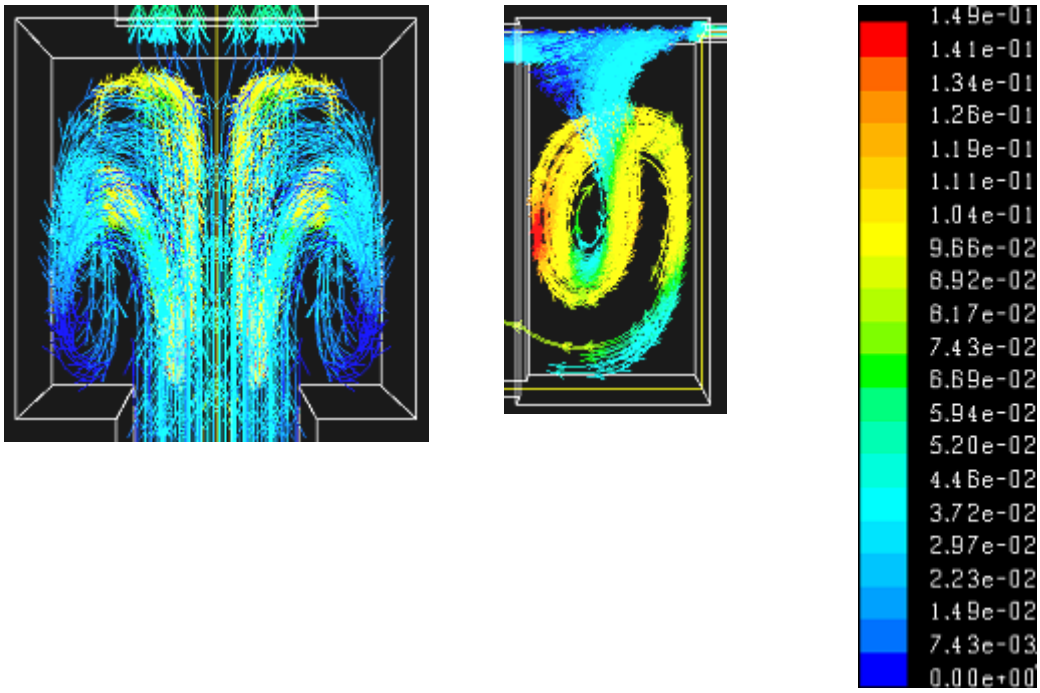

Figure 4.45: Path lines followed by particles in the micro reservoir injected from the inlet surface in case A6.

4.4.2 Variation in first channel and micro reservoir depths keeping the shallow channel depth = 5 micron. (A1, A5 and A6)

Figure 4.40, Figure 4.44 and Figure 4.45 show the path lines corresponding to cases A1, A5 and A6 respectively. Case A1 gives the horizontal vortices in the symmetrical halves of the micro reservoir while case A5 gives vertical vortices in the reservoir. Case A6 does not give clear vortices but circular motion of the particles can be seen in the left side views towards the bottom wall of the micro reservoir. Particle motion in case A1 follows a helical path in the two vortices from top wall and bottom wall. Particle motion converges to the bottom of the micro reservoir in case A5 and rise towards the top wall. A fraction of the particles enter the shallow channel and the rest of them follow circular motion inside the micro reservoir. In case A6, the particles converge to the top wall of the micro reservoir and move towards the shallow channel entrance in straight forward way. However, the particles show settling toward the bottom wall of the micro reservoir in circular motion.

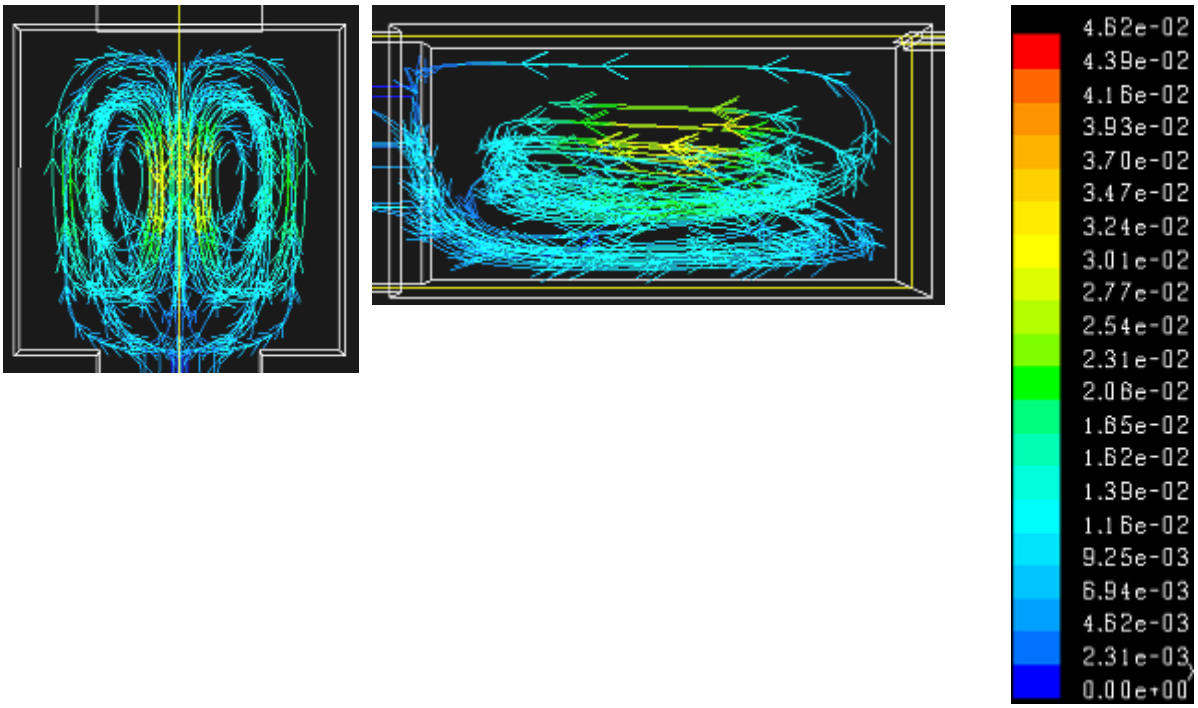

Figure 4.46: Path lines followed by particles in the micro reservoir injected from the inlet surface in case A7.

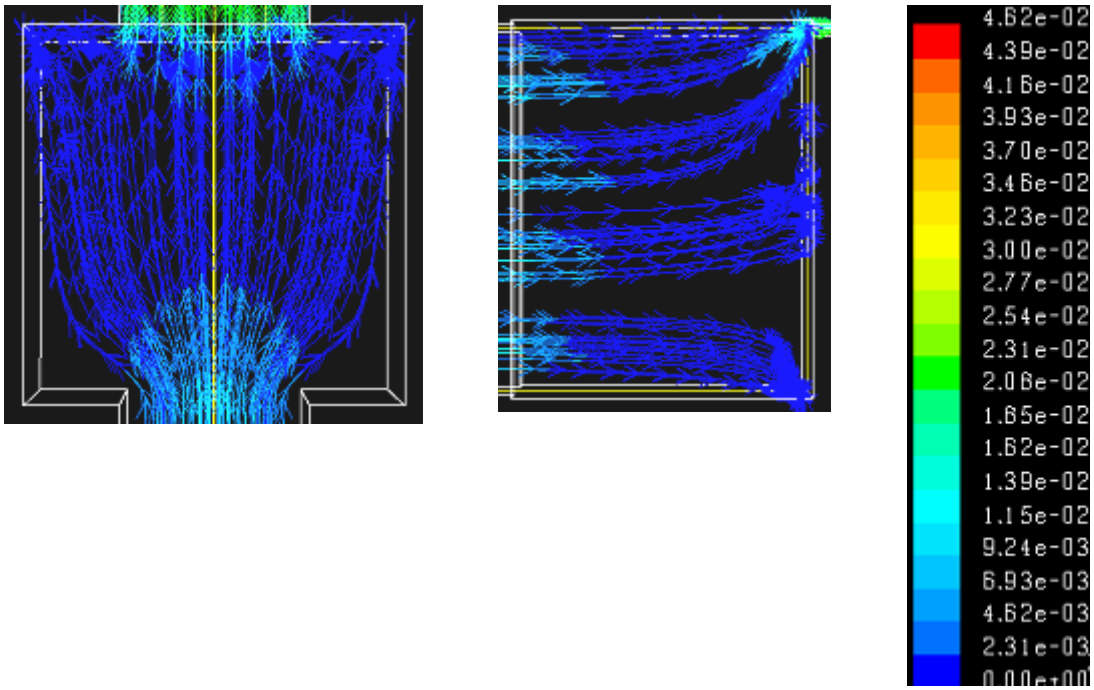

Figure 4.47: Path lines followed by particles in the micro reservoir injected from the inlet surface in case A8.

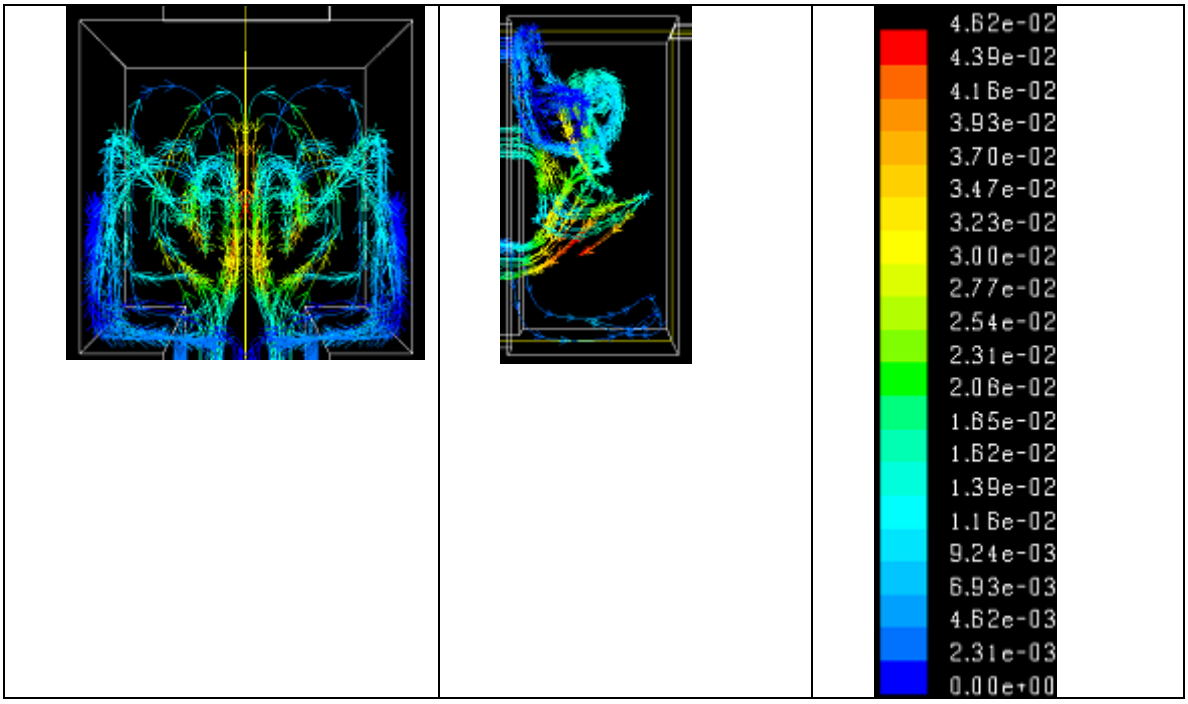

Figure 4.48: Path lines followed by particles in the micro reservoir injected from the inlet surface in case A9.

4.4.3 Variation in first channel depth and micro reservoir depth keeping the shallow channel depth = 3 micron. (A7, A8 and A9)

As shown in the figures (Figure 4.46, Figure 4.47 and Figure 4.48), the case A7 follows the scenario of two vortices in the symmetrical half of the micro reservoir, case A8 has straight path lines in the micro reservoir, and case A9 results in indistinguishable path lines. Particles in case A7 converge towards the bottom of the micro reservoir at its entrance and move toward the top wall in the helical path However, in case A8, there is no vortex and the path lines are quite straight.

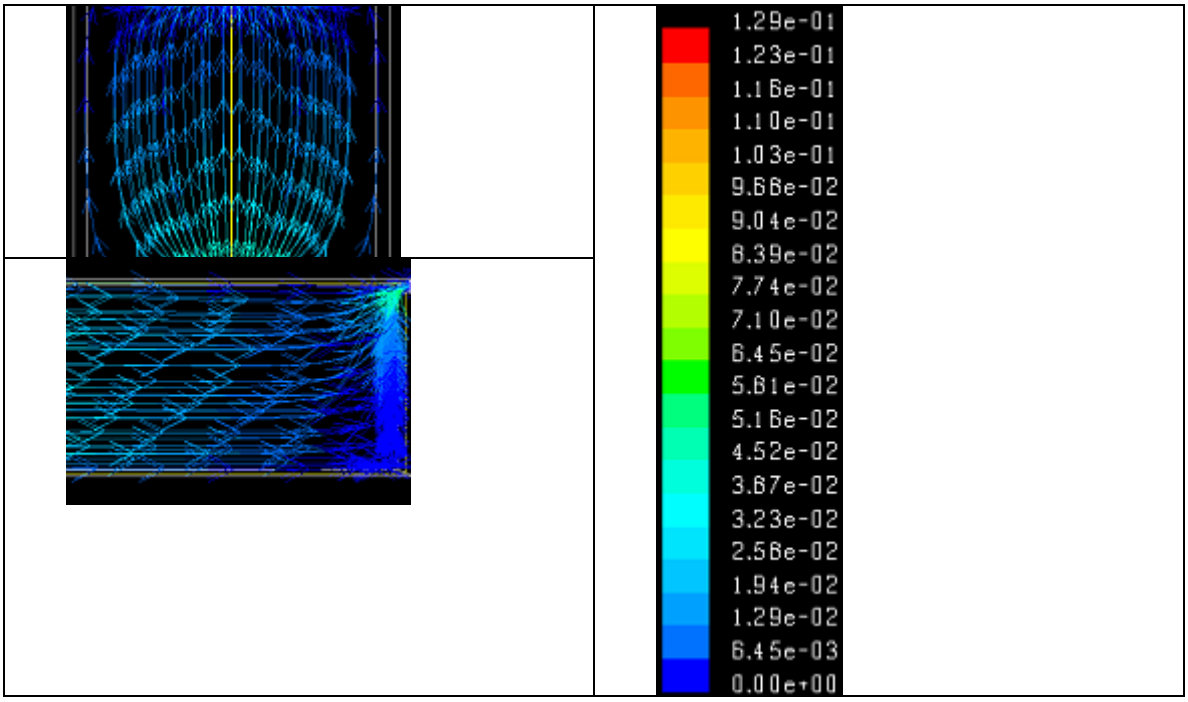

Figure 4.49: Path lines followed by particles in the micro reservoir injected from the inlet surface in case A10

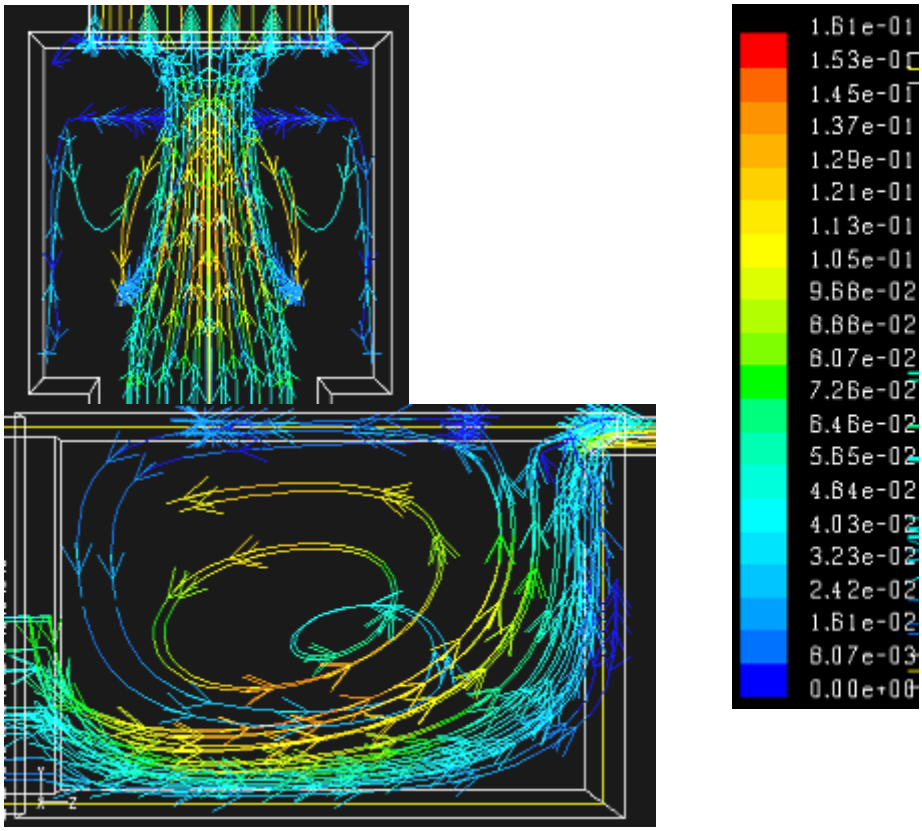

Figure 4.50: Path lines followed by particles in the micro reservoir injected from the inlet surface in case A11.

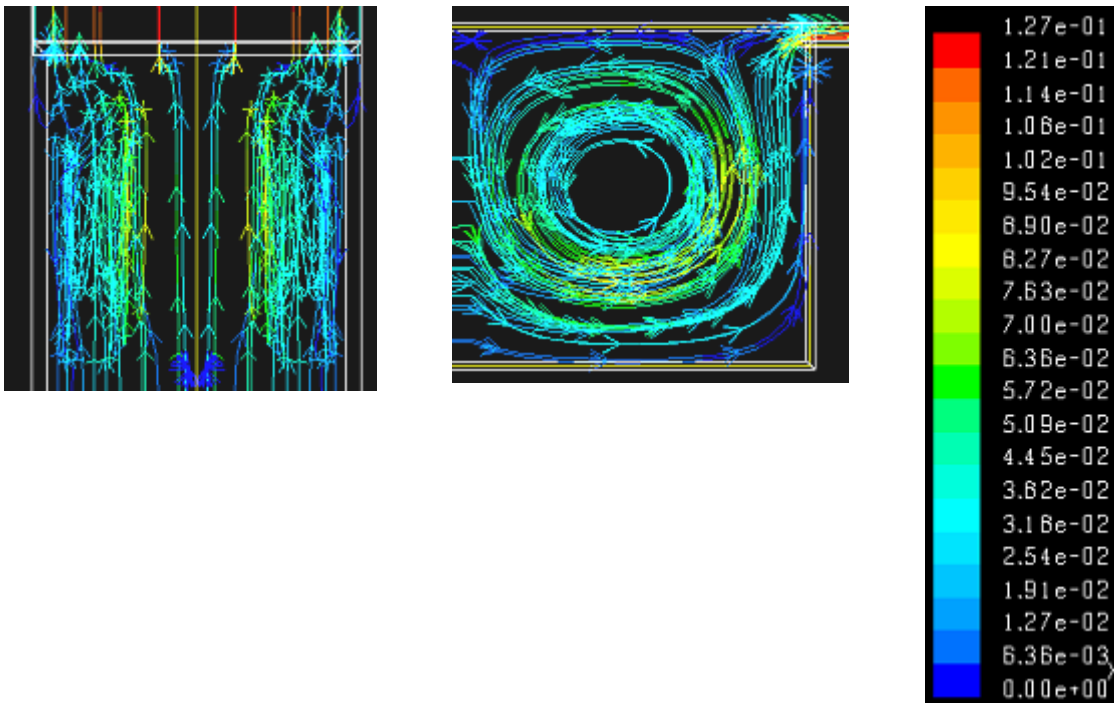

Figure 4.51: Path lines followed by particles in the micro reservoir injected from the inlet surface in case A12.

4.4.4 Variation in cross-section of the micro reservoir with first channel width = shallow channel width = 100 micron (A10, A11 and A12)

As shown in the figures (Figure 4.49, Figure 4.50 and Figure 4.51), all the three cases show straight path lines from the top. In case A10, path lines are quite straight. In case A11, the particles converge towards the bottom central region in the micro reservoir and follow vertical motion towards the shallow channel entrance. A fraction of the particles recirculate back in the micro reservoir. Case A12 also shows the same scenario but the particle motion is more in the vertical recirculation and the path lines are distributed uniformly in the entire micro reservoir region.

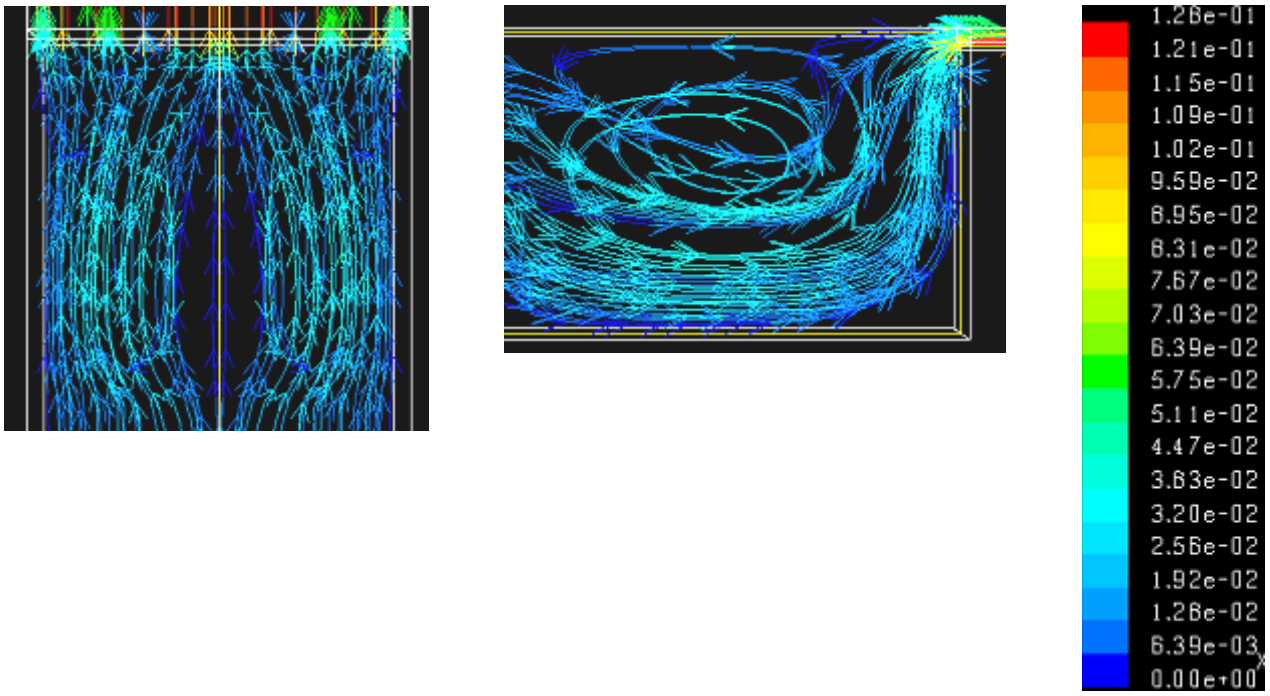

Figure 4.52: Path lines followed by particles in the micro reservoir injected from the inlet surface in case A13.

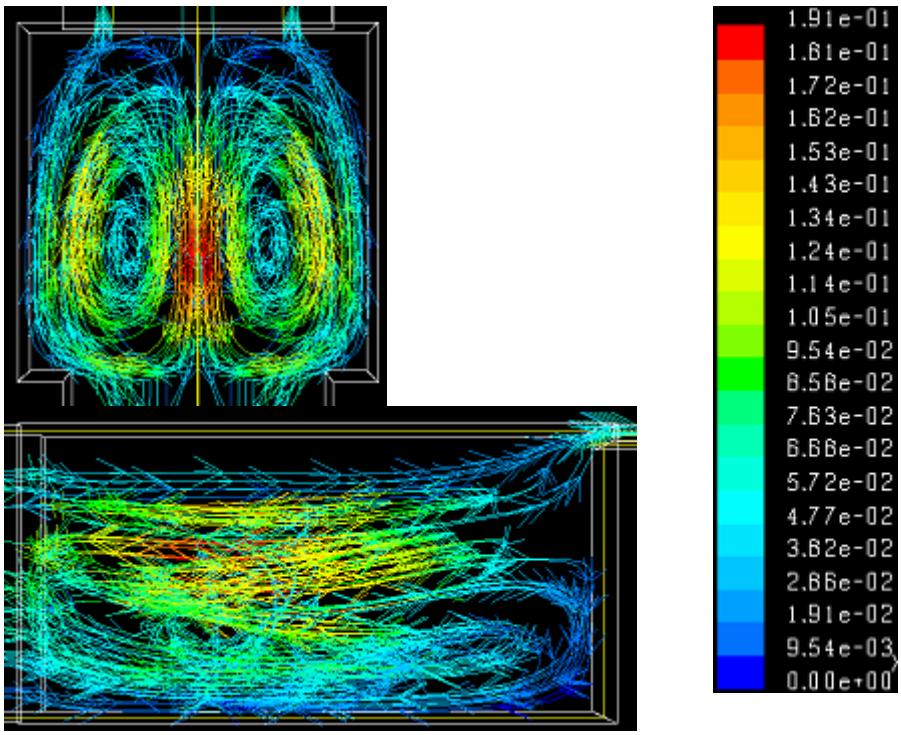

Figure 4.53: Path lines followed by particles in the micro reservoir injected from the inlet surface in case A14.

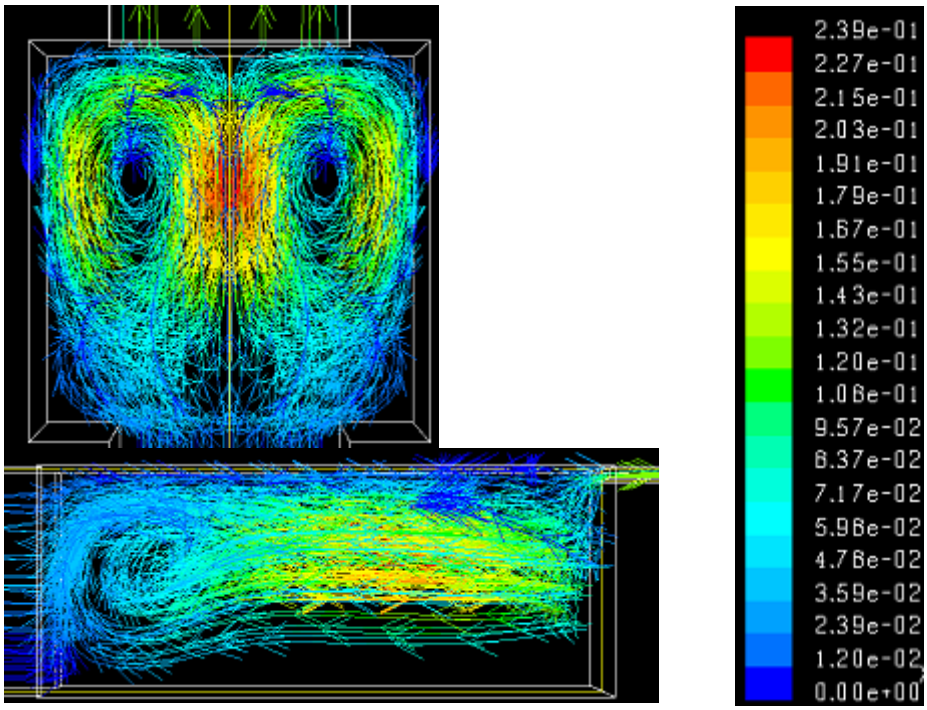

Figure 4.54: Path lines followed by particles in the micro reservoir injected from the inlet surface in case A15.

4.4.5 Variation in cross-section of the micro reservoir with first channel width = shallow channel width = 150 micron (A13, A14 and A15)

Figure 4.52, Figure 4.53 and Figure 4.54 show path lines corresponding to A13, A14 and A15, respectively. In case A13, the path lines diverge from the symmetrical axis and goes into the vertical vortices in the symmetrical halves of the micro reservoir. In addition, the particle motion is converged towards the bottom of the micro reservoir and move towards the shallow channel entrance. Few particles move back into the micro reservoir in vertical circular motion. Case A14 clearly shows two vortices from the top and particle motion is distributed more in the whole region of the micro reservoir. Straight particle motion directly from the first channel to the shallow channel can also be seen. Case A15 shows two horizontal vortices in the symmetrical halves and two weak vertical vortices near its entrance. The path lines are dense in the horizontal vortices showing the presence of many of the particles in these vortices.

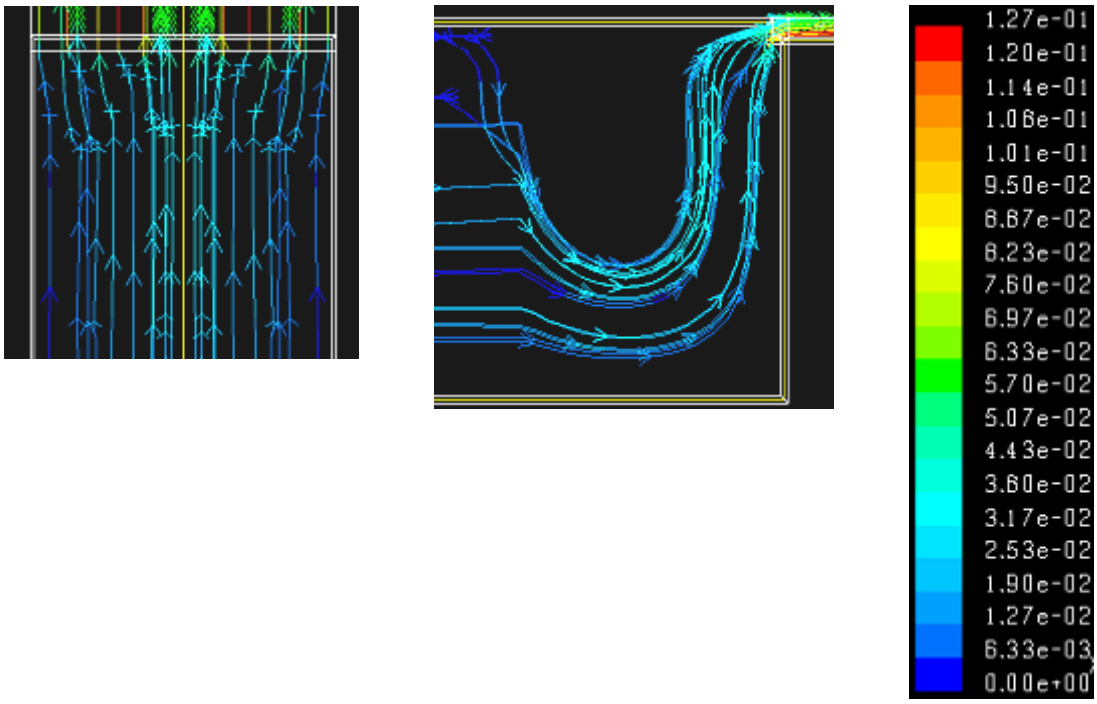

Figure 4.55: Path lines followed by particles in the micro reservoir injected from the inlet surface in case A16.

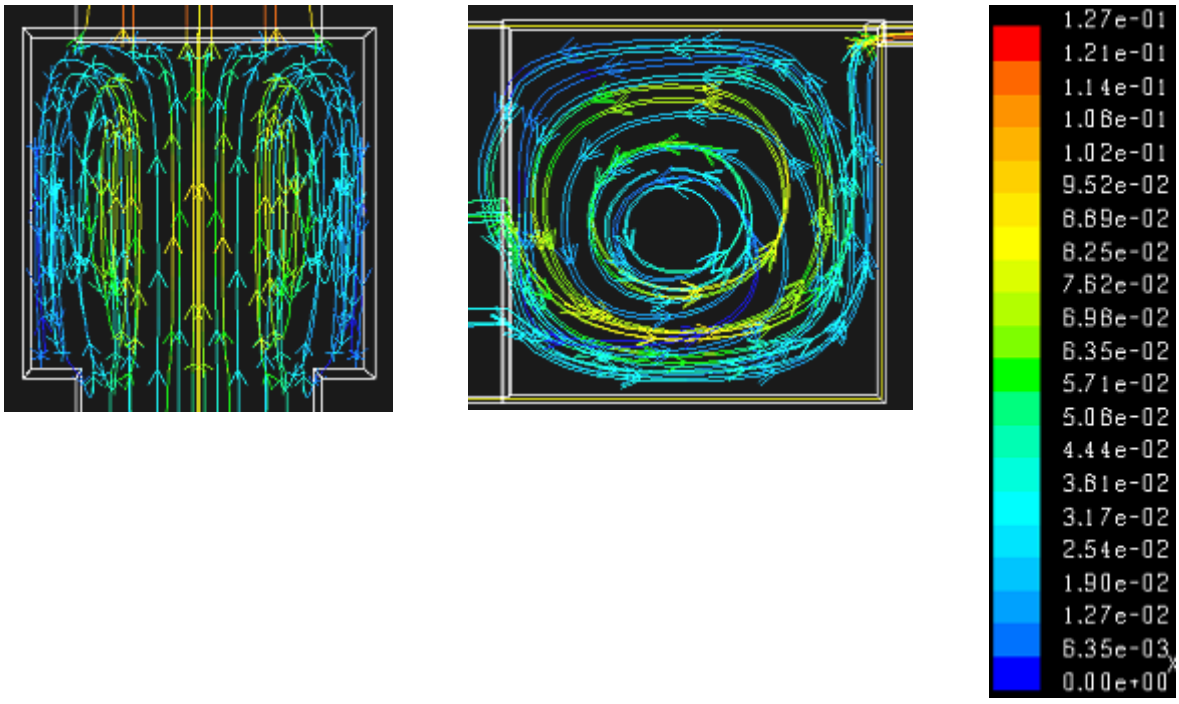

Figure 4.56: Path lines followed by particles in the micro reservoir injected from the inlet surface in case A17.

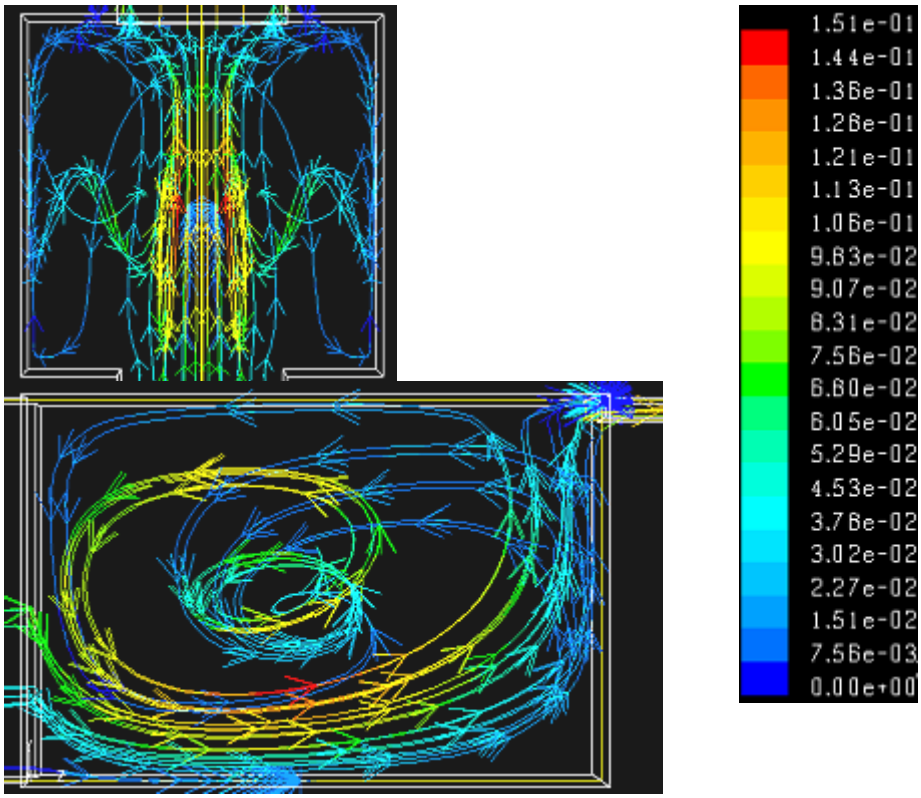

Figure 4.57: Path lines followed by particles in the micro reservoir injected from the inlet surface in case A18.

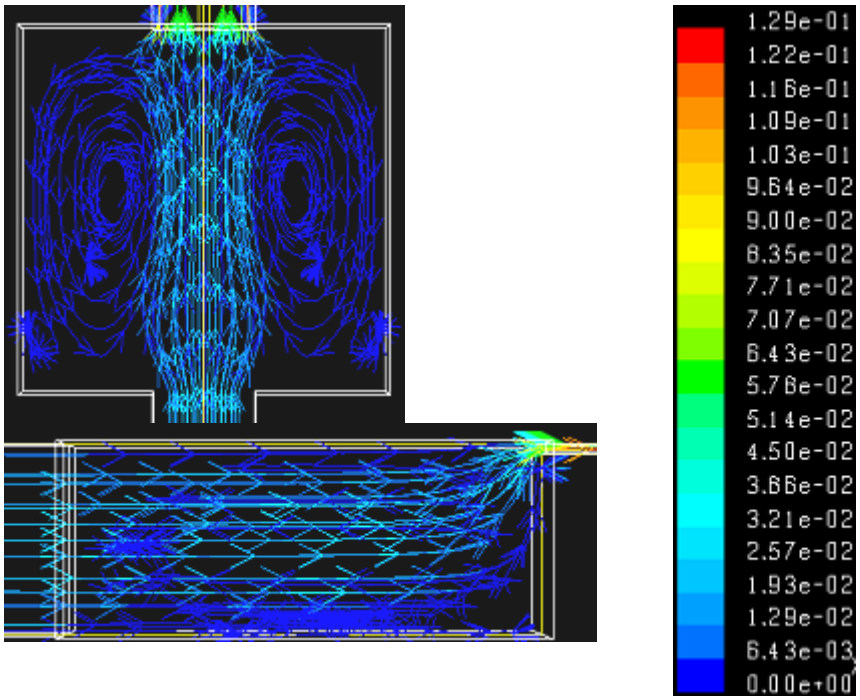

Figure 4.58: Path lines followed by particles in the micro reservoir injected from the inlet surface in case A19.

4.4.6 Variation in cross-section of the micro reservoir with first channel width = shallow channel width = 70 micron (A16, A17, A18 and A19)

Figure 4.55, Figure 4.56, Figure 4.57 and Figure 4.58 show path lines corresponding to A16, A17, A18 and A19, respectively. Case A16 shows the convergence of particles towards the bottom of the micro reservoir. The particle, then, follows the circular motion and rise towards the shallow channel entrance. There is no recirculation of particles. Case A17 give rise to vertical vortices in the symmetrical halves. The particles converge to the bottom of the micro reservoir and follows vertical circular motion in the micro reservoir. Fraction of them enters the shallow channel. Case A18 shows the convergence of particles in the bottom central region of the micro reservoir. Particles, in this case, also follows vertical circular motion in the micro reservoir but most of them enters directly in the shallow channel without recirculation. Case A19 shows quite straight path lines in the micro reservoir with very few particles trapped in the weak vortices in the micro reservoir. Most of the particles directly enter the shallow channel without recirculation.

4.5 Comparison of the mass fluxes

The mass fluxes in all the cases are compared as mentioned in the following sections to understand the flow resistance offered by different micro channel cases. Flow resistance in the micro channels is inversely proportional to the mass flux delivered by it.

4.5.1 Variation in the position of the micro reservoir from the inlet

The results (Figure 4.59) show the rise in mass flux as we change the position of the micro reservoir from the inlet. The rise becomes sharper with the shifting of micro reservoir. At 15900 micron, the mass flux increase to 3 times that of original position of 9900 micron. The rise in mass flux for phase 2 can also be seen but it is not much appreciable compared to phase1. Thus to get more of phase 2 to run through the micro channel, the most appropriate geometry will be the position of micro reservoir at the center of the micro channel.

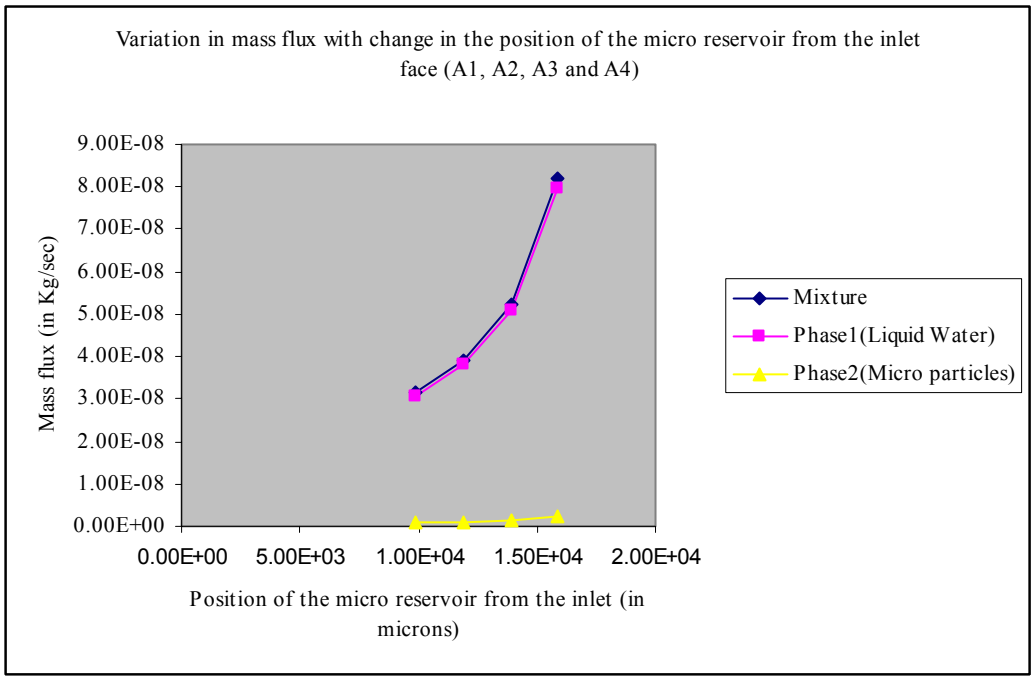

Figure 4.59: Variation in mass flux with the change in position of the micro reservoirs taking the cases A1, A2, A3 and A4 into account

4.5.2 Variation in shallow channel depths keeping the constant first channel depth and micro reservoir depth (A1 and A7, A5 and A8, A6 and A9)

When the shallow channel depth is increased, the mass fluxes in different channels are affected in different ways (Figure 4.60, Figure 4.61 and Figure 4.62). Micro channels with first channel and micro reservoir depth = 100 micron and 400 micron gives higher mass flux rise of mixture and phase 1 when the shallow channel depth is increased from 3 micron to 5 micron. However, the effect is not so sharp in the 250 micron depth counterpart. All the mentioned cases show a little rise in mass flux of phase 2.

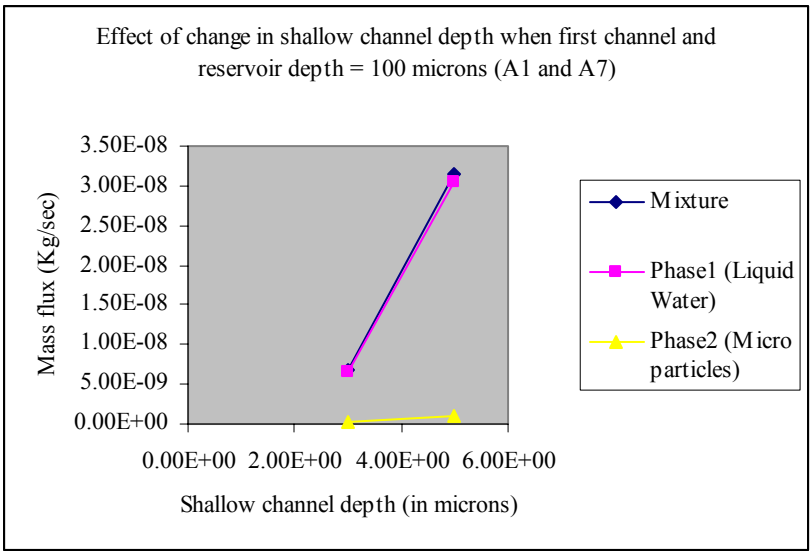

Figure 4.60: Effect of change of shallow channel depth on mass flux when the first channel depth and micro reservoir depth = 100 micron

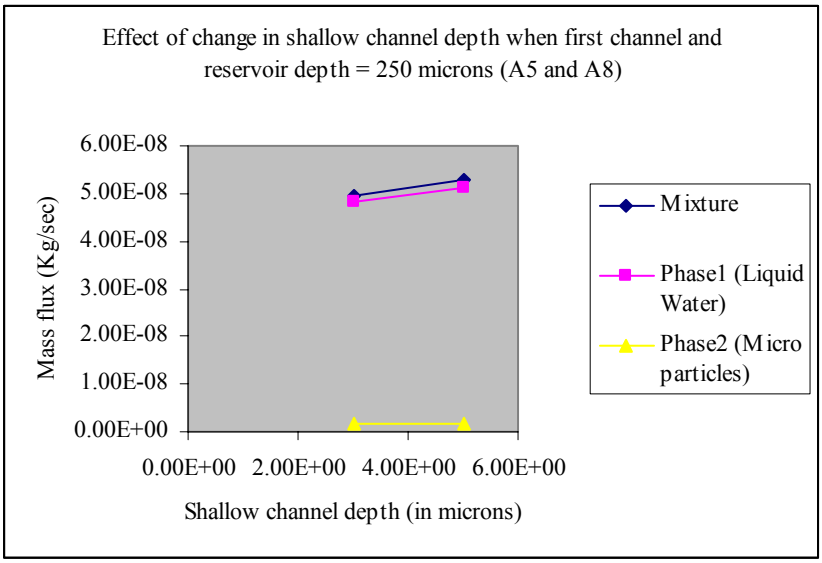

Figure 4.61: Effect of change of shallow channel depth on mass flux when the first channel depth and micro reservoir depth = 250 micron

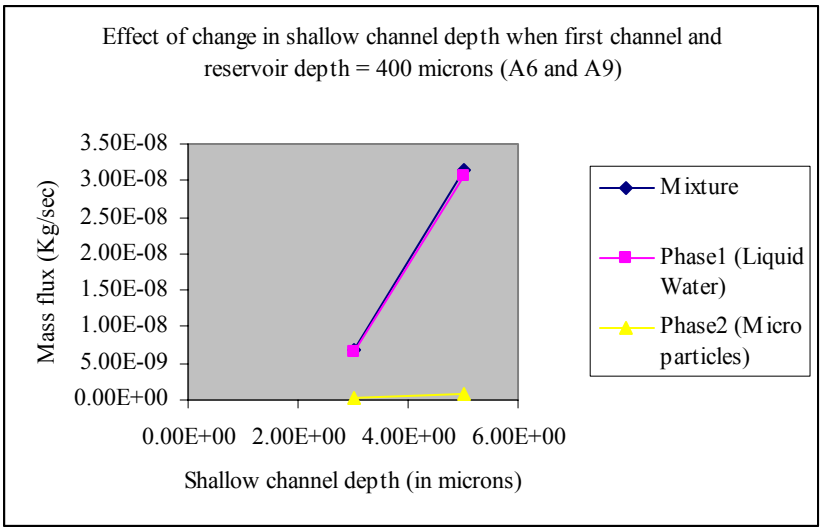

Figure 4.62: Effect of change of shallow channel depth on mass flux when the first channel depth and micro reservoir depth = 400 micron

4.5.3 Variation in cross-section of the micro reservoir with first channel width = shallow channel width = 100 micron

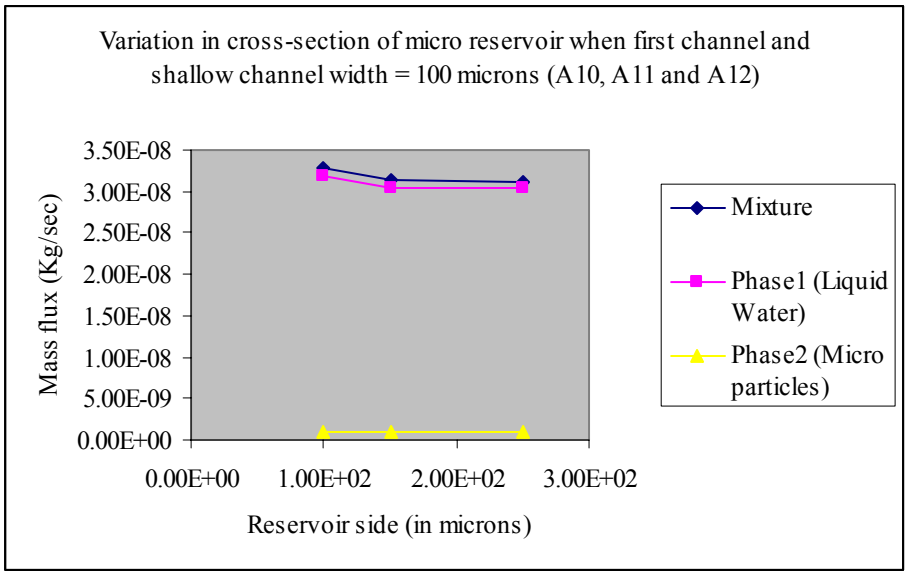

Figure 4.63: Effect of variation in cross-sectional area of the micro reservoir on the mass fluxes, when the first channel and shallow channel width = 100 micron

A fall in mass flux of mixture and phase1 can be seen when the micro reservoir cross section is increased from reservoir side = 100 micron to reservoir side = 150 micron (Figure 4.63). However it becomes more or less constant with the further increase in cross-section of micro reservoir with the side = 250 micron. Phase2 mass flux is constant in all the three cases.

4.5.4 Variation in cross-section of the micro reservoir with first channel width = shallow channel width = 150 micron

Figure 4.64 shows the rise in mass flux delivered when the micro reservoir cross-section is increased. The rise becomes sharper with the increase in reservoir side which is from 150 micron to 200 micron and from 200 micron to 250 micron. Phase2 mass flux remains constant in all the three cases.

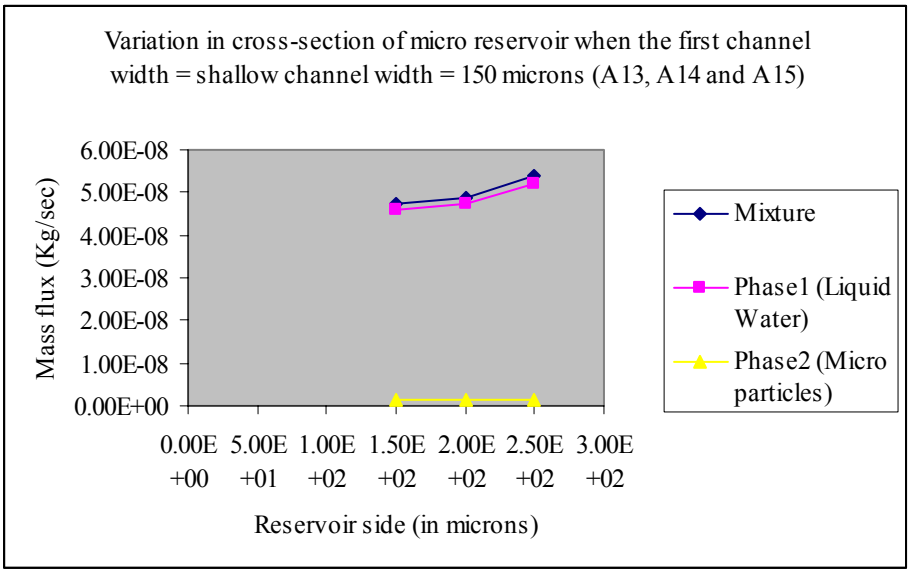

Figure 4.64: Effect of variation in cross-section of the micro reservoir on the mass flux when the first channel and shallow channel width = 150 micron

4.5.5 Variation in cross-section of the micro reservoir with first channel width = shallow channel width = 70 micron

The mass flux increases when the micro reservoir side is increased from 70 micron to 100 micron. It slightly decreases when the side is increased to 150 micron. There is sharp rise in mass flux when the reservoir side is increased to 250 micron. Phase 2 mass flux also shows increase with the increase in micro reservoir side.

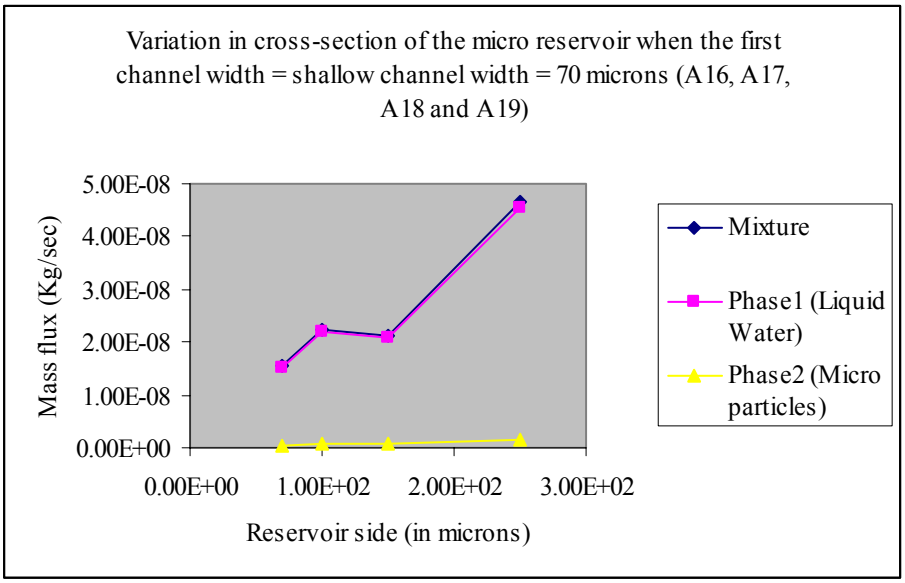

Figure 4.65: Effect of variation in cross-sectional area of the micro reservoir on the mass flux when the first channel and shallow channel width = 70 micron

Chapter 5: Design and Measurement: Single phase flow resistance experiments

5.1 Test Section

The test section consists of a silicon chip and micro channel holder. An exploded view of the entire cross-section drawn to scale is given in Figure 5.1. The silicon chip consists of a silicon wafer on which micro channels are etched and a pyrex glass plate which is anodically bonded to the silicon wafer. The sides of the silicon chip and Pyrex glass are 20 mm by 20 mm. The micro channel holder consists of a base plate and a cover plate. Two types of micro channels are used for experiments. They are enlisted as follows:-

1. Two-depth two-width micro channels: These micro channels consists of three parts namely: the first channel (width = 100 micron, depth = 250 micron and length = 9.9 mm), the micro reservoir (width = 200 micron, depth = 250 micron and length = 200 micron) and the shallow channel (width = 100 micron, depth = 5 micron and length = 9.9 mm). The cross-sectional geometry of the micro channel throughout its length is rectangular. The length of the micro channel is 20 mm which is equal to the length of the silicon substrate. Thus micro channel inlet and outlet coincide with the sides of the substrate. There are nineteen micro channels used on each substrate.
2. Straight micro channels: These micro channels are straight rectangular cross-sectional geometry micro channels. The dimensions of these micro channels are: width = 100 micron, depth = 250 micron and length = 20 mm. Similar to two-depth and two-width micro channel, the inlet and outlet of these micro channels

coincide with the side of the substrate. There are ninety micro channels used on each substrate.

There are 12 etched wafers (6 two-depth and two-width micro channels and 6 straight channels) used for the experiment. For each etched wafer 12 identical micro channel holders are used.

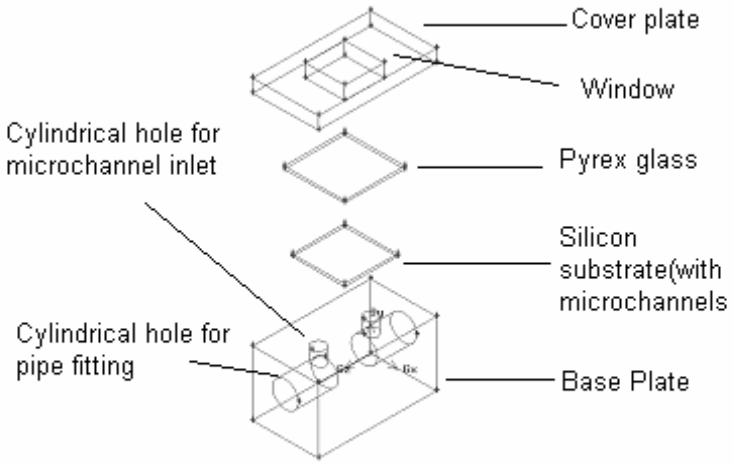

Figure 5.1: Exploded view of the micro channel holder

5.1.1 Micro channels

The photo mask layout for the micro channels was initially designed using cadence software. The micro channels were fabricated at the Institute of Microelectronics (IME), Singapore. The profile of each micro channel was checked using the profilometer. The micro channels were bonded anodically with pyrex glass: corning 7740. The thickness of pyrex glass is 0.5 mm. Before bonding, the glass and the silicon chips were cleaned using acetone and concentrated sulphuric acid. Finally, they were washed with ultra-pure water using the ultrasonic technique.

The chips and glasses were, then, dried using an air blower. The temperature in the anodic bonding was maintained at 400^{o}C and the potential difference between the electrodes was -1.7 kV. A glass was aligned with the silicon using the suction generated by vacuum pump which helps in holding the glass above the silicon chip. The glass was moved using threaded screws. After alignment, the glass was left on the silicon substrate for some time for the bonding to take place. In this way, all the 12 wafers were bonded with the pyrex glass.

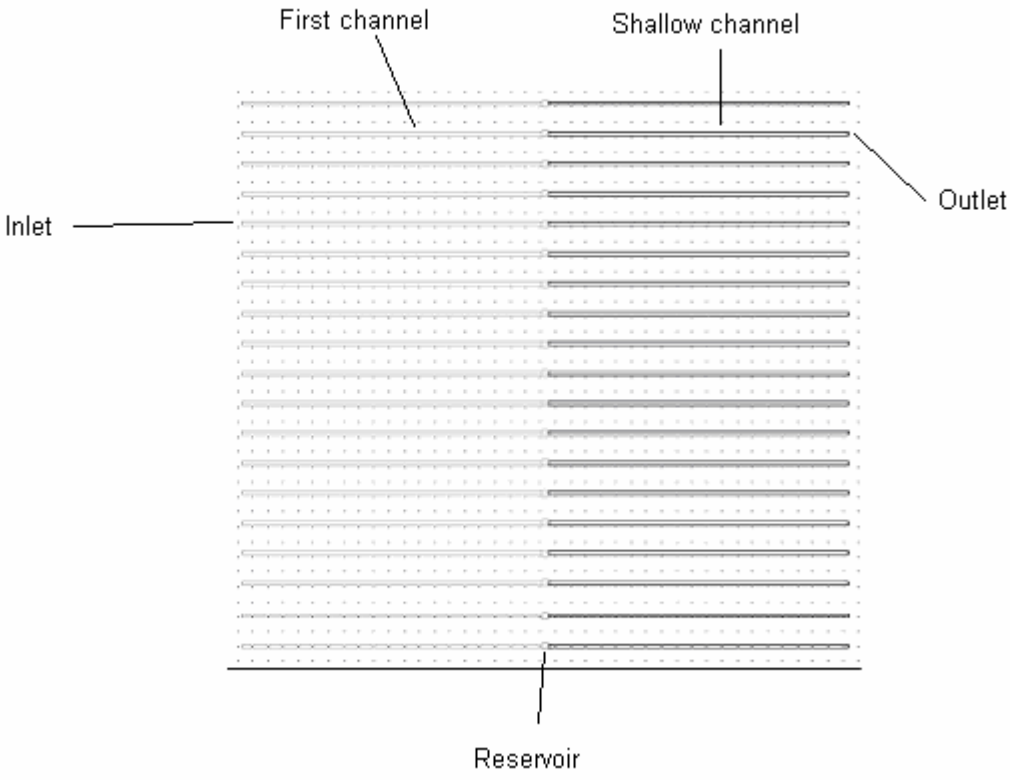

Figure 5.2: Photo mask layout of the two-depth and two-width micro channel used in the experiments

5.1.2 Supporting Hardware

The silicon substrate (containing the micro channels) with the pyrex glass plate was kept between the two holes on the aluminium base plate. The aluminium base plate dimensions are 30x25x25 cubic mm. The base plate has two internal channels in it. These channels has $1/4^{th}$ NPT brass fittings on one side and a smaller vertical channel (diameter = 5 mm) on the other. The vertical channel comes to the top of the base plate. The inner end holes separation between the vertical channels is 22 mm which is made in order to accommodate the substrate of length 20 mm.

This substrate was glued with the aluminium base plate with the help of epoxy glue. On the top of the glass plate was put another aluminium plate with a window of 15 mm by 15 mm. This window was put in order to facilitate clear view of the glass and the micro channels from the top for inspections. The bottom of the window sides was fixed to the glass plate in order to avoid any leakage through the junction during the experiment. The aluminium window plate and base plate has the same outer length and breadth. The gap between the outer edges of these plates is 1.5 mm. In order to cover this gap permanently, epoxy resin was fixed between this gap. All the micro channel holders were tested in a water bucket to check for any leakage in them.

5.2 Fluid Circuit and System Equipment

The experimental setup is shown in Figure 5.3. The fluid used for the experiment is de-ionized water. The experiments were conducted under normal atmospheric temperature and pressure.

5.2.1 Fluid Circuit and Piping

A pressure gauge is used to measure the pressure in the vessel or the micro reservoir for the fluid. This pressure gauge has the accuracy of 0.2% of FS, precision of 0.02 bar, readability 0.1 bar, and the maximum range 15 bar. The pressure applied to the cylinder is regulated with the help of a pressure regulator. A Digital Pressure Module (DPM) is used in the circuit just before the micro channel holder to get the best possible measurements of pressure drop across it. All the fluid circuit elements are connected with the ¼" NPT brass fittings and 6 mm diameter polyethylene piping. The piping has the maximum pressure limit of 15 bar.

The pressure vessel, which is made of aluminium, has the internal volume of 1200 cubic mm. The vessel is used to hold the fluid and pressurize it with the compressed air coming from the regulator end. The pressurized liquid, thus, rises from the bottom of the vessel. Valves, V1, V2 and V3, of on-off types are used to make or break the fluid circuit.

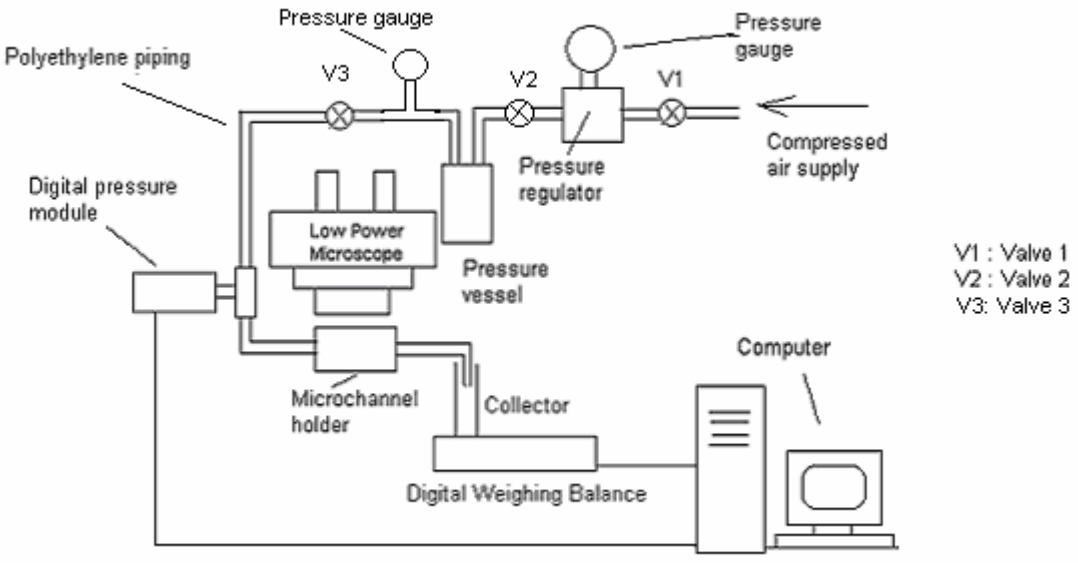

Figure 5.3: Schematic diagram of the experimental setup for the pressure-driven flow measurement in micro channel.

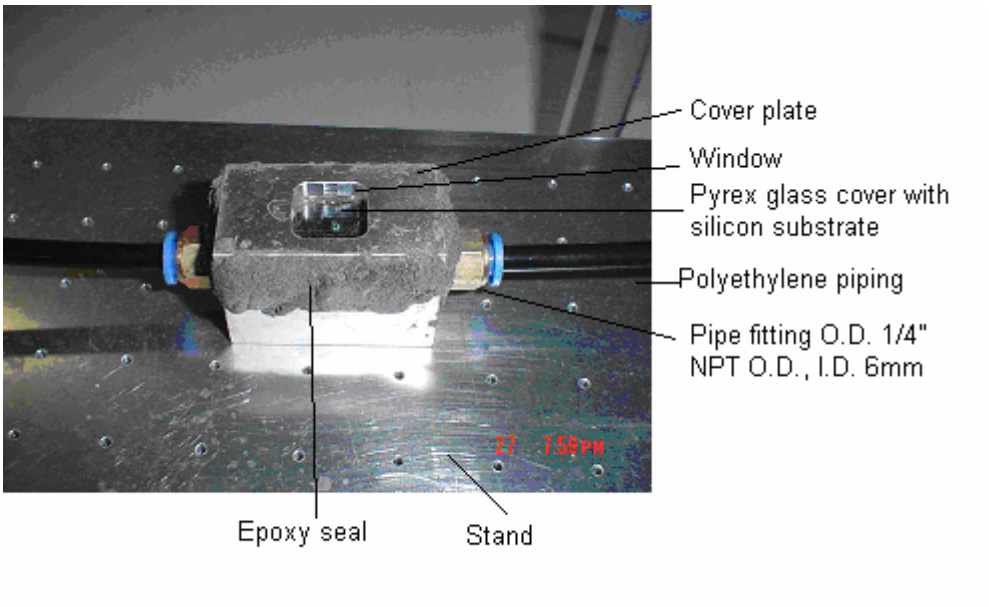

Figure 5.4: The microchip holder in the fluid circuit

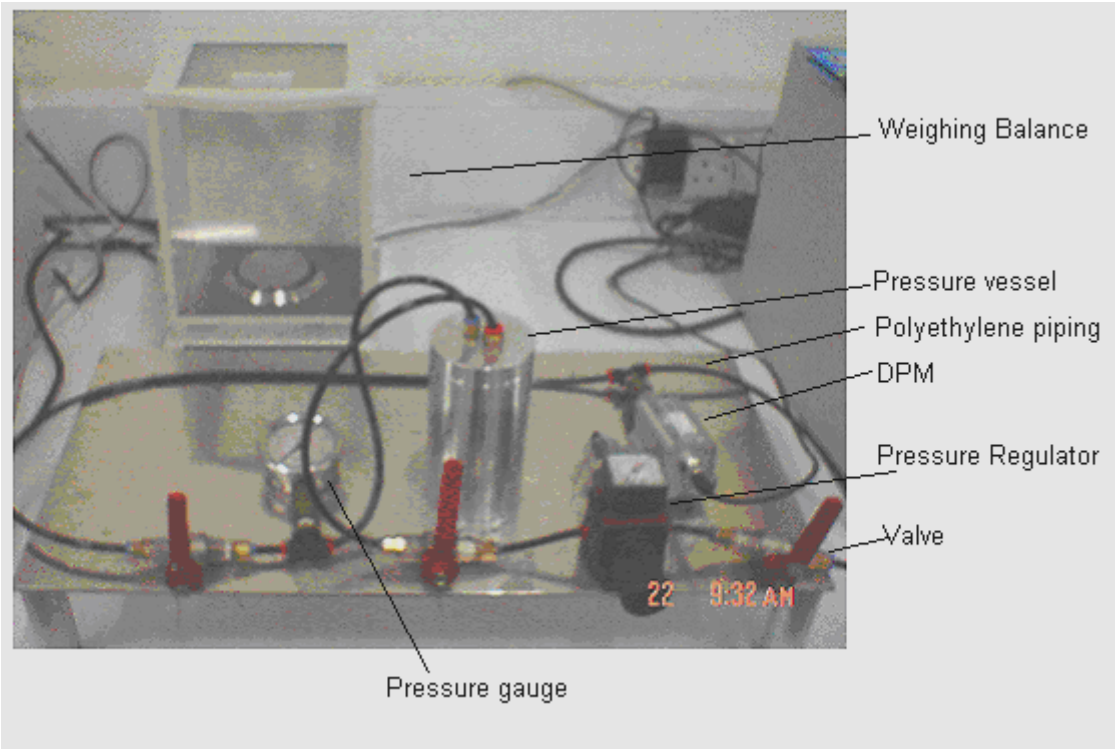

Figure 5.5: The fluid circuit of the experiment.

5.3: Instrumentation and Measurement

5.3.1 Volumetric Flow Rate

Volumetric flow-rate is measured using a digital weighing balance and a digital stop-watch. The digital weighing balance (Shimadzu AY 220) has a 0.1 mg of reading accuracy over the linear range of operation. The meter gives digital display output. The meter is powered by 240V AC power supply.

5.3.2 Pressure Drop

The pressure drop is measured using SI digital pressure module DPM-0010 which has the range from -1 to 10 bar. The pressure module is interfaced with the PC to get the reading with the accuracy of 0.025% of FS. The DPM is powered by 240V AC power supply.

5.3.3 Distance

All channel lengths and the channel widths of multiple channel designs are measured using the Olympus microscope with the magnification of 50. Longer dimensions such as the axial coordinates and the inlet/outlet pipe lengths are measured using a metric scale (± 0.5 mm). The depths of the various channels are measured using the profilometer.

5.4 Experimental Procedure

The experimental apparatus is shown in Figure 5.5. The pressure vessel is charged using the compressed air from a compressor pump. At full charge, the valve to the cylinder is closed and the pressure vessel becomes a closed system. The valve to the micro

channel holder is opened at the start of each experimental run and the liquid flows through the micro channels while the pressure continually decreases in the vessel.

A summary of the procedure followed for the single phase flow resistance measurements is as follows:

1. Mount the micro channel holder of the micro channel under investigation in the flow circuit. Calculate approximate pressure range required to obtain Re < 2000.

2. Start the electronic instruments such as digital weighing balance, DPM and PC.

3. Fill the pressure vessel with liquid.

4. Seal the vessel and open the valve to the compressed air coming from the compressor pump, allowing the vessel to be charged to desired pressure. Then close the valve, so the vessel is closed.

5. Open the valve to the micro channel holder, start the stop-watch, monitor the DPM reading and allow the liquid to flow to the measuring cylinder for certain time interval.

6. Close the valve, stop the stop-watch and weigh the measuring cylinder using the digital weighing balance.

Chapter 6: Results and Discussion: Single phase flow resistance experiments

The experiments were carried out under normal atmospheric temperature and pressure conditions. Since the mass on the balance and the pressure drop were sampled at the same time, the mass flow rate corresponding to the above pressure drop is

$$\rho Q = \frac{\Delta m}{\Delta t} \tag{7.1}$$

Thus, flow rate Q, for the given $\overline{\Delta P_{meas}}$ is

$$Q = \frac{\rho Q}{\rho}$$

$$= \frac{1}{\rho}\left(\frac{\Delta m}{\Delta t}\right) \tag{7.2}$$

6.1 Non-dimensionalization of measured variables

The measured pressure drop and flow rate are non-dimensionalized as follows, where ΔP^* and Q^* denote the non-dimensionalized variables. Note the dependence on physical parameters, shown in (7.3) and (7.4).

$$\Delta P^* = \text{function}(L,D,\mu,\rho) \tag{7.3}$$

$$Q^* = \text{function}(D,\mu,\rho) \tag{7.4}$$

thus, the variables are non-dimensionalized as

$$\Delta P^* = \frac{\Delta P_{meas}}{\frac{32\mu^2 L}{\rho D^3}} \tag{7.5}$$

$$Q^* = \left(\frac{4Q_{meas}}{\pi D^2}\right)\frac{\rho D}{\mu}$$

$$= \frac{\rho Q_{meas}}{\frac{\pi}{4} D\mu} \tag{7.6}$$

Equation (7.5) is chosen such that ΔP^* is equivalent to the Reynolds number based on the flow rate predicted by laminar theory for a given ΔP, i.e. $Q = \frac{\Delta P \pi D^4}{128 \mu L}$. Equation (7.6) is chosen such that Q^* is equal to the Reynolds number based on the measured flow rate. Alternatively,

$$\mathrm{Re}_{meas} = \frac{\rho\left(\frac{4Q_{meas}}{\pi D^2}\right).D}{\mu} \tag{7.7}$$

6.2 Results from the experiments with de-ionized water

For both the micro channels, the normalized pressure drop, ΔP^* is plotted against the normalized flow rate, Q^*. In classical laminar theory, the slope of the ΔP^* versus Q^* curve is equal to one for Re < 2000 or equivalently for Q^* < 2000. If the slope is less than one, the flow resistance has increased above that predicted by the classical macro-scale theory.

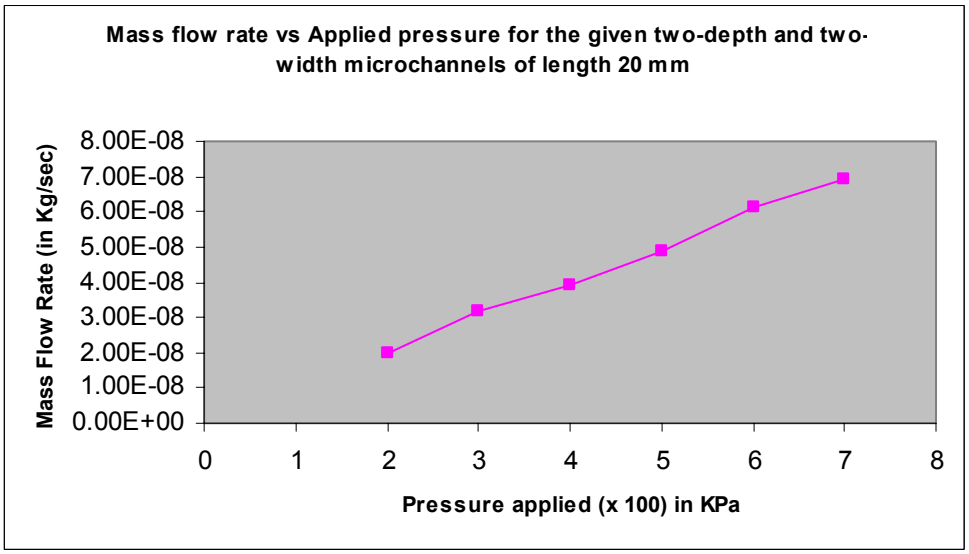

Figure 6.1: Mass flow rate vs. Pressure for two-depth and two-width micro channels

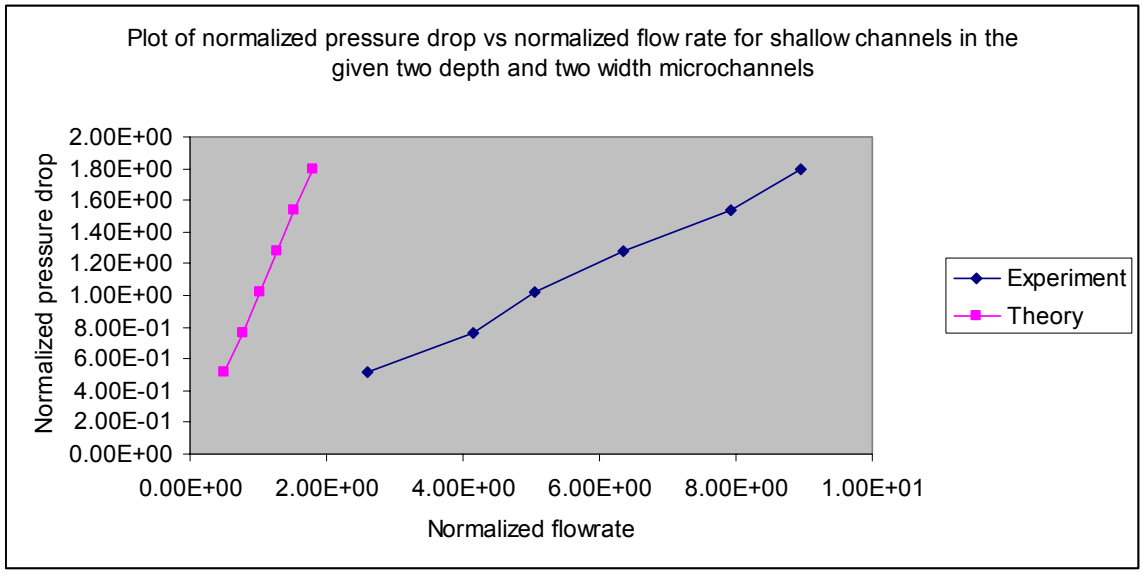

Figure 6.2: Normalized pressure drop vs. Normalized flow rate for two-depth and two-width micro channel. Note that the theoretical line corresponds to shallow channel since the flow resistance is dominated by this part of the micro channel

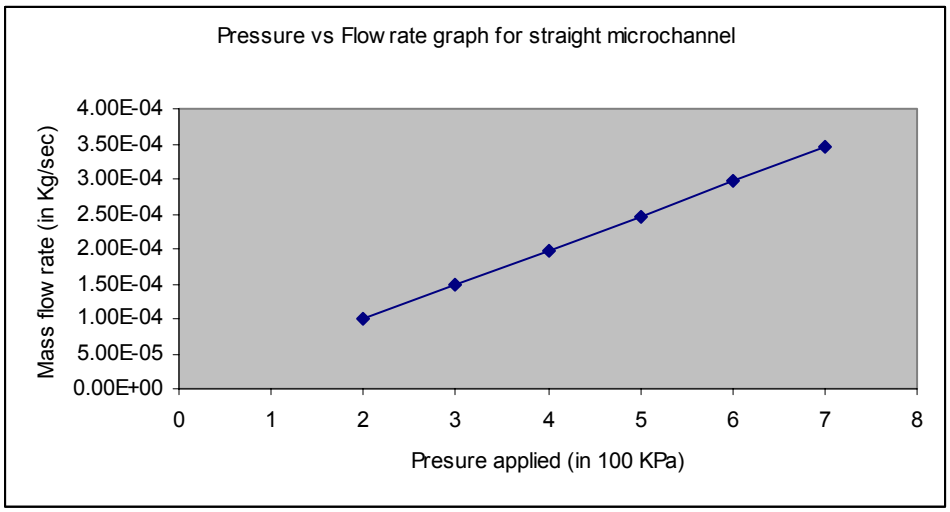

Figure 6.3: Mass flow rate vs. Pressure applied for straight micro channel

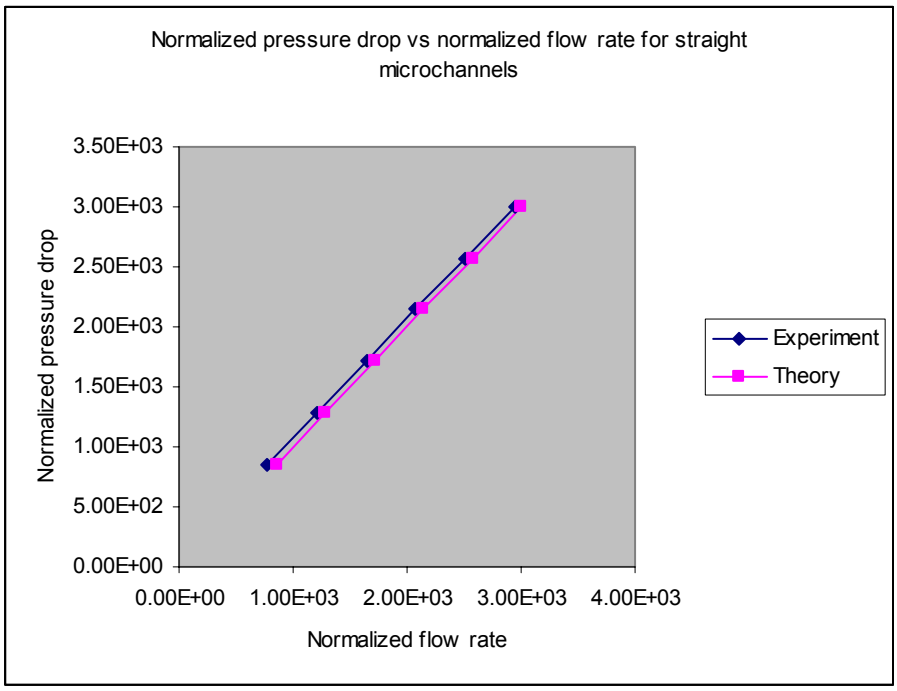

Figure 6.4: Normalized pressure drop vs. Normalized flow rate for straight micro channels

The results show that for two depth and two-width micro channels, the flow rate is proportional to the pressure drop. However, the slope of normalized pressure drop vs normalized flow rate graphs is less than 1 which indicates that the flow resistance in this micro channel is higher than expected and that the Reynolds number rise is less sharp than expected. The straight micro channels show good agreement with macro scale theory and the flow resistance is at par with the expected.

Chapter 7: Conclusions

The micro channel with two depths and two widths has a wide range of applications in the micro fluidics field especially in the μ-TAS and LOC applications. Results from the contours of volume fraction of phase 2 in the micro reservoir show that some geometries favor "better detection" in the micro reservoir while the others support "no clogging" in the shallow channel. In some cases there is more accumulation of particles which also helps in better detection as the particles are confined to small area. Path lines corresponding to each case shows the presence of horizontal vortices in the symmetrical halves, vertical vortices, straight motion of the particles and recirculation. Centerline velocity magnitude plots give us an idea about the rate of mixing in the micro reservoir of the fluid. Pressure profiles are identical in all the cases and show that the pressure in the micro channel decreases from the point of location of the micro reservoir.

Experimental studies confirmed that the two-depth and two-width micro channel offers higher resistance than expected while the straight channel gives good agreement with the theory.

7.1 Simulations

7.1.1 Pressure Profile:

The pressure remains more or less constant in the first channel at 200 kPa and gradually decreases to zero (gauge pressure) at the outlet. Pressure profile of case A2 is shown in Figure 4.1. All the micro channels follow the same pressure profile. Shifting the position of the reservoir shifts the point from which the pressure starts decreasing in the channel. Variation in the depth of the channels and variation in the cross section area of the reservoir does not affect the pressure profile.

7.1.2 Centerline velocity magnitude

For the cases A1, A2, A3 and A4, the nearer the micro reservoir is to the outlet, the higher the centerline velocity magnitude in the channel parts. The centerline velocity magnitude in the micro reservoir is the same in all the four cases. The plots also suggest that in the first channel, the velocity magnitude remains more or less constant in the A1 case, little fluctuates in the A5 case but rise gradually from the middle of the first channel to the reservoir in the A6 case. For the cases A7, A8 and A9, the centerline velocity magnitude remains more or less constant along the first channel but rises gradually before the entrance of the micro reservoir in the 100 micron depth channel and 400 micron depth channel. However, in the first channel the centerline velocity magnitude is much lower in A10 and high in A11 and A12. In the micro reservoir, the centerline velocity magnitude is same in A10 and A12 but high in A11.

In the case of A15, the centerline velocity magnitude decreases in the first channel as the fluid start reaching the reservoir. The reverse is followed in A13 and A14. In case A17, A18 and A19, a gradual rise in centerline velocity magnitude of the fluid as it reaches the micro reservoir entrance.

7.1.3 Particle Accumulation

Case A4 is less likely to get clogged in the shallow channel part compared to A1, A2, A3 and A4. Also, cases A1 and A3 are more suitable for detection purpose from the top. Case A5 is best in both respects of no clogging in the shallow channel and better detection in the micro reservoir compared to A1 and A6. A6 is not suitable for detection while A1 is likely to get clogged in the shallow channel part. Case A7 is

most suitable for better detection from the top and for not supporting clogging at the shallow channel entrance. The accumulation is also confined to a smaller region. Case 10 is best for high detection and low susceptibility for clogging compared to A11 and A12. A rise in volume fraction can also be seen at the central region of the top wall in A14 and at the bottom wall of reservoir in case A15. Case A19 also shows depletion at the backside of the top wall of the micro reservoir.

7.1.4 Path lines followed by particles injected from the inlet surface:

For the cases A1, A2, A3 and A4, the particle motion is confined to the periphery of the two vortices rather than at the center. Case A4, the vortices are not so clear. In case A6, the particles converge to the top wall of the micro reservoir and move towards the shallow channel entrance in straight forward way. However, the particles show settling toward the bottom wall of the micro reservoir in circular motion. Particles in case A7 converge towards the bottom of the micro reservoir at its entrance and move toward the top wall in the helical path. However, in case A8, there is no vortex and the path lines are quite straight. Case A12 also shows the same scenario but the particle motion is more in the vertical recirculation and the path lines are distributed uniformly in the entire micro reservoir region. Case A15 shows two horizontal vortices in the symmetrical halves and two weak vertical vortices near its entrance. The path lines are dense in the horizontal vortices showing the presence of many of the particles in these vortices.

Case A19 shows quite straight path lines in the micro reservoir with very few particles trapped in the weak vortices in the micro reservoir. Most of the particles directly enter the shallow channel without recirculation.

7.1.5 Mass Flux:

The mass flux rises as we change the micro reservoir position from the middle of the micro channel towards its outlet. The rise becomes sharper with the shifting of micro reservoir. At 15900 micron, the mass flux increases to 3 times that of original position of 9900 micron. The rise in mass flux for phase 2 can also be seen but it is not much appreciable compared to phase1. Thus to get more of phase 2 to run through the micro channel, the most appropriate geometry will be the position of micro reservoir at the center of the micro channel.

When the shallow channel depth is increased, the mass fluxes in different channels are affected in different ways (Figure 4.60, Figure 4.61 and Figure 4.62). Micro channels with first channel and micro reservoir depth = 100 micron and 400 micron gives higher mass flux rise of mixture and phase 1 when the shallow channel depth is increased from 3 micron to 5 micron. However, the effect is not so sharp in the 250 micron depth counterpart. All the mentioned cases show a little rise in mass flux of phase 2.

A fall in mass flux of mixture and phase1 can be seen when the micro reservoir cross section is increased from reservoir side = 100 micron to reservoir side = 150 micron (Figure 4.63). However it becomes more or less constant with the further increase in cross-section of micro reservoir with the side = 250 micron. Phase2 mass flux is constant in all the three cases.

Figure 4.64 shows the rise in mass flux delivered when the micro reservoir cross-section is increased. The rise becomes sharper with the increase in reservoir side which is from 150 micron to 200 micron and from 200 micron to 250 micron. Phase2 mass flux remains constant in all the three cases.

The mass flux increases when the micro reservoir side is increased from 70 micron to 100 micron. It slightly decreases when the side is increased to 150 micron. There is sharp rise in mass flux when the reservoir side is increased to 250 micron. Phase 2 mass flux also shows increase with the increase in micro reservoir side.

7.2 Experiments

The results show that for two-depth and two-width micro channels, the flow rate is proportional to the pressure drop. However, the slope of normalized pressure drop vs normalized flow rate graphs is less than 1 which indicates that the flow resistance in this micro channel is higher than expected and that the Reynolds number rise is less sharp than expected. The straight micro channels show good agreement with macro scale theory and the flow resistance is at par with the expected.

Possible future work on this project can extend to the fabrication of all these kinds of micro channels, visualization of the change in particle volume fraction in the micro reservoir and measuring the flow resistance in these micro channels experimentally.

List of References:

1. Sato, K., Tokeshi, M., Odake, M., Kimura, H., Ooi, T., Nakao, M., and Kitamori, T. (2000). Integration of an Immunosorbant Assay System : Analysis of Secretory Human Immunoglobulin A on Polystyrene Beads in a Microchip. Analytical Chemistry, 72, 1144-1147.
2. Fu, A. Y., Spence, C., Scherer, A., Arnold, F. H., and Quake, S. R. (1999). A microfabricated fluorescence – activated cell sorter. Nature Biotechnology, 17, 1109-1111.
3. Wilding, P., Kricka, L. J., Cheng, J., Vichia, G. H, Shoffner, M. A, and Fortina, P. (1998). Integrated Cell Isolation and Polymerase Chain Reaction Analysis Using Silicon Microfilter Chambers. Analytical Biochemistry, 257, 95-100.
4. Chang, W., Trebotich, D., Lee, L. P., Liepmann, D. (2000). Blood Flow in Simple Microchannels. Microtechnologies in Medicine & Biology, 1st Annual International IEEE-EMBS Special Topic Conference on, 311-315
5. Anderson, H., Wijngaart, W. V., Enoksson, P., and Stemme, G. (2000). Micromachined flow-through filter-chamber for chemical reactions on beads. Sensors and Actuators B, 67, 203-208.
6. Liu R. H., Stremler, M. A., Sharp, K. V., Olsen, M. G., Santiago, J. G., Adrian, R. J., Aref, H., and Beebe, D. J. (2000). Passive Mixing in a three dimensional serpentine micro channels. Journal of MEMS, 9, 190-197.
7. Bayt, R. L., Ayon, A. A., and Breuer, K. S. (1997) A performance evaluation of MEMS-based micronozzles. AIAA Proc. 33rd AIAA/ASME/SAE/ASEE Joint Propulsion Conf. Exhibit., 97-3169.

8. Molho, J. I., Herr, A. E., Mosier, B. P., Santiago, J. G., Kenny, T. W., Brennen, R. A., Gordon, G. B., and Mohammadi, B. (2001). Optimization of Turn Geometries for Microchip Electrophoresis. Analytical Chemistry, 73(6), 1350-1360.
9. Koning, J. M. (1997). Simulations of Micro channels with Sinusoidally Rough Walls. MS Thesis, San Jose State University.
10. Shrewsbury, P. J., Muller, S. J., and Liepmann, D. (2001). Effect of Flow on Complex Biological Macromolecules in Microfluidic Devices. Biomedical Microdevices, 3(3), 225-238.
11. Knight, J. B., Vishwanath, A., Brody, J. P., and Austin, R. H. (1998) Hydrodynamic Focussing on a Silicon Chip : Mixing Nanoliters in Microsecond. Phys. Rev. Lett. 80, 17, 3863.
12. Zahn, J. D., Talbot, N. H., Liepmann, D., and Pisano, A. P. (2000). Microfabricated Microneedles for Minimally Invasive Biomedical Devices. Biomedical Microdevices, 2(4), 295-303.
13. Branebjerg, J., Gravesen, P., Krog, J. P., and Nielsen, C. R. (1996). Fast mixing by lamination. Proc. IEEE MEMS Workshop, San Diego, CA, 441-446.
14. Choi, S. (1991). Friction Factors And Heat Transfer In Microtubes. Ph.D thesis, Dept. of Mechanical Engineering, Louisiana Tech. University.
15. Flockhart, S. M., and Dhariwal, R. S. (1998). Experimental and numerical investigation into the flow characteristics of channels etched in (100) silicon. J. Fluid. Eng., 120, 291-295.
16. Jiang, X. N., Zhou, Z. Y., Yao, J., Li, Y., and Ye, X. Y. (1995). Micro-fluid flow in micro channel. Transducers'95, Stockholm, Sweden, June 25-29, 317-320.

17. Mala, G. M., and Li, D. (1999). Flow characteristics of water in microtubes. Int. J. Heat and Fluid Flow, 20, 142.

18. Papautsky, I., Brazzle, J., Ameel, T., and Frazier, A. B. (1999a). Laminar fluid behavior in microchannels using micropolar fluid theory. Sensors and Actuators A, 73(2), 101-108.

19. Papautsky, I., Gale, B. K., Mohanty, S., Ameel, T. A., and Frazier, A. B. (1999b) Effects of rectangular microchannel aspect ratio on laminar friction constant. Proc. SPIE Symposium on Micromachining and Microfabrication: MicroFluidic Devices and Systems, Santa Clara, CA, Sep. 20-21, 147-158.

20. Peng, X. F., Peterson, G. P., Wang, B. X. (1994). Frictional Flow Characteristics of Water Flowing Through Rectangular Microchannels. Exp. Heat Trsfr., 7, 249-264.

21. Pfahler, J., Harley, J., Bau, H., and Zernel, J. (1991). Gas and liquid flow in small channels. Proc. ASME Micromech. Sensors, Actuators, and Systems, DSC, 32, 49-60.

22. Qu, W., Mala, M., and Li, D. (2000). Pressure-Driven Water Flows in Trapezoidal Silicon Microchannels. International Journal of Heat and Mass transfer, 43, 353-364.

23. Sharp, K. V., Adrian, R. J., Santiago, J. G., and Molho, J. I. (2000). Liquid Flows in Micro channels. CRC Handbook of MEMS, M. Gad-el-Hak (ed., 2001), CRC Press, New York, 6-1 to 6-38.

24. Tuckerman, D.B., and Pease, R.F.W. (1981). High-Performance Heat Sinking for VLSI. IEEE Electron Device Letters, EDL2(5), 126-129.

25. Wilding, P., Pfahler, J., Bau, H. H., Zemel, J. N. and Kricka, L. J. (1994). Manipulation and flow of biological fluids in straight channels micromachined in silicon. Clinical Chemistry, 40, 43-47.

26. Wu, P., and Little, W. A. (1983). Measurement of friction factors for the flow of gases in very fine channels used for microminiature joule-thomson refrigerators. Cryogenics, 5, 273-277.

27. Yu, D., Warrington, R. O., Barron, R., and Ameel, T. (1995). An experimental and theoretical investigation of fluid flow and heat transfer in microtubes. ASME/JSME Thermal Engineering Conf., March, Maui, Hawaii, 1, 523-553

28. Sharp, K. V. (2001). Experimental Investigation of Liquid and Particle-Laden Flows in Microtubes. PhD Thesis, University of Illinois.

29. Berg., A. V., and Lammerink, T. (1998). Micro total analysis systems: microfluidic aspects, integration concepts and applications. Top. Curr. Chem., 194, 21-49.

30. Jaeggi, D., Gray, R., Mourlas, N., and Drienbuizen, R. (1998). Novel interconnection technologies for integrated microfluidic systems : Solid State Sensor and Actuator Workshop, Hilton Head Island, South Carolina, June 8-11, 112-115.

31. Cristel, L., Peterson, K., McMillian, W., and Northrup, M. (1997). Rapid automated nucleic acid probe assays using silicon micro structures for nucleic acid concentration. J. Biomech. Eng., 121, 22-27.

32. Carlson, R., Gabel, C., Chan, S., and Austin, R. (1997). Self sorting of white blood cells in a lattice. Phys. Rev. Lett., 79, 2149-2152.

33. Bing H., Tan, L., and Regnier, F. (1999). Microfabricated Filters for Microfluidic Analytical Systems. Analytical Chemistry, 71, 1464-1468.

34. McLachlan, R. (1991). A steady separated viscous corner flow. J. of Fluid Mechanics, 231, 1-34.

35. Harns, T. M. (1997). Heat Transfer and Fluid Flow in Deep Rectangular Liquid Cooled Micro channels Etched in a (110) Silicon Substrate. MS Thesis, University of Cincinnati.

36. Tuckerman, D. B. (1984). Heat-Transfer Microstructures for Integrated Circuits. Ph.D. Thesis, Stanford University.

37. Munson, B. R., Young, D. F., and Okiishi, T. H. (2002). Fundamental of Fluid Mechanics. Fourth Edition, Wiley, New York.

38. GAMBIT Modeling Guide. (2001). Vol (1-3), FLUENT Inc.

39. Rhie, C. M., and Chow, W. L. (1983). Numerical Study of the Turbulent Flow Past an Airfoil with Trailing Edge Separation. AIAA Journal, 21(11), 1525-1532.

40. Patankar, S. V. (1980). Numerical Heat Transfer and Fluid Flow. Hemisphere Pub. Corp. Washington, D.C.

41. Vasquez, S. A., and Ivanov, V. A. (2000). A Phase Coupled Method for Solving Multiphase Problems on Unstructured Meshes. Proceedings of ASME FEDSM'00: ASME, Fluids Engineering Division Summer Meeting, Boston.

42. FLUENT 6.0 User's Guide. (2001). Volume (1-5), FLUENT Inc.

43. Krüger, J., Singh, K., O' Neill, A., Jackson, C., Morrison, A., and O' Brien, P. (2002). Development of a microfluidic devices for fluorescence activated cell sorting. Journal of Micromechanical microengineering, 12, 486-494.

44. Nakajima, M. (2001). Novel micro channel system for monodispersed microspheres. RIKEN Review: Science and Technology in Micro/Nano Scale, 36, 21-23

45. Wenski, T. E. (1997). Particle Simulation of Micro channel flows with Realistic Boundaries. MS Thesis, San Jose State University.

46. Pfahler, J. N. (1992). Liquid Transport in Micron and Submicron Size Channels. PhD Thesis, University of Pennsylvannia.

47. Eringen, A. C. (1964). Simple Microfluids. International Journal of Engineering Science, 2(2), 205-217.

48. White F. M. (1994). Fluid Mechanics. Third Edition, McGraw Hill, New York.

49. Pan, F., and Acrivos, A. (1967). Steady flows in rectangular cavities. J. of Fluid Mechanics, 28, 643-655.

50. Burggraf, O. R. (1966). Analytical and numerical studies of the structure of steady separated flow. J. of Fluid Mechanics, 24, 113-151.

51. Heinbuch, V., and Fischer, J. (1989). Liquid Flow in Pores : slip, no-slip or multilayer sticking. Physical Review A, 40(2), 1144-1146.

52. Beavers, G. S., Sparrow, E. M., and Magnuson, R. A. (1970). Experiments on Hydrodynamically Developing Flow in Rectangular Ducts of Arbitrary Aspect Ratio. Int. J. of Heat & Mass Transfer, 13, 689-702.